Numerical Analyses of Dip-Slip Fault Rupture-Suction Bucket Interaction

Master Thesis

Vasileios Papavasileiou
Department of the Built Environment
Aalborg University

AALBORG UNIVERSITY
DENMARK

Department of the Built Environment
M.Sc. Structural and Civil Engineering
Thomas Manns Vej 23
9220 Aalborg Ø
www.aau.dk

Title:

Numerical Analyses of Dip-Slip Fault Rupture-Suction Bucket Interaction

Project:

Master Thesis

Project period:

February - June 2021

Supervisors:

Lars Bo Ibsen
Amin Barari

Number of pages: 91
Number of appendices: 2
Submission date: June 10, 2021

Abstract:

This thesis concerns a Numerical Analyses of Dip-Slip Fault Rupture-Suction Bucket Interaction. A tripod suction bucket foundation is modelled in Plaxis 3D with Hardening Soil Model with Small Strain Stiffness constitutive model, and the free field results for both normal and reverse fault rupture are compared with published data from previous studies, in order to verify the numerical model.

A parametric study is performed with the presence of a tripod suction bucket foundation interacting with a reverse fault rupture. All three bucket legs are positioned subsequently in a way that the free field fault would emerge below them. The L/D ratio is equal to 1, accounting for 6.25 meters length and diameter. The soil response in terms of plastic shear strain propagation and settlements is examined. In addition, structural displacements, rotations and forces are investigated for each of the three tripod positions. The same analysis is conducted with $L/D = 0.5$, accounting for 3.25 meters skirt length and 6.5 meters diameter.

This research revealed that the presence of the structure is having an impact on the fault rupture propagation and that the tripod has to withstand horizontal dislocations, rotations and large loads due to the fault. The worst case scenario appeared to be the propagation of the fault rupture and it's interaction with the middle bucket of the tripod, where the largest loads and rotations are experienced. The downsizing of skirt's length is proved to be beneficial since it is not forcing the structure to tilt or displace more, while at the same time is reducing the loads imposed to the half.

Further studies are proposed to further enlighten the mechanism involving in the complex phenomenon of Dip-Slip Fault Rupture-Suction Bucket Interaction.

Preface

This thesis reflects the research effort related to the master thesis written during the 4^{th} semester of Structural and Civil Engineering Master of Science at Aalborg University.
The author would like to express his gratitude to the supervisors Amin Barari and Lars Bo Ibsen for their constant support and guidance. Also, the author would like to thank Professors Ioannis Anastasopoulos, George Gazetas, Michael Davies and Fraser Bransby for the data they kindly provided and led to the validation of the proposed model.

This thesis could not be completed without the constant support from my family and friends. The highest stake of every achievement belongs to them and I would not be who I am today without their love and constant support.

Reading guide

References are made using the Harvard method.A list of the sources and external references mentioned in the report can be found under the section "Bibliography". If information on specific citations in the bibliography section are missing is an indication that the author was not able to acquire them even after extensive research and hence, are omitted. In text citations are placed in parenthesis, with the year in brackets, e.g. "...(Papavasileiou [2021]). Figure and table numbering follow the current chapter number. Formulas are given as chapter number and formula number. For appendix, the above is assigned a letter instead of chapter number, e.g. "Figure A.1", "Table C.2" and "(E.2)".
For mathematical expressions, references are given in the form: "... is determined by Equation 1.1". Calculation and example expressions do not have an equation number unless special reference is deemed necessary.

Contents

Introduction 1

1.1 Renewable Energy Sector

Energy production from renewable sources has been in the recent years one of the primary economical, political and social objectives globally. In 2004, the share of energy from renewable sources in gross final consumption in the European Union was 8.5%, while in 2018 this percentage was increased to 18%. Figure 1.1 illustrates the share of energy consumption from renewable resources in selected European countries in 2017.

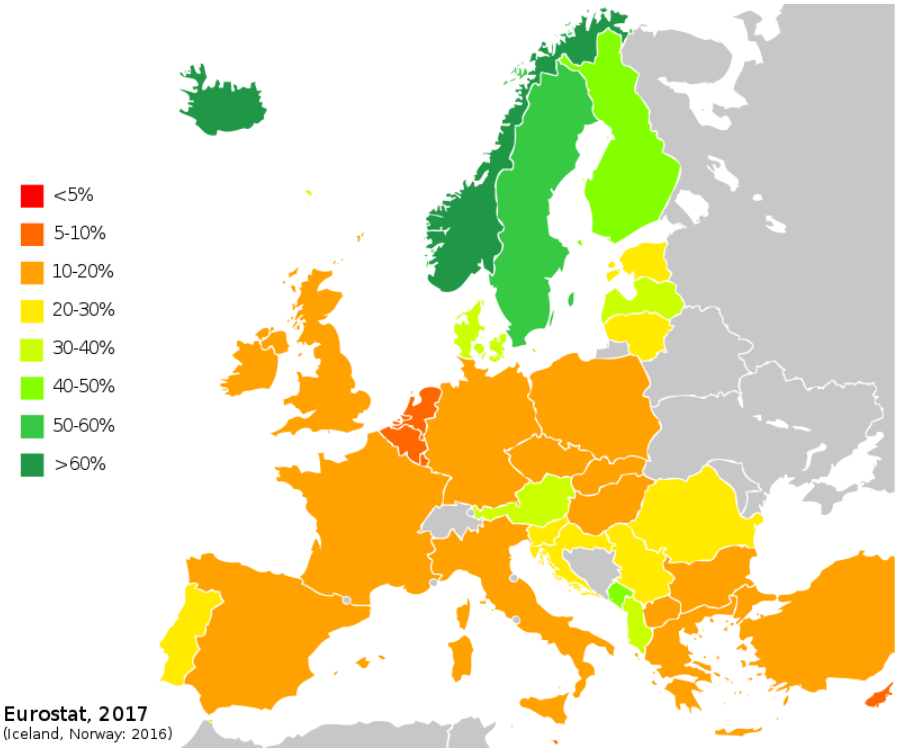

Figure 1.1. Share of renewable energy in gross final energy consumption. Data for year 2017 in selected European countries.

The Europe 2020 strategy incorporates a target of at least 20% of gross final energy consumption from renewable sources by 2020, with a further 12% increase, adding up to a total of 32% until 2030. According to (IRENA [2020]), renewable capacity reached 2537 gigawatts (GW) globally by the end of 2019, with the main contributors presented in Table 1.1.

Hydropower	Onshore Wind Energy	Offshore Wind Energy	Solar Energy	Bioenergy
1310	594	28	586	124

Table 1.1. Worldwide total renewable energy capacity (GW). Data from IRENA [2020].

Although offshore renewable energy capacity is still relatively small, there is a rapid increase during the last years (3 GW installed in 2010), and significant investments are constantly emerging in the offshore sector. For historical reference, the first offshore wind project was installed in Denmark in 1991.

Investments on offshore wind farms (OWFs) are growing against the well-known onshore wind farms to avoid the following shortcomings:

- Negative impact on landscape.
- Reduced energy production due to variations of wind velocity and physical blockages that might be human structures or hills.
- Noise pollution for nearby communities.
- Animal casualties, especially birds during the migration period.

On the other hand, the construction of OWFs deploys :

- Larger and more powerful wind turbines with up to 14 MW capacity as of 2020.
- Larger development areas.
- Higher wind velocities throughout the year.
- Less impact on the landscape.

1.2 Foundation Types

The primary goal for both industry and academia nowadays is to make offshore wind energy more efficient in terms of energy production, as well as in terms of design, construction, installation and decommissioning costs. In addition, innovative solutions are seeking in order to reduce the underwater wildlife impact and increase the allowable foundation depths, while floating wind turbine projects are under consideration for installation in countries with relatively deep waters (Spyridonidou et al. [2020]). Prototypes for OWTs with capacities higher than 10 Megawatts are planned for the near future, while offshore foundations may account for up to 40% of total design The available foundation types for offshore wind turbines are presented in Figure 1.2.

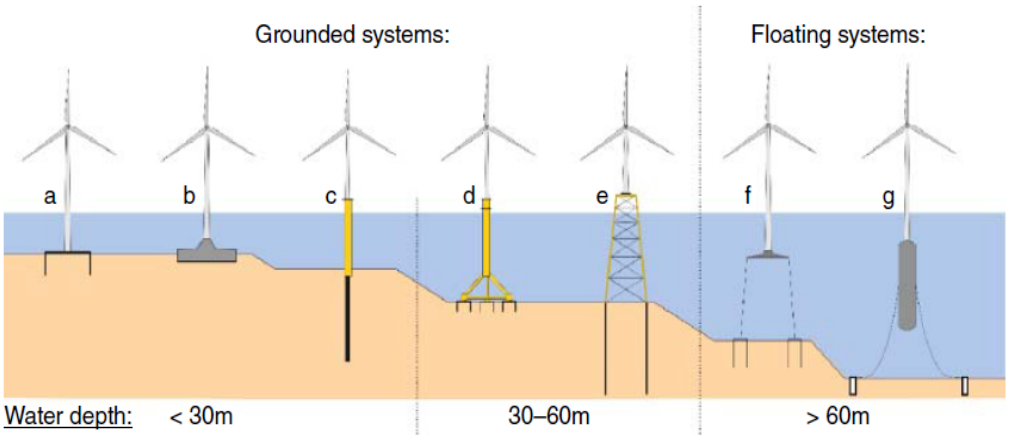

Figure 1.2. Offshore foundation types (from left to right): Monobucket, gravity based, monopile, tripod suction bucket, monopiles on jacket, floating tension leg platform, floating spar buoy, (Bhattacharya, S. [2019]).

Although monopiles are the most popular support structures for offshore wind turbines today accounting for almost 80% of the total installed offshore wind turbine foundations, this thesis is concerned with suction bucket foundations. This decision is made based on the fact that monopiles are already widely investigated and successfully employed in a large extent, while regarding suction bucket foundations the research field is wide open, considering the fact that is a relatively new concept. In addition, monopiles are preferred for shallow waters but their response and efficiency in deeper waters, where the energy potential is higher, is questionable.

1.3 Research motivation

In this study, tripod suction bucket foundations are analysed, initially proposed as an innovative solution for the offshore wind turbine sector by (Houlsby et al. [2005]). In the very same paper, the authors stated that monobuckets are uneconomic as the wind turbines are becoming sufficiently larger.

Suction buckets were primarily used for anchors in clayey soils and in a smaller extent as foundations for offshore oil and gas platforms. It is evident that the structural response and the loading regime as support structures for wind turbines varies greatly compared to the oil and gas platforms. Thus extended research is required for a safe and resilient design.

During the installation, the bucket is driven through the soil by it's self-weight and afterwards suction is applied mechanically, which will create the required pressure difference for the complete installation.

Suction bucket foundations are already in mass production and installed in the North Sea successively. Although, these areas are on a grand scale seismically inactive, while areas like Japan and Taiwan where suction buckets are planned to be installed are heavily prone to seismic events. This study is an attempt to provide an insight on the response of tripod suction buckets founded in the vicinity of active faults. During an earthquake event, the dip-slip or strike-slip rupture of an existing fault generates permanent offsets of quasi-static nature which may interact with the foundation. This topic -to the knowledge of the writer- has not been adequately investigated yet, and this condition leads naturally to the problem statement of the present thesis:

What is the effect of dip-slip fault rupture on tripod suction bucket foundations?

Literature Review 2

In this chapter, the theoretical background of this study is presented. Also, a brief literature review on the topic is mentioned and discussed.

2.1 Faults

The theory of this section is largely based on (Kramer [1996]).

The movement between two portions of the earth's crust will occur on new or preexisting offsets in the geological structure of the crust, known as faults. Faults may range from several meters to hundreds of kilometers in length and extend from the surface to some kilometers on the subsurface. An active fault can cause an earthquake excitation, or even aseismically a movement may occur.

In a seismic event, the rupture of an earthquake fault generates two types of ground displacement; permanent quasi-static offsets on the fault itself and transient dynamic oscillations away from the fault (Anastasopoulos and Gazetas [2007*a*]). The second type of displacement is the result of waves originating successively at each "point" of the fault as the "slippage" takes place, and they propagate over large distances in the earth. These waves are affecting the ground surface and the structures founded on it. In contrast, the permanent offset on a fault affects the ground surface only if the rupture extends all the way to the surface. While the earthquake induced ground oscillations are widely examined and investigated, less effort has been devoted to understand the effect of fault-rupturing seismic fault on the overlying soil and the structures founded on it.

2.1.1 Fault Geometry

The surface of a fault can be approximated as a plane. The orientation of it can be described by its strike and dip. The strike of a fault is the horizontal line produced by the intersection of the fault plane and a horizontal plane, as shown in Figure 2.1. The downward slope of the fault plane is described by the dip angle, which is the angle between the fault plane and the horizontal plane measured perpendicular to the strike. A completely vertical fault will have, naturally, a dip angle of 90 °.

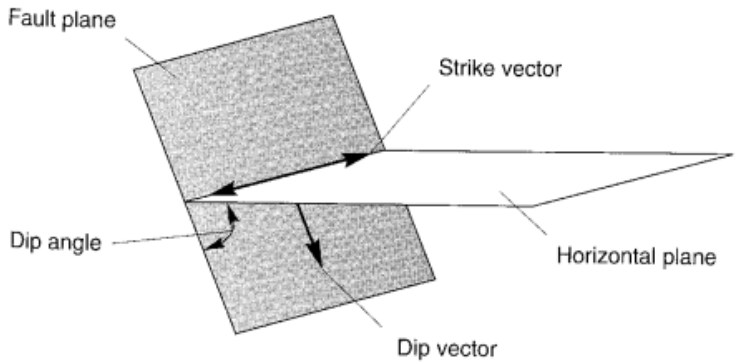

Figure 2.1. Fault plane orientation, (Kramer [1996]).

2.1.2 Fault Movement

If the fault movement occurs in the direction of the dip is referred to as dip-slip movement. In this study, dip slip movements are examined. According to the direction of movement, a dip slip fault can be either normal or reverse.

A normal dip-slip fault occurs when the material above the inclined fault (called hanging wall from now on) moves downward with respect to the material below the fault (called footwall from now on). This type of fault is mainly associated with tensile stresses in the crust.

A reverse dip-slip fault occurs when the horizontal component of dip-slip movement and the hanging wall is moving upwards relative to the foot wall. This type of fault is associated with compressive stresses. A typical normal and reverse fault illustration is shown in Figures 2.2 and 2.3, respectively.

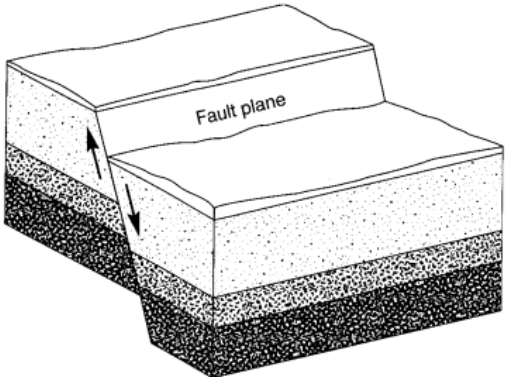

Figure 2.2. Normal fault, (Kramer [1996]).

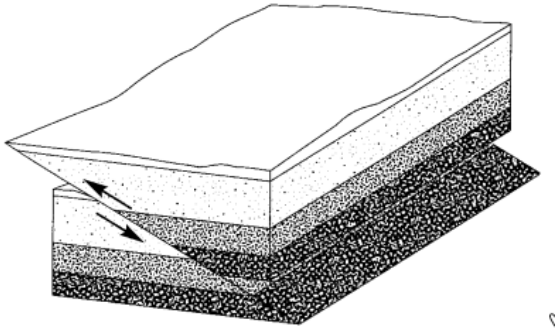

Figure 2.3. Reverse fault, (Kramer [1996]).

If the fault movement is occurring parallel to the strike is called strike-slip movement, see Figure 2.4. These type of movements are out of the scope of this study. Hence, no further theory is presented.

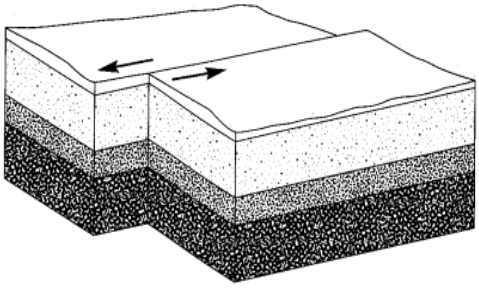

Figure 2.4. Left lateral strike-slip fault, (Kramer [1996]).

2.2 Kocaeli 1999 Earthquake Case Study

In 1999, the devastating Izmit earthquake triggered by reactivation of the strike slip North Anatolian Fault leading to M_w 7.4 moment magnitude and causing 17000 casualties (Marza [2014]). This led to the collapse or serious damage of multiple structures, while many of these were crossed by the surface rupture and aroused the curiosity of several researchers.

A number of papers were published, (Anastasopoulos and Gazetas [2007*a*],Anastasopoulos and Gazetas [2007*b*]), enlightening the existing knowledge on Fault Rupture-Soil-Foundation-Structure Interaction (from now on FR-SFSI) and was the initiative for numerous analytical and very well documented studies on this phenomenon by the same research team. These studies are briefly reviewed in this section.

Although practice codes like Eurocode 8 demand that *"buildings and important structures not to be erected in the vicinity of active fault"*, this is difficult to achieve. Some reasons why this is difficult to achieve are outlined in (Anastasopoulos and Gazetas [2007*a*]):

1. Difficulty to determine reliably which of the faults are potentially active.

2. Along the fault outcrop (surface break of the fault), ruptures are neither continuous nor do they follow precisely the surface outcrop of existing faults.

3. Fault outcrop depends not only on the magnitude and type of fault rupture, but also on the overlying soil characteristics. Deep and loose soils are less prone to outcrop against cohesive with small thickness soils.

4. The presence of the structure may modify the rupture path, leading to a possible complete diversion of it.

(Anastasopoulos and Gazetas [2007*a*]) performed a case study in a number of structures close to an approximately 2 meters normal fault. It needs to be stated that the main faulting mechanism in this case was strike-slip fault which locally converted into a normal fault. In Figure 2.5 a sketch of the study area is presented.

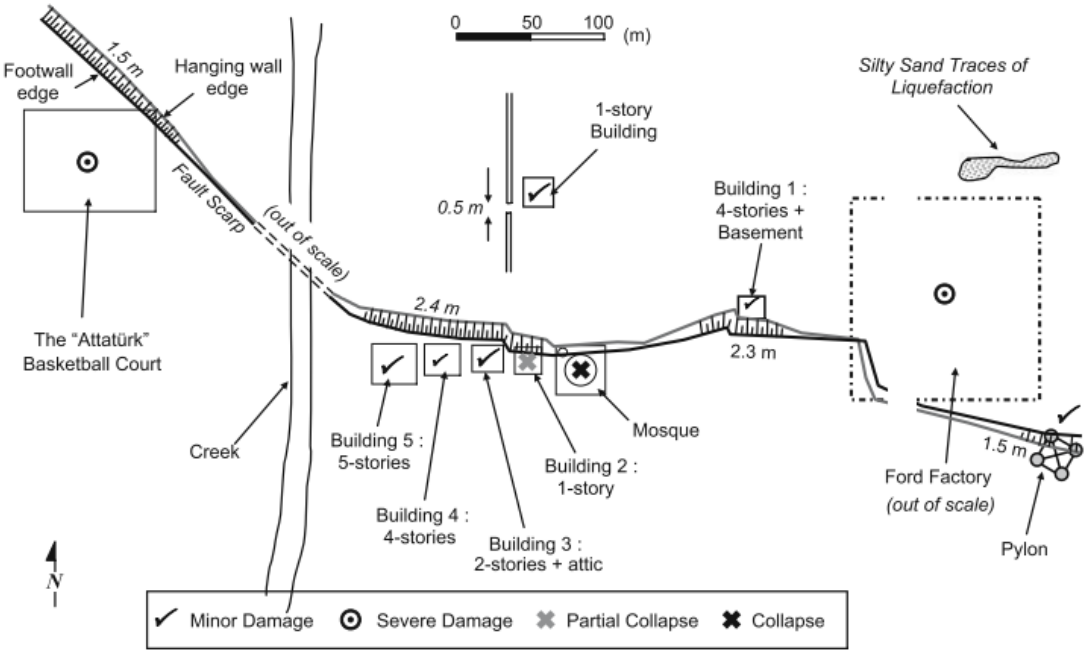

Figure 2.5. Plan view of Kocaeli investigation area with the normal fault trace, (Anastasopoulos and Gazetas [2007*a*]).

As it is visible in Figure 2.5, the surface rupture appeared to deviate from its original path, "avoiding" crossing the structures. It is very important to clear out that the soil conditions in the area do not alter significantly. Thus, the different structural response and the deviation of the path is attributed only on differences in foundation and structural rigidity.

Building 1 is first analysed. It is a 4-story reinforced-concrete structure with basement. The rupture diverted and avoided the structure, causing only flooding of its basement even though the dislocation was relatively large; 2.3 meters vertical and 1.1 meter horizontal. Thus, this is an indication that a strong structure built across a fault causes diversion of the fault.

Secondly, the Mosque is analysed. In this case, no visible fault scrap was evident, but it was expressed through differential settlement. This structure partially collapsed and then demolished since the damages were not economically feasible to repair. It was founded on several isolated footings, without shear walls or stiff tie beams and a superstructure of reinforced-concrete. Since the Mosque is obviously less stiff than Building 1, the differential settlement was transmitted unaltered to the superstructure and led to serious damages.

The next case is Building 2. This was a poorly constructed 1-story structure, with wooden-tile covered roof supported directly on cinder blocks. Between the roof and the walls, concrete beams were evident, although poorly reinforced. The building did not have a foundation. This structure was torn apart by the rupture, see Figure 2.6. Given the very limited tensile resistance of the cinder blocks, the part crossed by the rupture collapsed but the rest of it was left intact, avoiding total collapse and possible casualties.

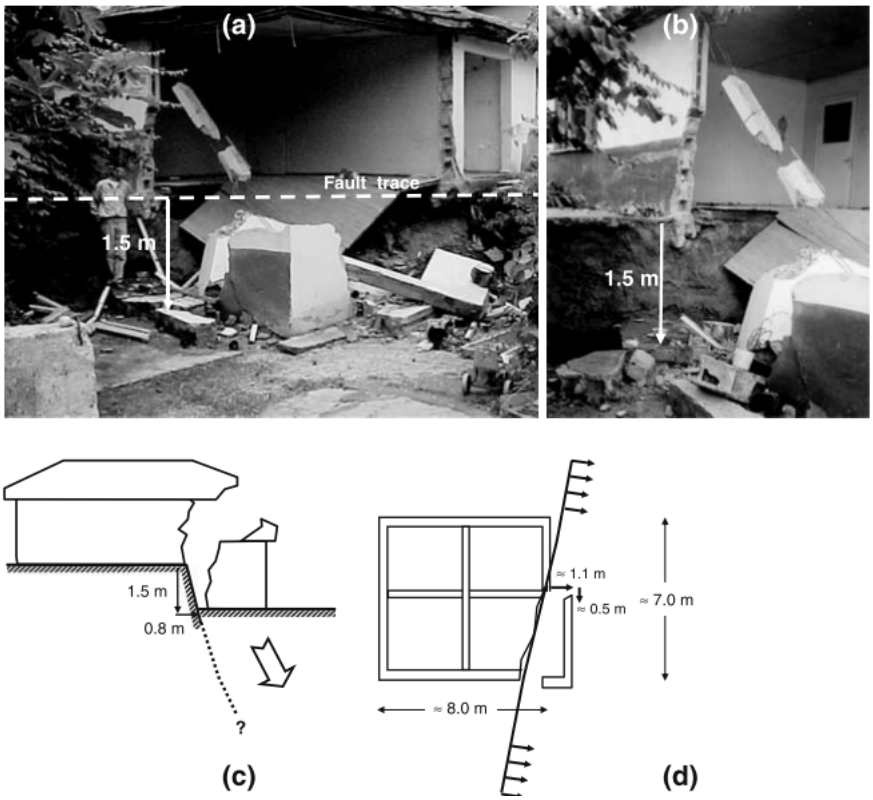

Figure 2.6. Building 2 partial collapse. Photos, schematic cross section and plan view, (Anastasopoulos and Gazetas [2007*a*]).

Afterwards, Building 3 managed to survive the fault rupture without damage, except some minor cracks on the brick wall. Most importantly, it seems that the presence of the building which is founded on the footwall diverted the rupture path. This building is a 2-story reinforced concrete structure with an attic, founded on a box type foundation system comprising stiff concrete beams between a mat and a top slab. The rigidity and stiffness of this foundation type saved the structure from any detrimental damages.

One more structure analysed in (Anastasopoulos and Gazetas [2007*a*]) is the "Ataturk" basketball court. This court had just been constructed when the earthquake happened. The rupture crossed its northeast corner causing significant damage due to the differential tectonic displacement, see Figure 2.7, leading to demolition since it was claimed to be damaged beyond the limit of repair. Its concrete shear walls failed, while the non-bearing bricks were cracked indicating tensile failure due to differential displacement. Some of the piles failed completely and were totally detached from the pile cap. The structural system comprised of shear-wall type columns positioned along the perimeter and each column is founded through 2 x 2 pile groups connected together with a 1.2 meters in thickness pile cap.

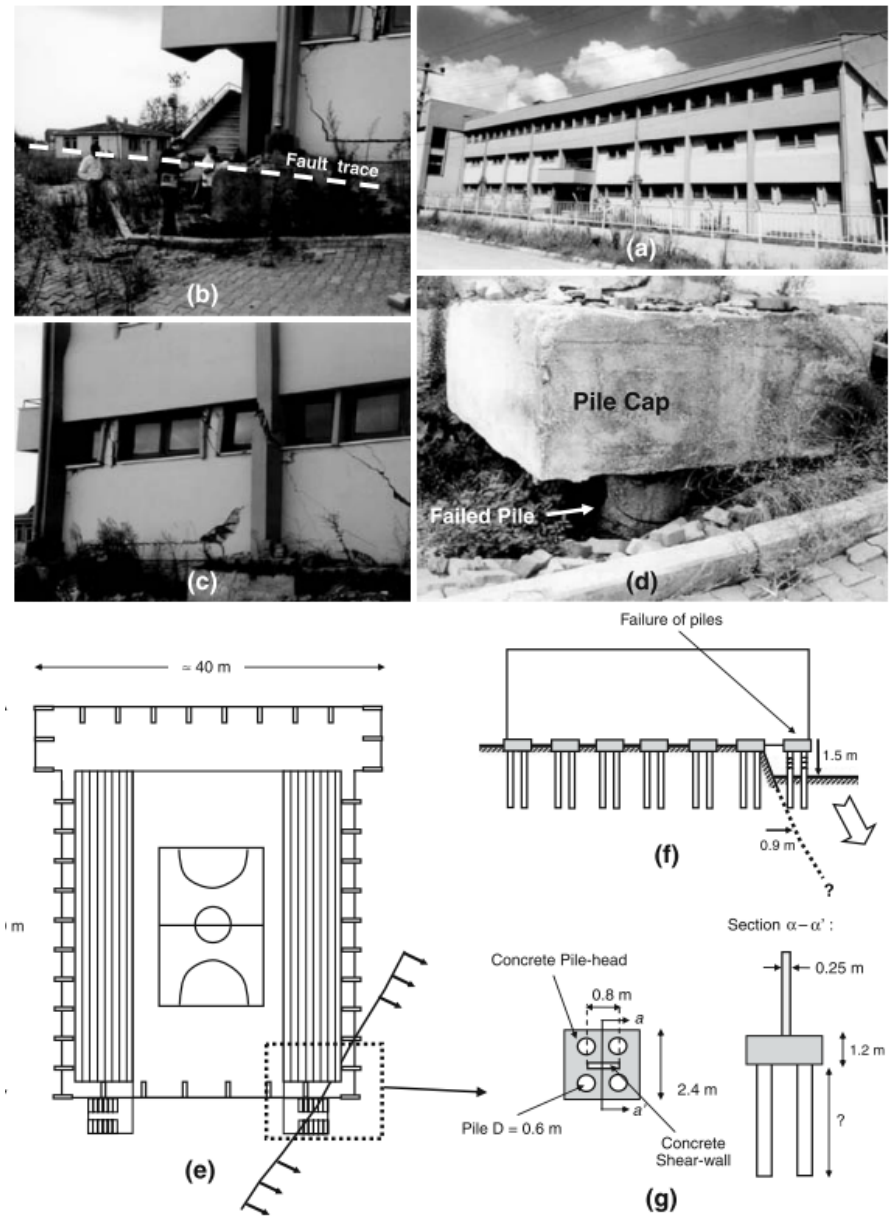

Figure 2.7. "Attaturk" basketball court severe damages, photos and schematic plan view and cross sections, (Anastasopoulos and Gazetas [2007*a*]).

The main conclusions of the study regarding the structural response close to the fault rupture are presented herein:

1. Structures supported on rigid mat or box-type foundations performed quite well causing the rupture path to divert, in contrast to those founded on isolated footings or piles.

2. Buildings with isolated footings allow the dislocation to emerge within the structure, causing significant deformation and distress.

3. Structures founded on path tend to force the superstructure to follow the imposed deformation. Even though they might are adequately designed and constructed, pile foundations play a detrimental role.

In (Anastasopoulos and Gazetas [2007*b*]), the same case study is analysed numerically and experimentally in order to confirm the field observations. This analysis is presented herein.

The researchers used two-dimensional (2D) plane strain Finite Element Analysis in order to investigate the FR-SFSI. The soil deposit was uniform, at the base of which a normal fault with a specific dipping angle α produced downward displacement with a vertical component h. To avoid boundary effects, the width of the model was four times higher than the soil deposit thickness. Also, a finer mesh is employed in the center of the model, where the fault is expected to outcrop.

A modified Mohr-Coulomb failure criterion with isotropic strain hardening is applied, by introducing the mobilised friction and dilatancy angles, ϕ_{mob} and ψ_{mob}, respectively. The soil parameters were calibrated through direct shear test.

Firstly, (Anastasopoulos and Gazetas [2007*b*]) validated their model in terms of fault rupture propagation in the free field comparing the developed FEA model and a series of centrifuge tests conducted at the University of Dundee. The modelling technique predicted correctly both the location of fault outcropping and the displacement profile at the ground surface. For more information about the model validation, refer to Anastasopoulos et al. [2007].

At a second stage, the buildings of the Kocaeli earthquake case study were analysed. In favor of simplicity and avoiding complexities, the superstructure structural system of all buildings (except Building 2) were assumed exactly the same, with the only difference being in the number of stories and of course the surcharge load and the foundation type. In order to investigate the foundation type effect, the surcharge load kept constant, while in order to investigate surcharge load effect, the foundation types assumed as invariably box-type. A dip angle $\alpha = 60^{\circ}$ is employed. A detailed explanation of the numerical analysis results for each specific case is outside of the scope of this thesis. Thus, only the main conclusions are outlined:

1. The developed FEA model, assuming a modified Mohr-Coulomb scheme is in qualitative agreement with reality. The performed centrifuge tests confirm this.

2. Structures founded on continuous rigid mat or box-type foundations perform better than the ones isolated footings or piles.

3. Structures founded on continuous rigid mat or box-type foundations may force the fault outcropping to divert. Otherwise, the stiffness of those foundations spread the deformation and allow the structure to rotate as rigid body.

4. Structures founded on isolated footings allow the rupture to outcrop within the limits of the building imposing substantial distress and distortion.

5. Piles without a cap may divert the dislocation but also force the superstructure to follow the imposed deformation; the structure is not relieved by losing contract with the deformed soil surface, as in the case of rigid mat or box-type foundations, causing extensive damages on the superstructure.

6. The effect of the surcharge load q is very important. The increase of q alternates the stresses beneath the foundation and hence the diversion of the dislocation. Since the soil beneath the structure is of higher strength, the rupture tends to "avoid" it and diverts.

7. Structures in the vicinity of active faults can be designed to withstand tectonic dislocations. The secret is, to be founded on continuous, stiff and rigid foundations. Unlikely, isolated footing and even piles can be detrimental in such cases.

(Anastasopoulos et al. [2008]) performed numerical analyses of fault-foundation interaction. Three different FEA methods were employed and calibrated through already available data. The first method uses the commercial FEA program Plaxis in combination with a non-associated elastic-perfectly plastic Mohr-Coulomb constitutive model. The second method uses the commercial FEA program Abaqus combined with a modified Mohr-Coulomb constitutive model that takes into account strain softening, while the third method uses the FEA code Dynaflow along with a more complex multi-yield constitutive model. For more information about the soil and foundation models, refer to (Anastasopoulos et al. [2008]).

The calibrated models were verified against centrifuge tests with an acceptable agreement and therefore the second method was used to develop a parametric study. The soil compliance, the surcharge load q and the distance s between the free field fault outcrop and the foundation varied. The main conclusions are:

1. The increase of the surcharge load q amplifies the diversion of the rupture path. In addition, "smooths" the settlement profile leading to a decrease of the detached regions of the foundation.

2. The increase of soil compliance (looser soils) is always beneficial since structures founded on loose sand experience far less separation than dense sand.

3. The rotation of the structure maximizes when the rupture outcrops close to the middle of the foundation and is minimized when the rupture emerges near the edge of the structure that is closest to the hanging wall.

A similar study for strip foundations can be found in (Anastasopoulos et al. [2009]), and for piled foundations in (Anastasopoulos et al. [2013]).

To the knowledge of the writer, the one and only investigation including caisson foundations and fault rupture is published by (Loli et al. [2011]). Although the mentioned study does not have many similarities with the study presented in this thesis, it will be briefly introduced to clear out the need of further enlightenment on the topic examined.

(Loli et al. [2011]) investigated the response of a single caisson foundation during reverse fault rupture located in Min-Chien City, Taiwan. The structure was crossed by Chelingpu fault during Chi-Chi earthquake and was subjected to a relative displacement of approximately 4 meters. The structure can be seen in Figure 2.8.

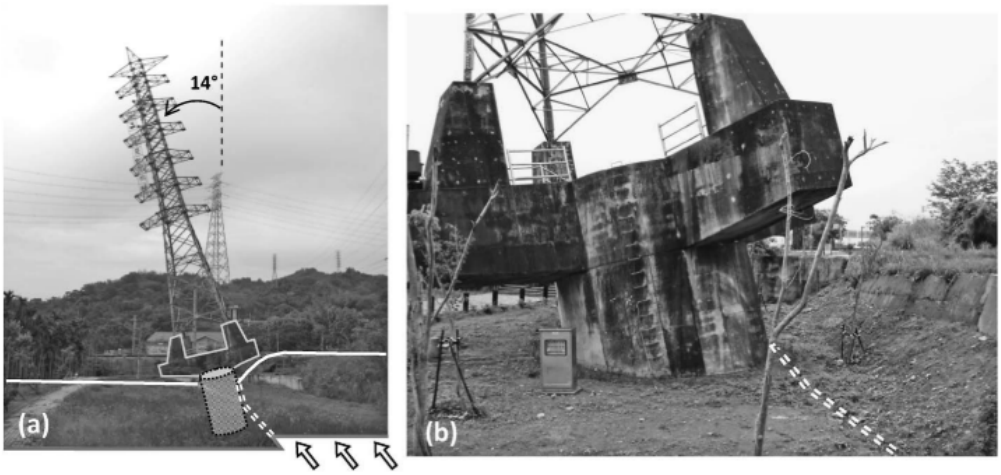

Figure 2.8. Reverse fault rupture interaction with a caisson foundation: (a) electricity pylon crossed by the fault; (b) closer view of the caisson, (Loli et al. [2011]).

The fault rupture diverted to the hanging wall due to its interaction with the caisson, while the electricity pylon remained stationary on the foot wall experiencing large rigid-body rotation. The foundation had 5 meters of breadth and length and 10 meters of embedded depth supported on a 15 meters layer of sand with relative density equal to 80%. The dead weight of the superstructure was 20 MN and the dip angle 60°.

A series of centrifuge tests were conducted in University of Dundee with variance of the distance between the caisson and the free field fault rupture outcrop. Also, a numerical model was developed in the FEA program Abaqus to verify the response, using a refined mesh close to the foundation and a Mohr-Coulomb constitutive model with strain softening. The soil-caisson interface was modelled using contact elements allowing sliding and/or detachment to occur.

The FE model showed acceptable agreement with the centrifuge tests, as it can be seen in Figures 2.9 for the free field and 2.10 with the presence of the structure.

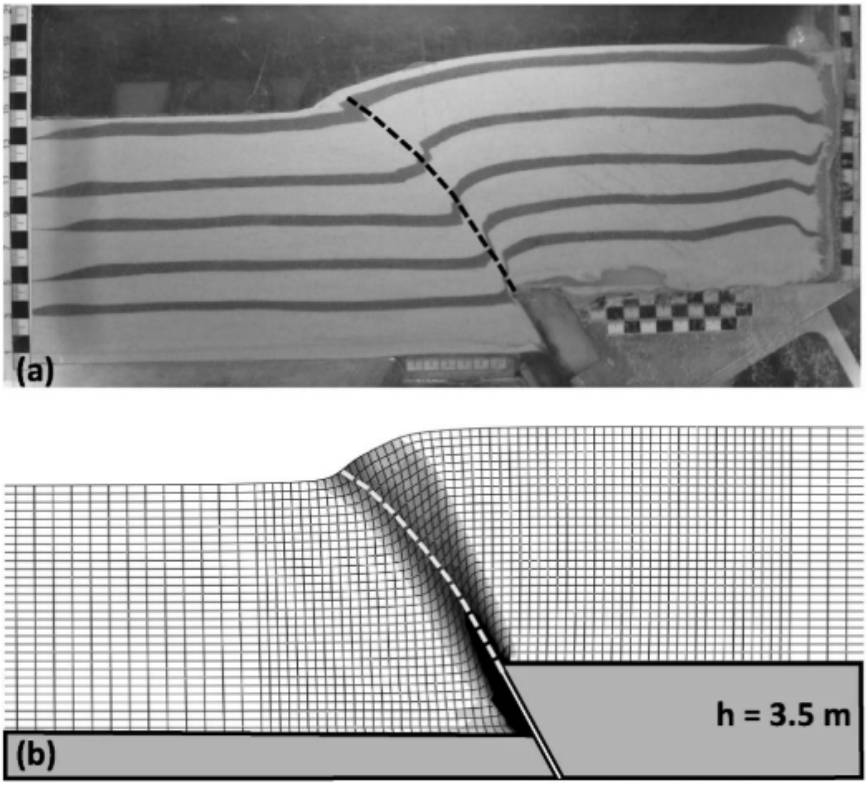

Figure 2.9. Soil model deformation in the free field; (a) centrifuge model and (b) FE deformed mesh for fault throw 3.5 meters, (Loli et al. [2011]).

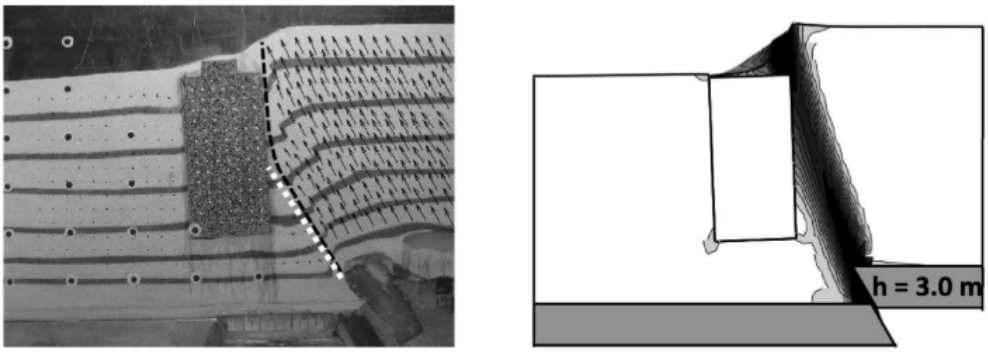

Figure 2.10. Fault rupture-caisson interaction mechanisms for s/B=-0.78; centrifuge model (left) and FE deformed mesh (right), (Loli et al. [2011]).

Afterwards, a parametric study is conducted to study the effect of the exact caisson position relative to the fault outcrop. The key conclusions of this report are:

1. The employed numerical model captures the reality in a good manner with validation against centrifuge tests.

2. The caisson acted as a kinematic constraint, causing complete diversion of the fault rupture path and forced it to develop outside the foundation margins.

3. The response is sensitive to the position of the foundation relative to the free field rupture.

4. The caisson's zone of influence is widespread, leading to a need for wide lateral boundaries to eliminate unwanted boundary effects.

Finally, (Gazetas et al. [2008]) summarized Quaker project findings and proposed some preliminary design recommendations for dip-slip fault-foundation interaction problems which can be employed in future structural codes. In addition, further studies were conducted on numerical and experimental behavior of fault ruptures and the reader can refer to them for further information (Rokonuzzaman et al. [2009], Rokonuzzaman et al. [2014], Bransby, Davies and Nahas [2008], Bransby, Davies, Nahas and Nagaoka [2008]).

After this brief literature review, it is evident that even the numerous papers published about FR-SFSI, the fault rupture-suction bucket interaction is not examined yet. This thesis will attempt to cover this knowledge gap and provide some valuable preliminary insight on the mechanisms involved in it.

Validation of Analysis Methodology 3

In this chapter, a validation of the constitutive and numerical model is presented. Firstly, the soil model used is briefly introduced based on (Plaxis [2020b]). Afterwards, the free field response for both normal and reverse fault rupture is compared with results published in the literature.

3.1 Plaxis 3D

The choice of Finite Element Analysis software depends on the problem formulation, the desired outcome, any limitations that may occur and the accessibility to it. Although several FEA programs are available, both commercial and open-source, Plaxis 3D is used for this thesis. For the purpose of this investigation, Plaxis fulfills all the necessary demands to obtain the desired outcome. In addition, provides a user-friendly interface and several in-build constitutive models. Although the free field analysis can be done in 2-dimensional analysis, the parametric study with the presence of the tripod suction bucket demands -as expected- 3-dimensional analysis. For this reason, all the calculations are conducted in a 3D domain.

Plaxis 3D uses 10-node tetrahedral elements for soil modelling, see Figure 3.1.

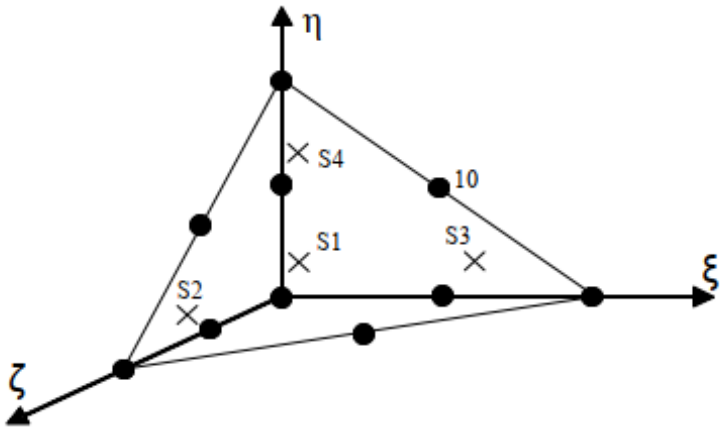

Figure 3.1. 3D soil elements, (Plaxis [2020*a*]).

In order to model the structure and Soil-Structure Interaction, special types of elements are used:

- Beams: 3-node line elements compatible with the 3-node edges of a soil element.
- Plates and geogrids: 6-node plate and geogrid elements.
- Soil-Structure Interaction: 12 node interface elements.

3.2 Hardening Soil Model with Small Strain Stiffness

The Hardening Soil Model with Small Strain Stiffness (herein HSsmall for brevity) constitutive model is implemented in Plaxis 3D for the performed numerical analysis. HSsmall is an advanced non-linear elastoplastic model based on Hardening Soil model, sharing the same parameters and including two additional:

- The initial very small-strain shear modulus G_0.
- The shear strain level $\gamma_{0.7}$ at which the secant shear modulus G_s is reduced to about 70% of G_0.

As opposed to classic, first-order approximation of soil behavior models like Mohr-Coulomb, the yield surface of a hardening plasticity model can expand in principal stress space due to plastic straining. This characteristic is allowing HSsmall model to capture the response of dip-slip fault rupture propagation through sand in a qualitatively acceptable way.

Two types of hardening are present, namely shear and compression hardening. Shear hardening is used to model irreversible strains due to primary loading, while compression hardening is used to model irreversible plastic strains due to primary compression in oedometer and isotropic loading. The yield contour is presented in Figure 3.2.

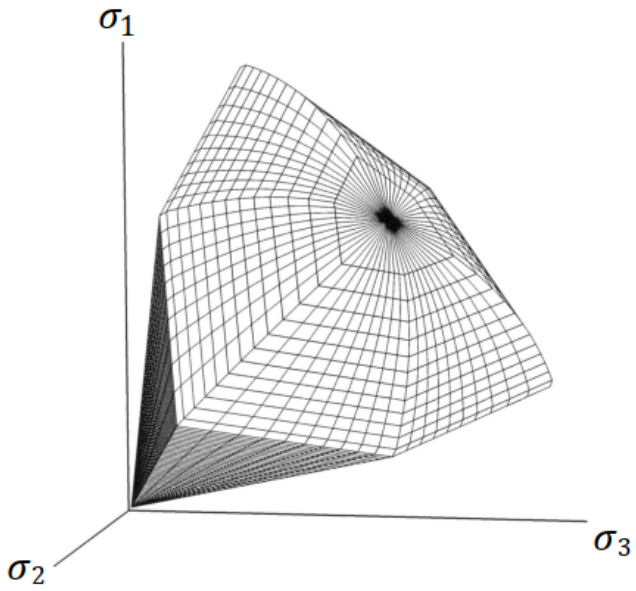

Figure 3.2. Representation of total yield contour of Hardening Soil model in principal stress space for cohesionless soil, (Plaxis [2020*b*]).

While Hardening Soil model which forms the basis of HSsmall assumes linear elastic material behavior during unloading-reloading, the strain range in which the soil is truly elastic is very small. With increasing strain amplitude, soil stiffness decays non-linearly, as is illustrated in Figure 3.3, which indicates that at the minimum strain which can be reliably measured in classical laboratory tests, soil stiffness is decreased to less than half its initial value. This fact is treated by HSsmall model, in which very small strain soil stiffness and its non-linear dependency on strain amplitude is taken into account.

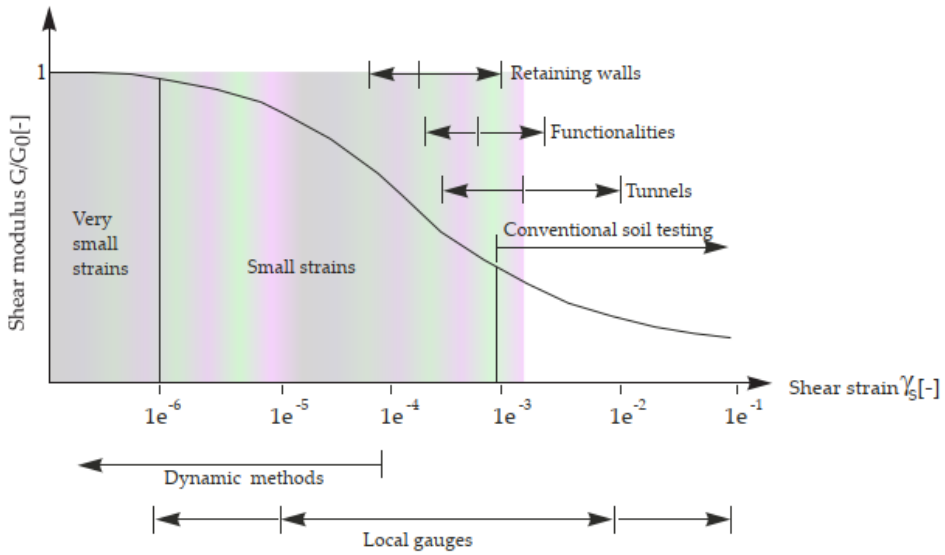

Figure 3.3. Stiffness-strain behavior of soil with typical strain ranges for laboratory tests and structures, (Plaxis [2020*b*]).

In this thesis, HSsmall parameters calibrated against monotonic centrifuge test by (K. Glitrup and L.R. Christiansen [2019]), and further used by (K. Nielsen [2020]) are employed. The parameters used for the calculations in Plaxis 3D can be seen in Table 3.1. Further details on each parameter, detailed background theory of HSsmall and the calibration technique can be found in Appendix A.

Parameter	Value	Units
D_r	75.80	%
γ_{sat}	19.01	kN/m^3
γ_{unsat}	14.81	kN/m^3
ϕ'	39.18	°
ψ	9.18	°
c'	0.20	kPa
E_{50}^{ref}	16235	kPa
E_{ur}^{ref}	48705	kPa
E_{oed}^{ref}	12988	kPa
G_0^{ref}	43387	kPa
γ_{07}	$3.44{\cdot}10^{-4}$	[-]
m	0.80	[-]
K_0	0.37	[-]
ν_{ur}	0.27	[-]
R_f	0.95	[-]
R_{inter}	0.48	[-]

Table 3.1. Calibrated parameters for HSsmall, by (K. Glitrup and L.R. Christiansen [2019]).

3.3 Comparison Data

The free-field propagation of dip-slip fault rupture is examined. Finite Element Analysis commercial program Plaxis 3D is employed and the results are compared with centrifuge tests conducted in the beam centrifuge at University of Dundee and with a Finite Element Analysis with a modified Mohr-Coulomb soil model in Abaqus software.

The data for the centrifuge tests and the FEA can be found in (Anastasopoulos et al. [2007]), where four different types of tests are presented, modelling both normal as well as reverse fault ruptures. The soil depth was approximately 25 meters while the other dimensions were varied, depending on the centrifugal acceleration. Table 3.2 illustrates the basic parameters and prototype dimensions of centrifuge experiments, while a photograph and basic dimensions of the experimental apparatus is presented in Figure 3.4.

Test	Fault type	g	D_r	H (m)	L (m)	W (m)	h_{max}(m)
4	Normal	100	80.0	25.0	68.0	20.0	1.91
3	Reverse	100	83.9	25.0	68.0	20.0	2.22
12	Normal	115	60.2	24.7	75.7	23.5	3.15
8	Reverse	115	60.9	24.5	75.7	23.5	2.56

Table 3.2. Summary of Basic Parameters and Prototype Dimension of Centrifuge Experiments, after (Anastasopoulos et al. [2007]).

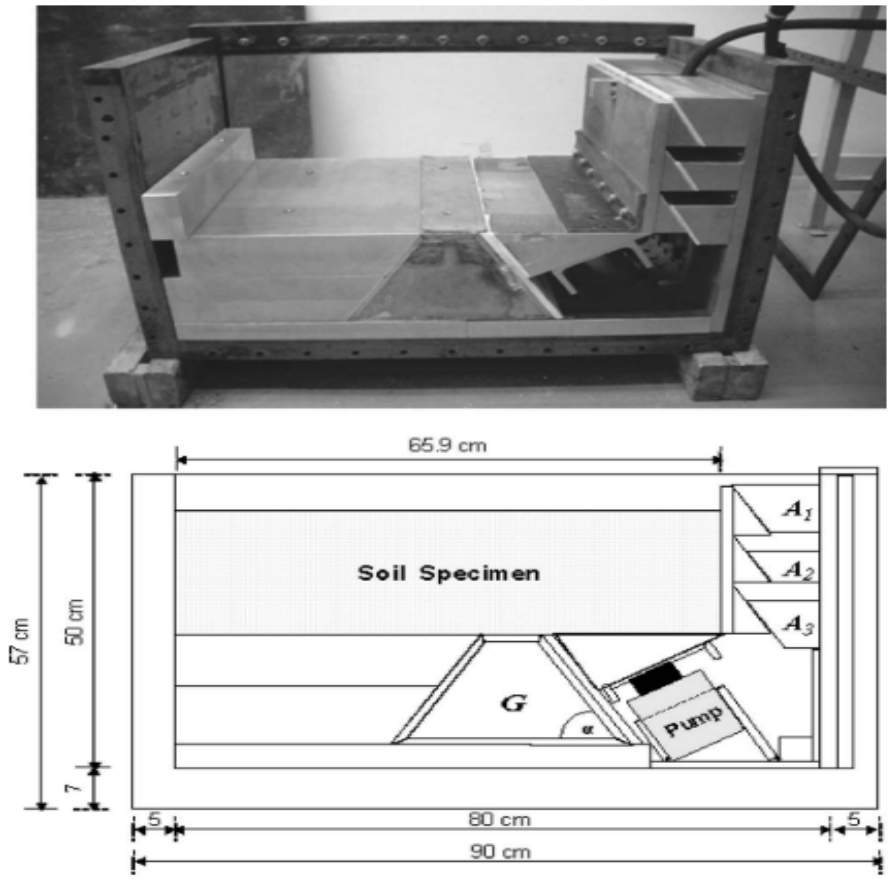

Figure 3.4. Photograph and basic dimensions of centrifuge experimental apparatus installed in Dundee University, (Anastasopoulos et al. [2007]).

As it is already mentioned, the calibrated HSsmall parameters used in this study are accounting for D_r equal to 75.8 %. Hence, the results from the numerical analysis are compared to Tests 3 and 4, see Table 3.2. Although the relative density is not precisely the same, the deviations are expected to be small and the proposed comparison is assumed to be valid.

The available data are presented in Figures 3.5 and 3.6 and will later form the basis for the verification of the proposed model. Note that the data points are extracted from the literature and edited for improved visualization. These plots will later be one form of comparison against the Finite Element Analysis with HSsmall, for the validation of the free field response before the parametric study with the presence of the tripod suction bucket.

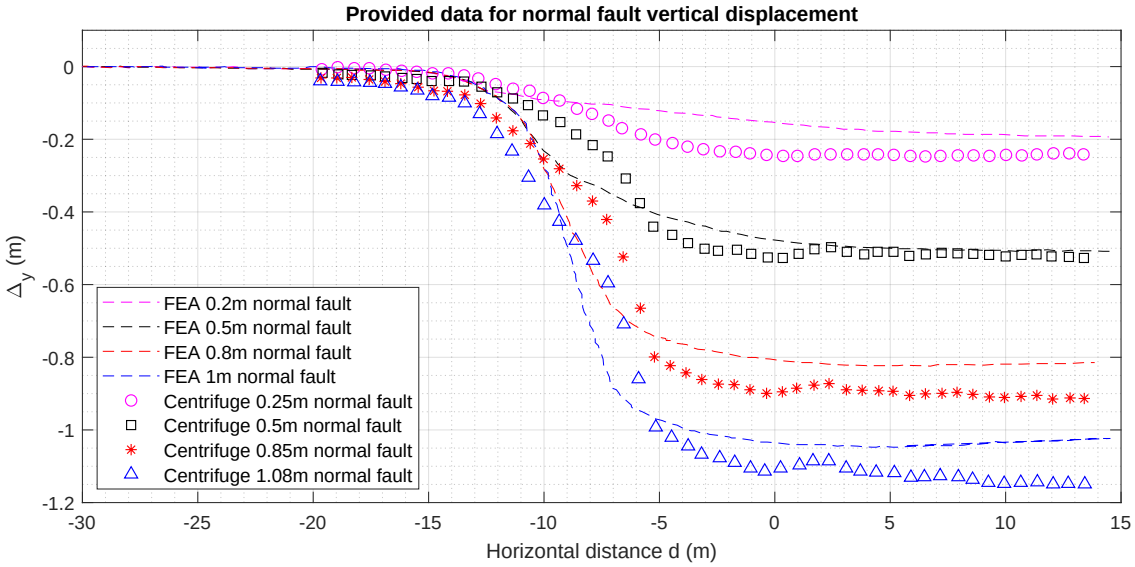

Figure 3.5. Provided $\Delta_y - d$ plots for normal fault, edited after (Anastasopoulos et al. [2007]).

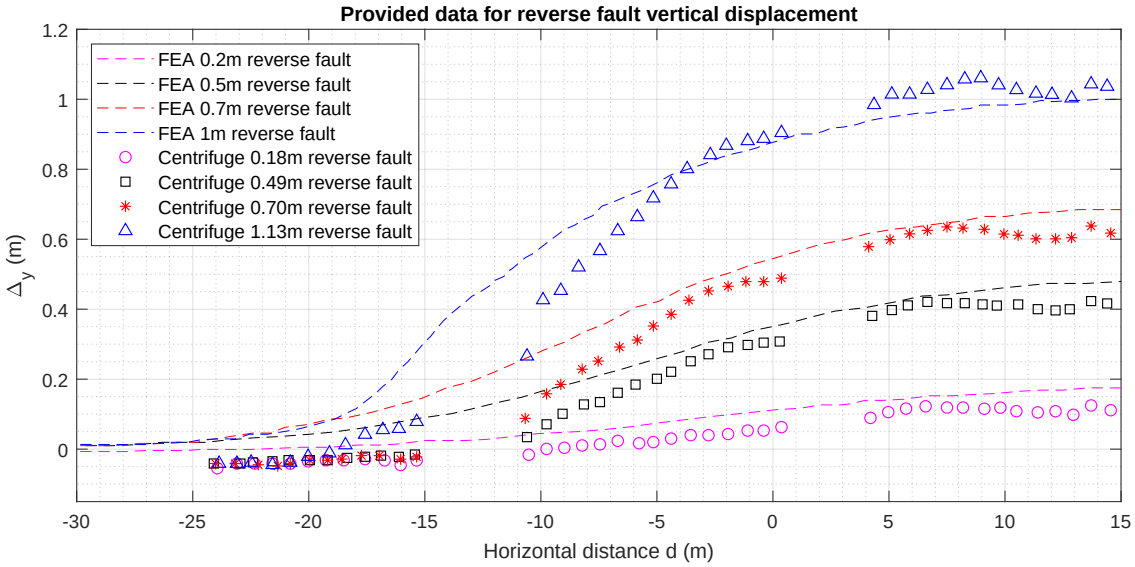

Figure 3.6. Provided $\Delta_y - d$ plots for reverse fault, edited after (Anastasopoulos et al. [2007]).

The other form of comparison to verify the accuracy of the proposed soil model and modelling technique is based on plastic shear strain band from the fault. Photographs from the centrifuge experiments indicating the development and outcropping of the rupture to the surface are available for normal and reverse fault, with 1.08 meters and 1.13 meters bedrock dislocation, see Figures 3.7, 3.8, respectively. In addition, the deformed mesh with superimposed plastic shear strain contours obtained from the Finite Element Analysis with the modified Mohr-Coulomb model in Abaqus is available, see Figure

3.9.

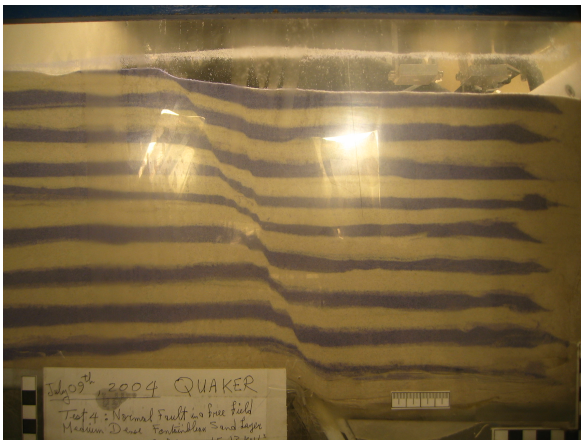

Figure 3.7. Soil deformation for $h = 1.08m$ normal fault on centrifuge test with $D_r = 80\%$.

Figure 3.8. Soil deformation for $h = 1.13m$ reverse fault on centrifuge test with $D_r = 83.9\%$.

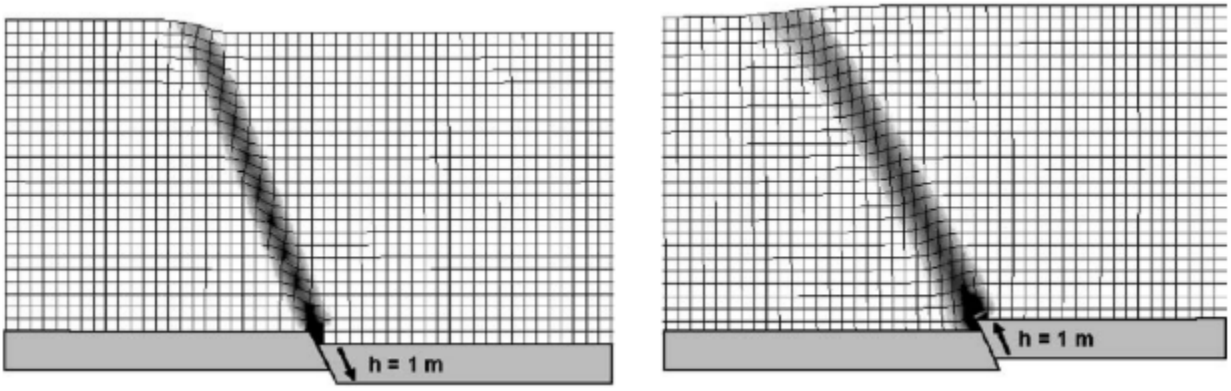

Figure 3.9. FE deformed mesh with plastic shear strain concentration for normal (left), reverse (right) fault, $h = 1m$ and $D_r = 80\%$, (Anastasopoulos et al. [2007]).

A summary of the modelled dislocations in Plaxis 3D with respect to the type of fault is presented in Table 3.3. Note that if there is inconsistency between the provided FEA and centrifuge analysis, e.g. $h = 1.13m$ for the centrifuge and $h = 1m$ for the FEA model, the median value is taken for the proposed HSsmall model.

Fault type	**Bedrock offset h (m)**			
Normal	0.225	0.50	0.825	1.04
Reverse	0.19	0.50	0.70	1.07

Table 3.3. Type of fault and bedrock offsets modelled.

3.4 Numerical model

In order to validate the free field response, a numerical model is constructed in Plaxis 3D Finite Element Analysis software, using 10-node tetrahedral elements for soil modelling. The model for reverse fault is pictured in Figure 3.10. Same modelling techniques is followed for normal fault, with the only difference being the signs of h and x parameters.

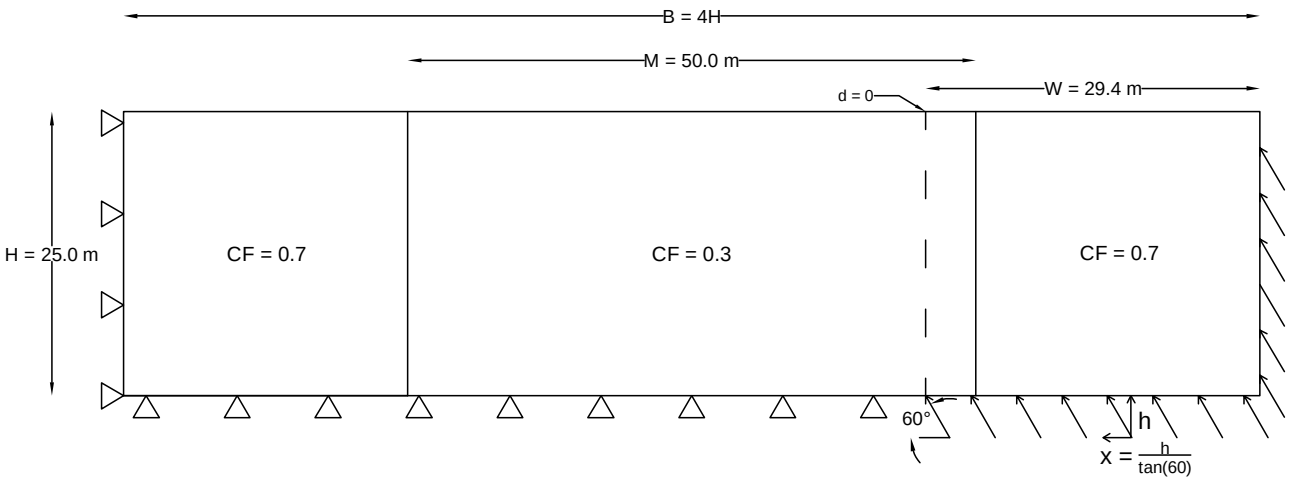

Figure 3.10. 2D representation of the numerical model.

The model refers to a uniform sand soil deposit of thickness $H = 25m$, at the base and the side of which a dip-slip fault, dipping at an angle $\alpha = 60°$ measured from the horizontal, ruptures and produces downwards for normal or upwards for reverse fault displacement with a varying vertical component h. Since Plaxis 3D does not have the option for prescribed displacement with an angle, the vertical component is modelled independently of the horizontal, which is calculated as $x = h/tan(\alpha)$ in order to produce the desired resultant bedrock dislocation.

The coordinate $d = 0m$ is the position of bedrock dislocation appliance, and is located at $W = 29.4m$ from the model's right boundary along x-axis. This is selected in order to duplicate exactly the modelling conditions of the centrifuge test results provided, which are the references for the free field response verification.

A visualisation of the 3D model with the coordinate system and the applied displacements for reverse fault is depicted in Figure 3.11.

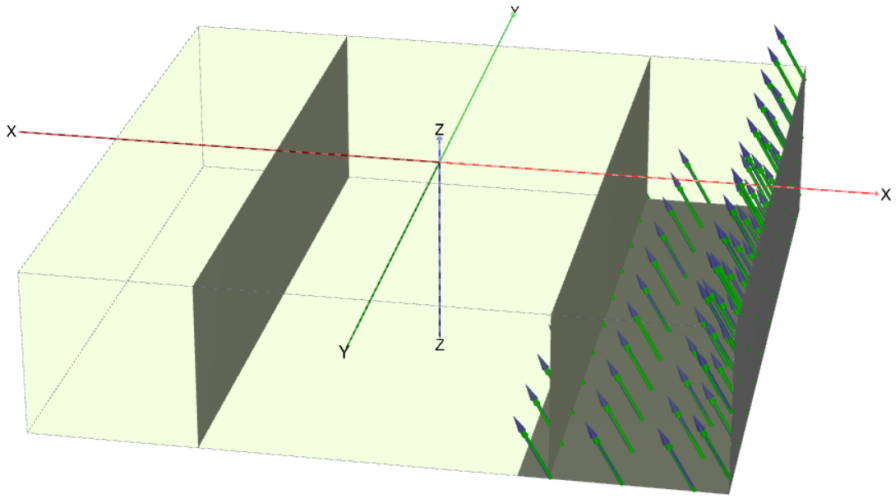

Figure 3.11. 3D model view with the applied displacement and the coordinate system displayed.

The width of the model is equal to $B = 4H$ in order to avoid the undesired parasitic boundary effects. During the verification of the free field model, it was shown that the boundary conditions play significant role to the calculation outcome. Of course, as expected the boundary conditions are overlapped

from the applied displacement at the points which is applied. Multiple combinations are modelled and the most accurate results are observed with the following boundary conditions:

- Boundary X_{min}: Normally fixed
- Boundary X_{max}: Horizontally fixed
- Boundary Y_{min}: Normally fixed
- Boundary Y_{max}: Normally fixed
- Boundary Z_{min}: Vertically fixed
- Boundary Z_{max}: Free

As previous studies have shown, the density of the mesh and the element size plays a significant role on the calculation outcomes and contribute on avoiding the Finite Element Analysis shortcomings. Specifically, in fault rupture propagation problems, the thickness of the shear zone band depends highly on the mesh selection and denser mesh is essential in areas where significant changes in stress or strain can be expected during the analysis.

In fact, (Anastasopoulos et al. [2013]) in their 3D free field model exploring the interaction of pile foundation with a rupturing normal fault used elements with $d_{FE} \leq 1m$, while in the vicinity of the structure the maximum element size was 0.3 meters. In addition, (Rasouli and Fatahi [2018]) investigated a cushioned piled raft foundation subjected to normal fault rupture and used elements with $d_{FE} \leq 0.5m$ at the points of interest, while away from the fault the mesh was coarser. For this purpose, the middle part of the model as depicted in Figure 3.10 has a lower coarseness factor compared with the latter boundaries.

This leads to an optimisation problem considering the necessity for a very fine mesh and the available computational resources. Plaxis 3D in large domains, as the one examined in this investigation is very demanding in terms of computational power, especially when the structure is added. Thus, the choice for the mesh density is based on the best possible results considering the available resources.
In Plaxis 3D, the mesh generator requires a global meshing parameter l_e, which represents the target element dimension based on the following equation, including the outer geometry dimensions and the element distribution:

$$l_e = r_e \cdot 0.05 \cdot \sqrt{(x_{max} - x_{min})^2 + (y_{max} - y_{min})^2 + (z_{max} - z_{min})^2} \tag{3.1}$$

The element distribution factor r_e varies from 0.5 for very fine to 2 for very coarse mesh. In this case, very fine mesh is selected. In order to further refine the mesh locally, the coarseness factor is employed. This factor reduces the target element size and is selected as 0.3 in the middle 50 meters of the model and 0.7 on the outer parts. This led to a generation of a mesh for the free field model with with approximately 500,000 soil elements, 700,000 nodes and an average element size of 1.45 meters, while the mean element size in the refined area is 0.53 meters. This mesh is considered as acceptable for the purposes of this analysis. A representative figure of the free field mesh is depicted in Figure 3.12.

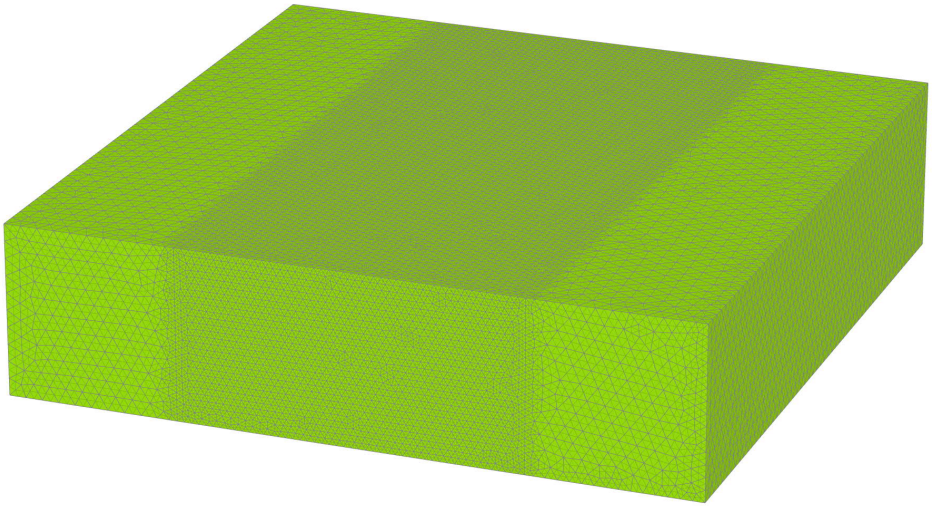

Figure 3.12. Mesh of the 3D free field model.

Plaxis 3D supports staged construction, so the user is able to specify different settings for every phase, apply different calculation methods and activate different objects in the model. For the free field model, the following two phases are activated:

1. **Phase 0 - Initial stress:** This stage is automatically generated and represents the initial stress state by using the K_0 procedure. In this case the lateral earth pressure coefficient at rest for normal consolidation soil is used and calculated as $K_0 = 1 - sin\phi$.

2. **Fault:** In this stage the surfaces are introduced and the prescribed displacement is applied to model the reverse/normal fault.

3.5 Reverse fault

Four different bedrock offsets of reverse fault rupture are modelled, see Table 3.3, and then are compared with the available data in (Anastasopoulos et al. [2007]) as those are presented in Section 3.3. These data include $\Delta_y - d$ plots in order to verify the capability of HSsmall and corresponding modelling technique in Plaxis 3D to capture the soil response. In addition, a further visual comparison is developed against photographs from centrifuge experiments and deformed mesh with superimposed plastic shear strain concentration.

Figure 3.13 illustrates the response for 1.07 meters reverse fault with HSsmall, against the provided displacement profiles at the soil surface from the FEA model with the modified Mohr-Coulomb soil model with 1 meter fault, and the centrifuge experiment producing 1.13 meters fault.

As it is evident, despite the small difference in the imposed displacements, the vertical displacement profile at the surface of the soil volume is identical and the soil behavior is captured perfectly. The maximum vertical displacement reaches 1 meter at $d = 15m$, while from $d = -25m$, five meters away from the centre of the model along the negative x-axis, the soil surface is unaffected from the fault.

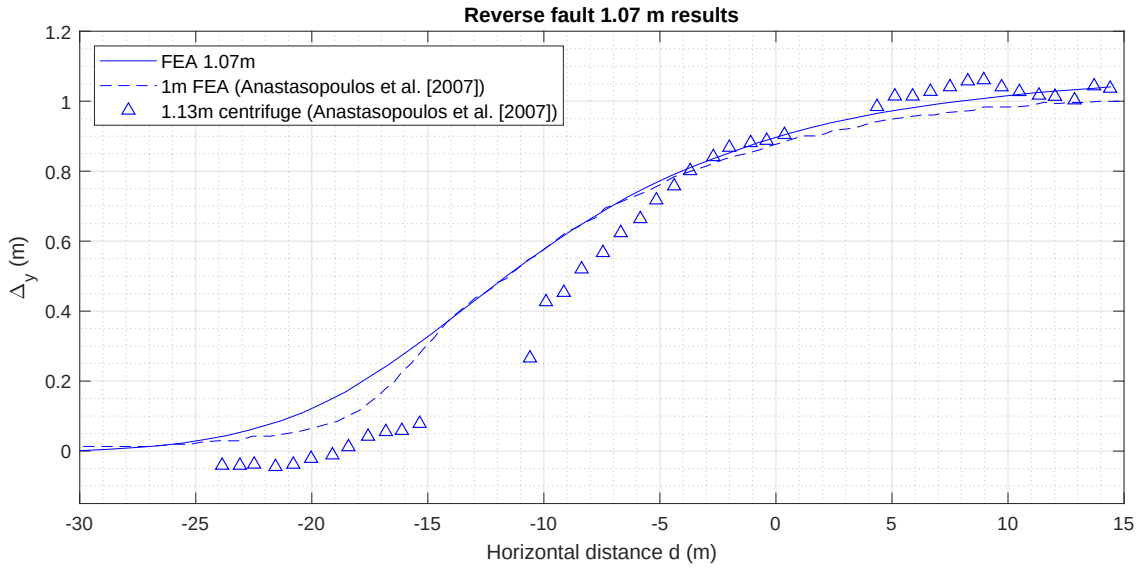

Figure 3.13. $\Delta_y - d$ comparison for reverse fault with 1.07 meters bedrock offset.

In Figures 3.14 and 3.15, the soil volume deformation after the reverse fault rupture is illustrated. Note that the deformed soil volume is scaled up to 5 times for clarity. The same scaling is followed through the report for this type of Figures in order to endure the ability of direct comparisons. Even though an exact comparison cannot be made, the general outcome is that the FEA model deformation is qualitatively relevant with the centrifuge results.

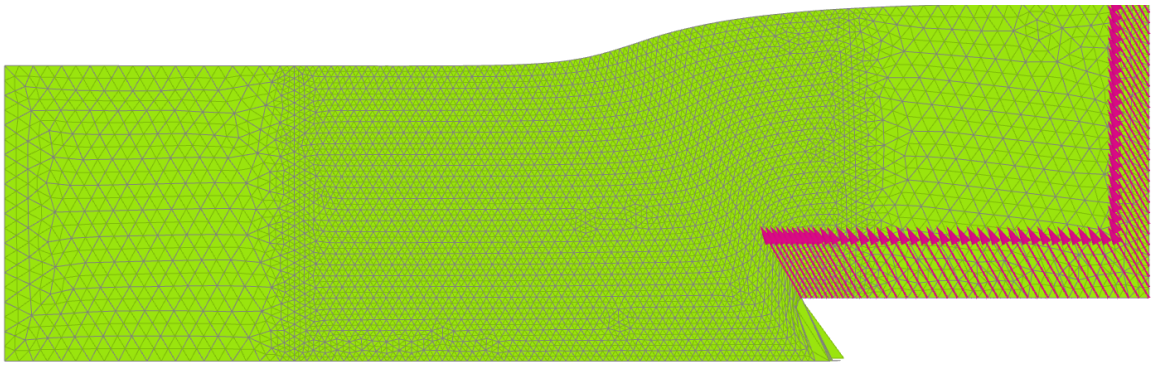

Figure 3.14. Deformed soil volume and mesh after 1.07 meters reverse fault rupture.

Figure 3.15. Provided soil deformation for $h = 1.13m$ reverse fault on centrifuge test with $D_r = 83.9\%$.

Figures 3.16 and 3.17 compare the deformed mesh with plastic shear strain band. Note that only shear strains higher than 0.04 are depicted in order to identify the exact fault rupture propagation. The same approach is followed throughout the report for the free field calculations, unless stated otherwise. The plastic shear strain band for the remaining fault offsets are presented in Appendix B since there are no further available data to compare against in the literature.

It is clear from the figures that the trend of shear strain band is captured, with the higher plastic strains developing close to the position of the applied displacement and then reduce until it outcrops at the soil surface. The only difference between the two models is that on the provided plot, the shear strain band tends to bend in a higher extent towards the footwall, while the calculated results with HSsmall model seems to have a higher angle to the horizontal.

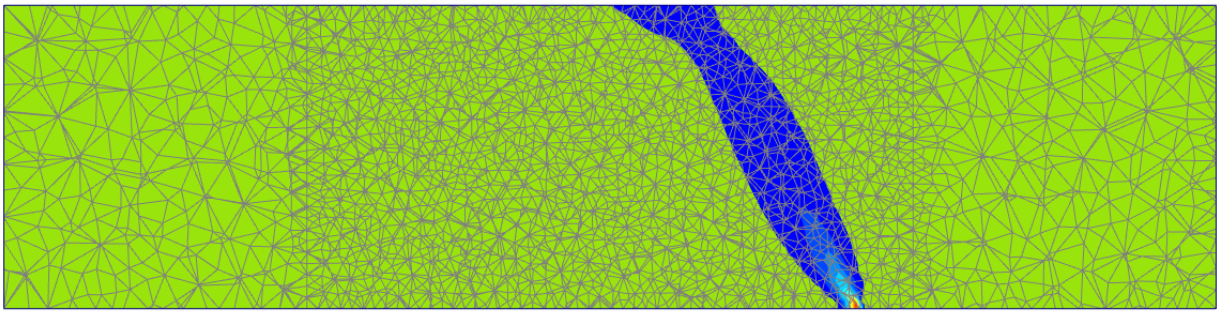

Figure 3.16. FEA plastic shear strain concentration for 1.07 meters reverse fault.

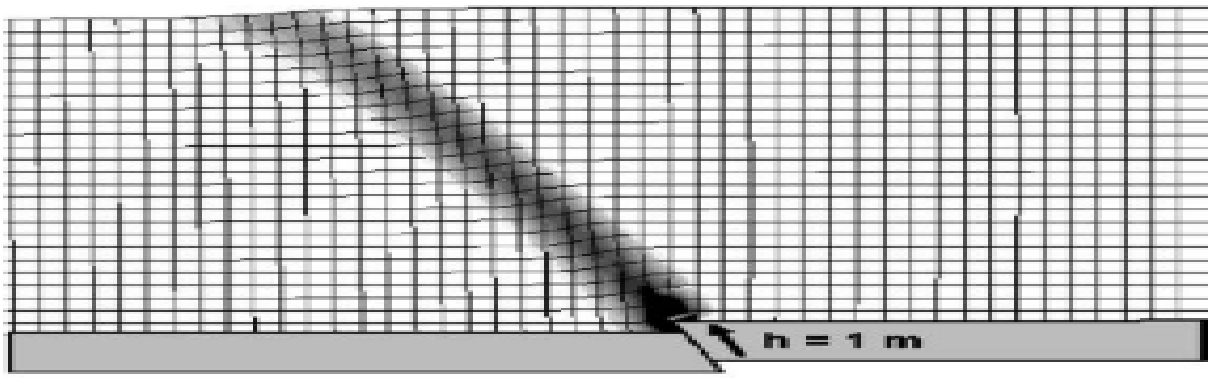

Figure 3.17. Provided FEA plastic shear strain concentration for 1 meter reverse fault, (Anastasopoulos et al. [2007]).

Figure 3.18 illustrates the response for 0.70 meters reverse fault, against the provided displacement profiles from the FEA model with the modified Mohr-Coulomb soil model and the centrifuge experiment, both imposing 0.70 meters of reverse fault. It is clear that in this case also, the vertical displacement profile at the surface of the soil volume is identical and the soil behavior is captured perfectly. The maximum vertical displacement reaches 0.66 meters at $d = 15m$, while from $d = -25m$, five meters away from the centre of the model along the negative x-axis, the soil surface is unaffected from the fault.

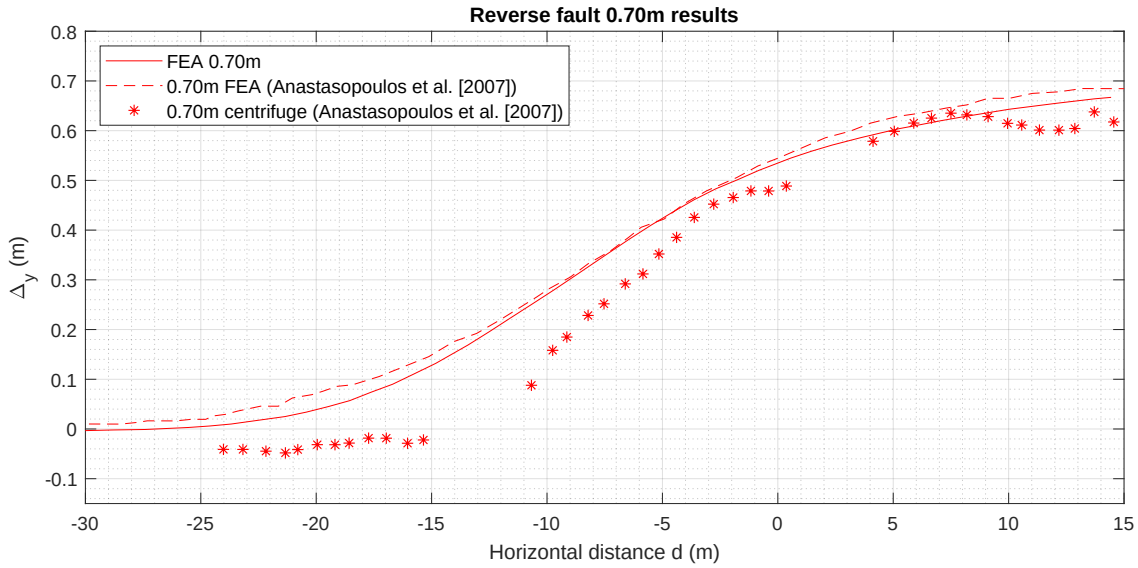

Figure 3.18. $\Delta_y - d$ comparison for reverse fault with 0.70 meters bedrock offset.

Figure 3.19 illustrates the response for 0.50 meters reverse fault against the provided displacement profiles from the FEA model with the modified Mohr-Coulomb soil model and the centrifuge experiment, imposing 0.50 and 0.49 meters of reverse fault, respectively. As in the previous results, the vertical displacement profile at the surface of the soil volume is reproduced in the best possible way. The maximum vertical displacement reaches 0.48 meters at $d = 15m$, while from $d = -22m$, two meters away from the centre of the model along the negative x-axis, the soil surface is unaffected from the fault.

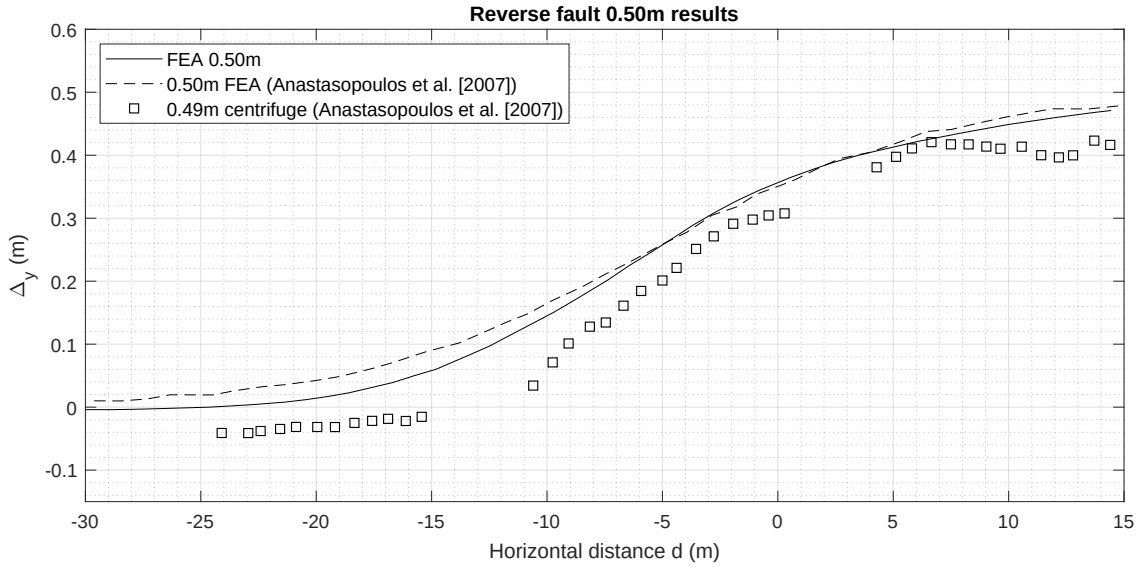

Figure 3.19. $\Delta_y - d$ comparison for reverse fault with 0.50 meters bedrock offset.

Lastly, Figure 3.20 illustrates the response for 0.19 meters of reverse fault against the provided displacement profiles from the FEA model with the modified Mohr-Coulomb soil model and the centrifuge experiment, imposing 0.20 and 0.18 meters of reverse fault, respectively. In this case, it is evident that such small displacements are unable to produce large deformations and affect the soil profile significantly. Although, the vertical displacement profile at the surface of the soil volume is

again identical in all three cases. The maximum vertical displacement reaches 0.17 meters at $d = 15m$, while from $d = -20m$, , at the centre of the model along the negative x-axis, the soil surface is unaffected from the fault.

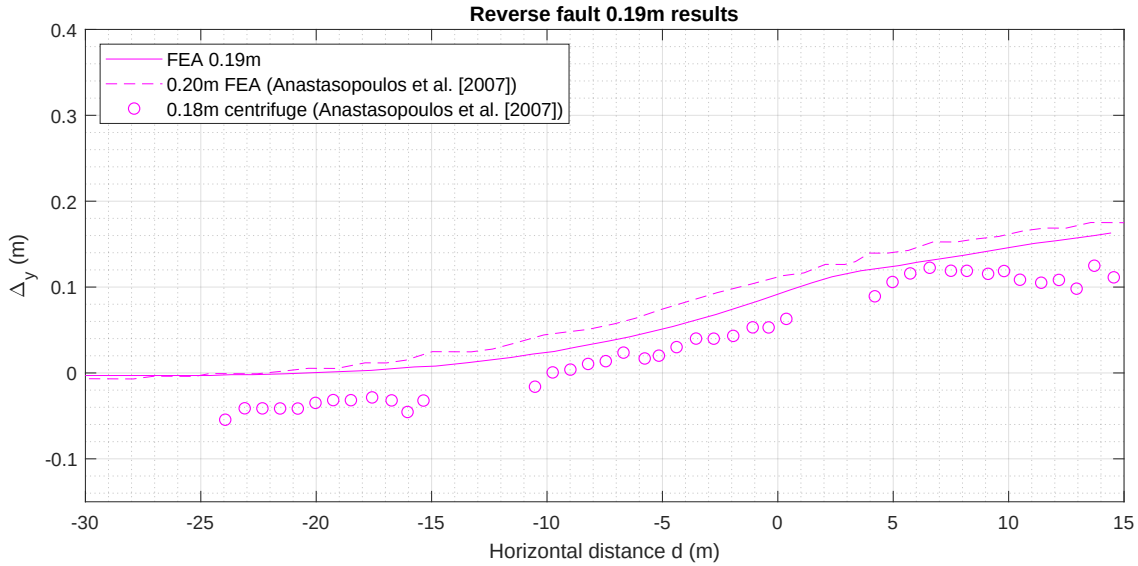

Figure 3.20. $\Delta_y - d$ comparison for reverse fault with 0.19 meters bedrock offset.

Overall, it can be claimed with a high degree of confidence that reverse fault rupture modelling in Plaxis 3D with HSsmall soil model can reproduced realistic results. The outcomes in both term of $\Delta_y - d$ plots and shear strain localisation are identical with the results produced by centrifuge experiments and FEA models, with a modified Mohr-Coulomb version accounting for strain softening. Thus, this type of fault will be used later on on the parametric analysis and is expected to give valid and trustful results.

3.6 Normal fault

Similar to the approach followed in the reverse fault results, in the normal fault calculation four different bedrock offsets are modelled and compared with the available literature data by (Anastasopoulos et al. [2007]). The modelled offsets can be seen in Table 3.3. $\Delta_y - d$ plots are employed for the comparison, along with deformed mesh with superimposed plastic shear strains for a visual comparison.

Figure 3.21 presents the vertical displacement over distance d trend for 1.04 meters of normal fault with HSsmall, against 1 and 1.08 meters fault from FEA analysis with modified Mohr-Coulomb and centrifuge test, respectively. In this case, it is clear that the level of accuracy is not the same as in the reverse fault, see Figure 3.13.

Even though the soil behavior is captured in a qualitatively acceptable manner, leading to the highest settlement of approximately 1 meter, the quantitative agreement is not exact. This might be due to the difference on the relative densities, with the provided data having $D_r = 80\%$, while the HSsmall parameters used are calibrated for $D_r = 75.8\%$. Although this might be one reason for this differences, it cannot be claimed definitive since the reverse fault $\Delta_y - d$ plots have a perfect match despite the density difference. Another reason that might cause such inaccuracies is the interaction of the fault with the boundaries of the model. It seems that the applied surface displacement forces the model to "slide" outside of the boundaries and smoothen the surface displacement profile.

The soil deformation can be split in two different areas in the plot, with the first being from $d = -2.5m$ until $d = 15m$, where the displacement profile is identical , while the second area (from $d = -2.5m$ and along the negative x-axis), the soil behaves slightly different than expected. In fact, initially the modelled soil seems to be stiffer between $d = -2.5m$ and $d = -7.5m$, giving less displacement, while after $d = -7.5m$ the behavior is alternated and while the available data points reach zero vertical displacement the modelled soil is still experiencing vertical displacements. In other words, the calculations from (Anastasopoulos et al. [2007]) resulted in a steeper $\Delta_y - d$ curve.

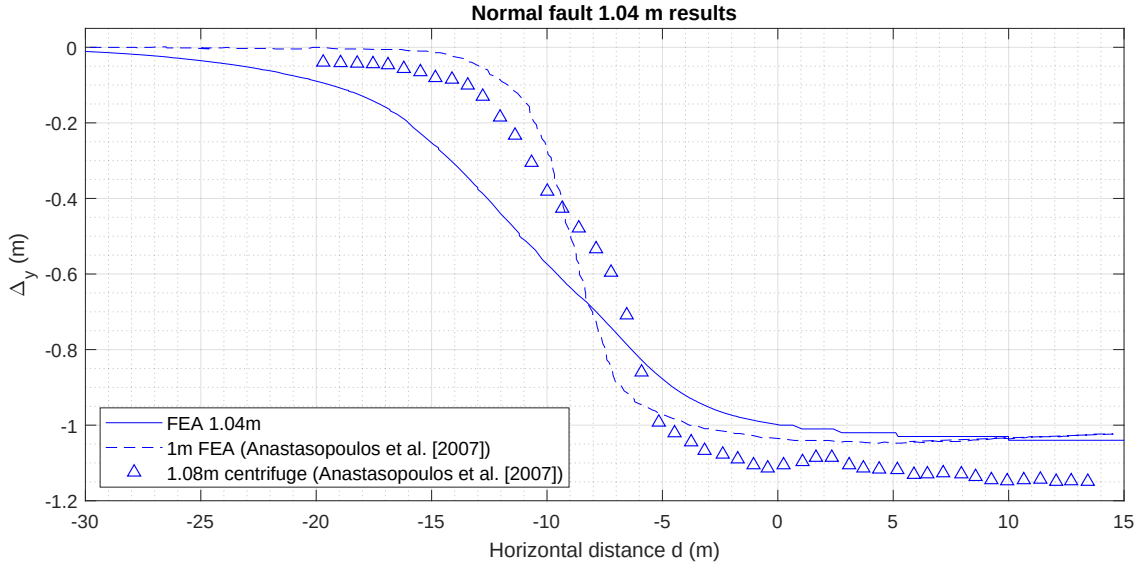

Figure 3.21. $\Delta_y - d$ comparison for normal fault with 1.04 meters bedrock offset.

Figures 3.22 and 3.23 depict the deformed soil volume after the Finite Element Analysis and centrifuge test, respectively. Although is hard to do a direct comparison, it can be claimed that the soil deformation follows at least approximately the same pattern in both cases.

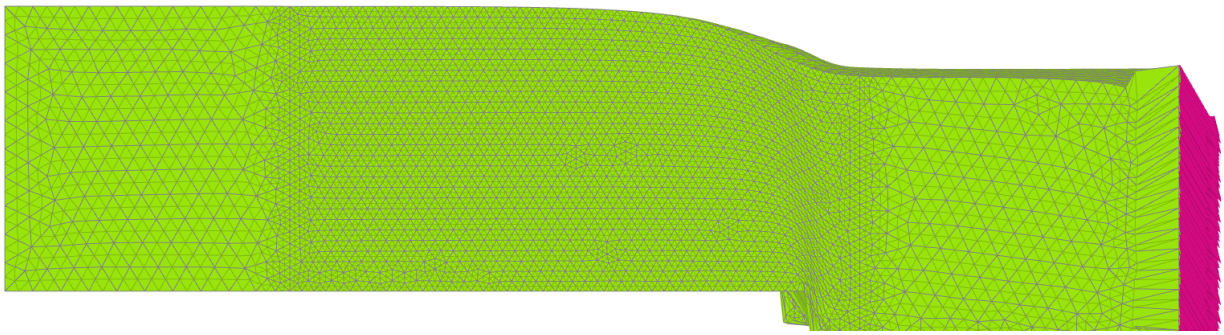

Figure 3.22. Deformed soil volume and mesh after 1.04 meters normal fault rupture.

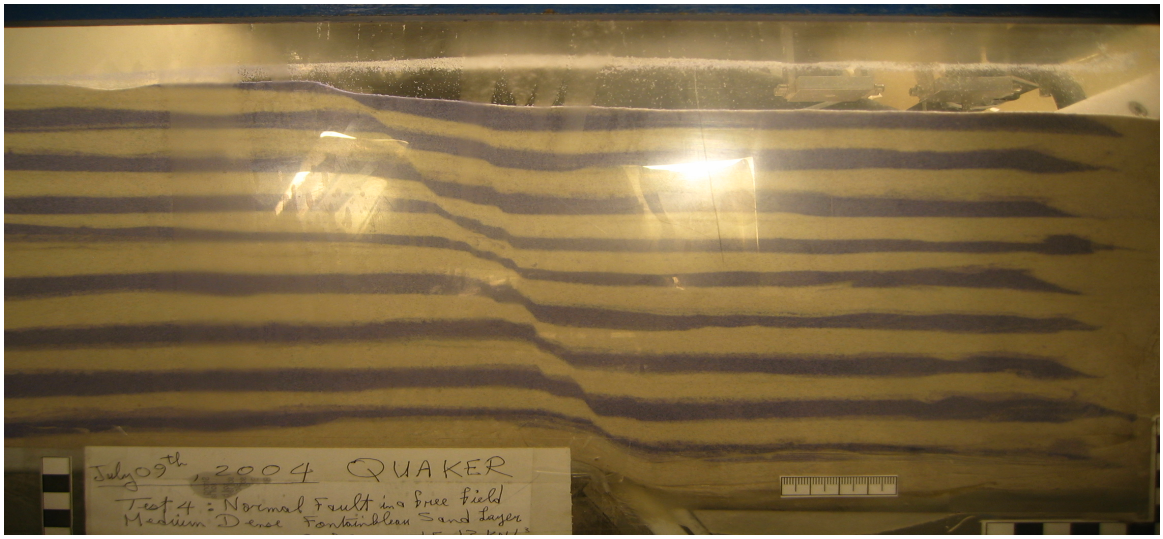

Figure 3.23. Provided soil deformation for $h = 1.08m$ normal fault on centrifuge test with $D_r = 80\%$.

Figures 3.24 and 3.25 are illustrating the deformed mesh with plastic strain concentration for 1.04 and 1 meters normal fault, respectively. The plastic shear strain band for the remaining fault offsets are presented in Appendix B since there are no further available data to compare against.

As in the reverse fault, the same response is experienced herein. The fault path follows the same trend, outcrops in the surface with the only differences being that in the provided figure the shear band bends to the footwall in a higher extent than the calculated one. In addition, the thickness of the band is smaller in the provided data, but this depends highly on the element size. A more narrow shear zone could be achieved with denser mesh, but this was not possible with the available computational resources. Overall, the response is very well captured and the result is considered as acceptable.

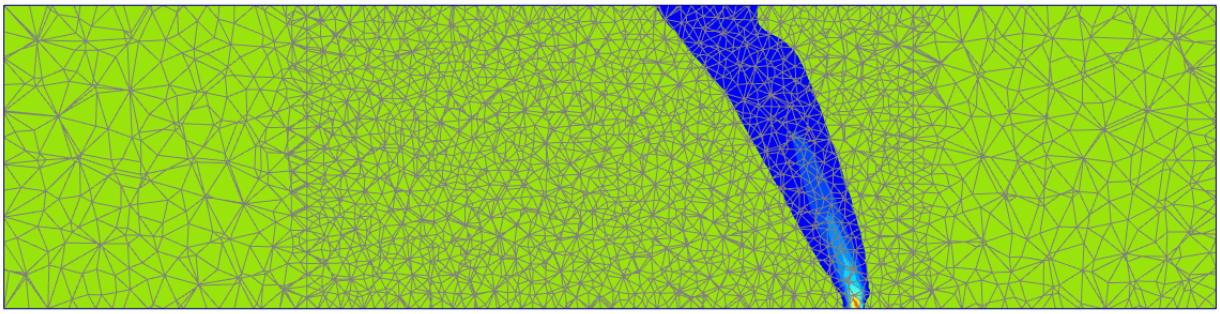

Figure 3.24. FEA plastic shear strain concentration for 1.04 meters reverse fault.

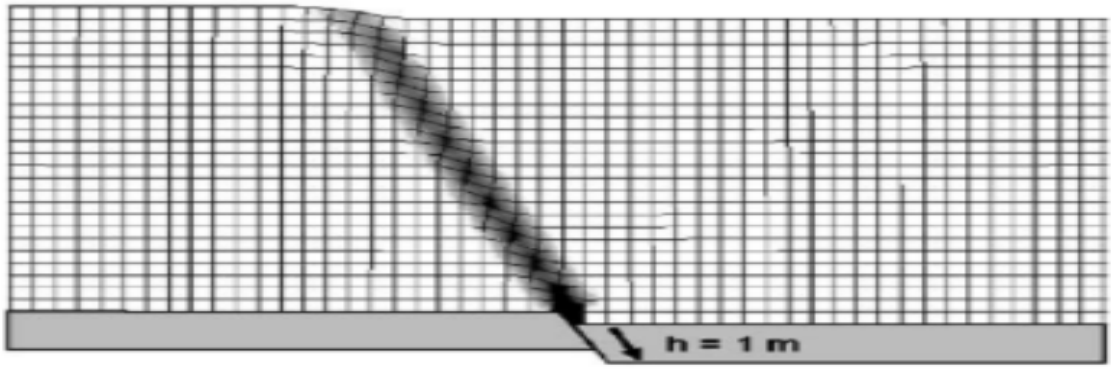

Figure 3.25. Provided FEA plastic shear strain concentration for 1 meter normal fault.

Figure 3.26 presents the vertical displacement versus distance for the 0.825 meters normal fault with HSsmall, against the provided 0.80 and 0.85 meters faults from Finite Element Analysis and centrifuge test, respectively. In this case, the three analysis follow the same trend until $d = -7.5m$, while after that and along the negative x-axis the calculated displacements are higher than the provided ones, until it converge again at $d = -30m$. Overall, the result is considered as acceptable for the purposes of this investigation.

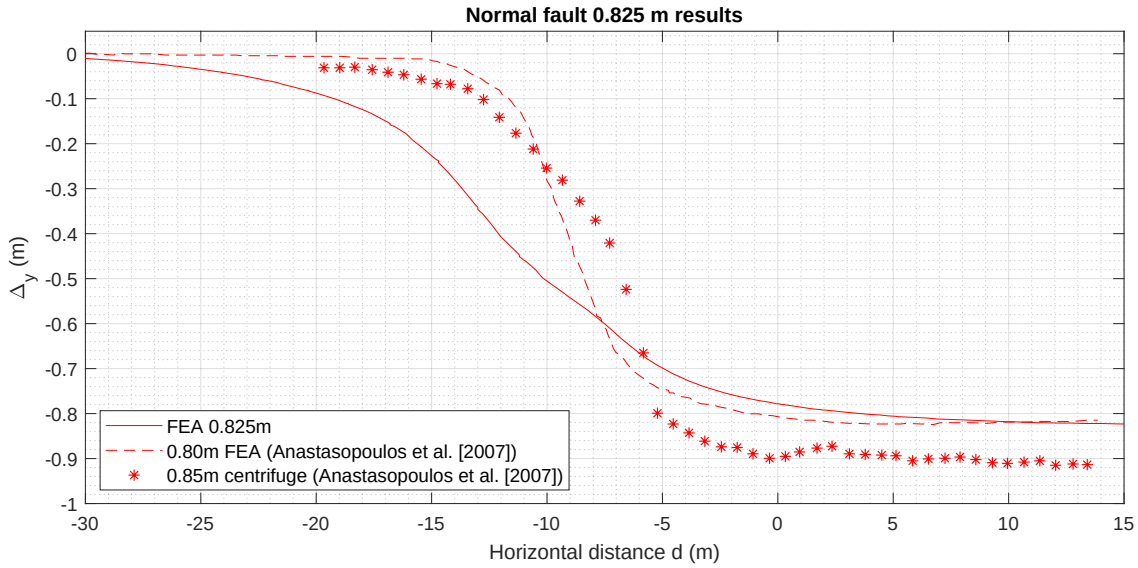

Figure 3.26. $\Delta_y - d$ comparison for normal fault with 0.82 meters bedrock offset.

Figure 3.27 presents the vertical displacement versus distance for the 0.50 meters normal fault, against the provided faults from Finite Element Analysis and centrifuge test, using the same bedrock offset. Similarly to the previous findings, the three analysis follow the same trend until $d = -7.5m$, while after that along the negative x-axis the calculated displacements are higher than the provided ones until it converge again at $d = -30m$, away from the location of the applied fault. Overall, this result is also considered as acceptable for the purposes of this investigation.

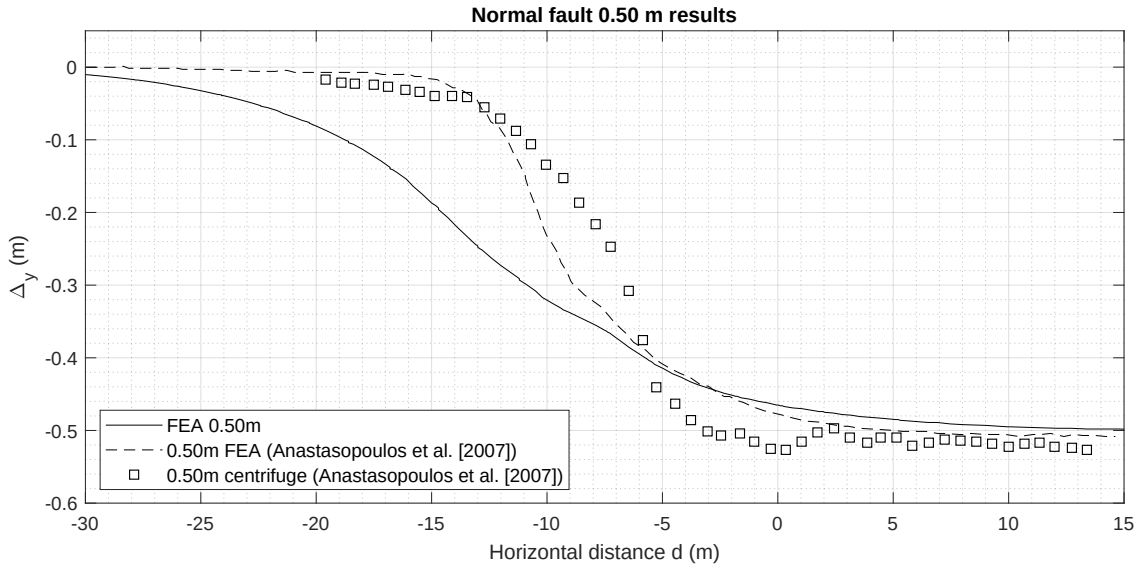

Figure 3.27. $\Delta_y - d$ comparison for normal fault with 0.50 meters bedrock offset.

Lastly, Figure 3.28 presents the vertical displacement versus distance for the 0.225 meters normal fault, against the provided faults from Finite Element Analysis and centrifuge test, using 0.20 and 0.25 meters dislocations, respectively. Despite the minor value of offset, in this case the displacement curve is identical until $d = -5m$, while after that along the negative x-axis the calculated displacements are higher than the provided ones, until it converge again at $d = -27.5m$ away from the location of the applied fault.

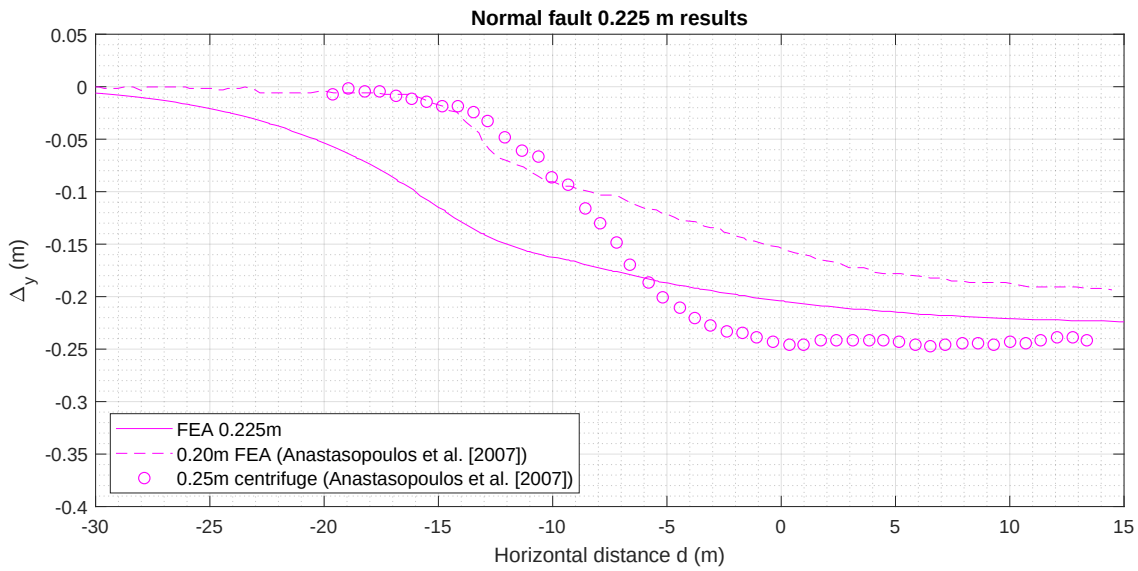

Figure 3.28. $\Delta_y - d$ comparison for normal fault with 0.225 meters bedrock offset.

With the soil model and modelling technique verified, four further bedrock offsets are calculated for use in the parametric study. Although, only one of these is finally used due to time limitations and the rest are presented in Appendix B as a benchmark for further studies.

Parametric Study 4

In this chapter, the parametric study is presented. The tripod suction bucket structure is modelled and the response of it under reverse fault rupture is investigated. The structure is placed in three different positions with respect to the free field outcrop location, so the rupture emerges under every bucket subsequently with the L/D ratio being equal to 1. Afterwards, the same analysis is performed with L/D ratio equal to 0.5 to see the influence of the skirt length on the structural rotations, settlements and plastic shear strain localisation.

4.1 Numerical Model

The numerical model as described in Subsection 3.4 for the free field response is used in the parametric study by adding the suction bucket tripod foundation.

A plan view of the suction bucket tripod is depicted in Figure 4.1. The length over diameter ratio is equal to 1 in the first calculation subset and equal to 0.5 in the second calculation subset, with the diameter being 6.5 meters in both, while the skirt length is 6.5 and 3.25 meters, respectively. The distance between the bucket geometrical centre and the reference point, where the load is applied is equal to 19.5 meters, leading to an S/D spacing ratio equal to 3.

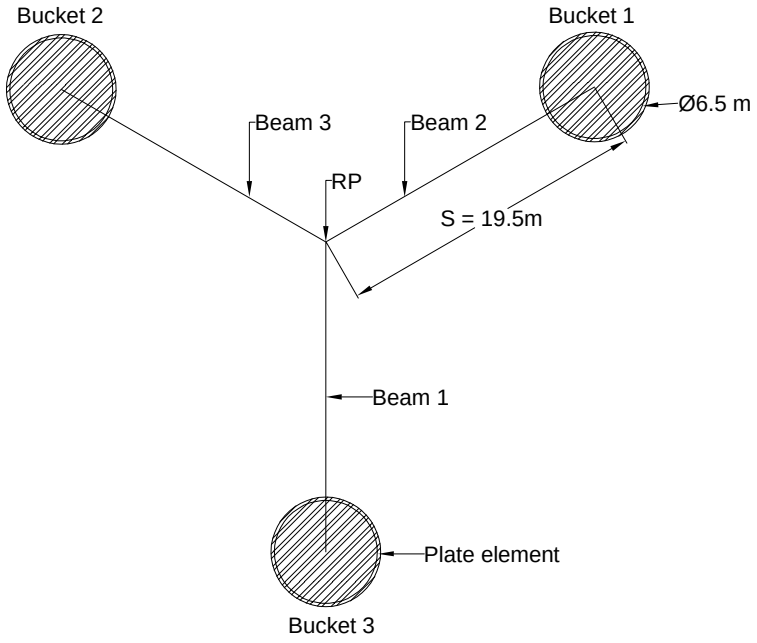

Figure 4.1. 2D plan view of the tripod suction bucket.

The suction bucket lid and skirt are modelled with elastic plate elements accounting for high strength steel and reproducing a very rigid structure which allows rigid body rotation and prevents any deformation on the steel components, since those deformations -if any- are outside of the scope of this research. The plates are composed by 6-node triangular elements with three rotational and three translational degrees of freedom per node. The steel parameters are illustrated in Table 4.1.

Parameter	Value	Units
Thickness	0.2	m
Unit Weight	77.0	kN/m^3
Elastic Modulus	18.0 E9	kN/m^2
Shear Modulus	7.5 E9	kN/m^2
Poisson's Ratio	0.2	[-]

Table 4.1. Material parameters for bucket steel.

The buckets are connected with elastic beam elements, which are composed by 3-node line elements with three rotational and three translational degrees of freedom per node. These beams are connected in a height $z = 5m$, where the point load accounting for the wind turbine superstructure is applied. The beam material parameters are illustrated in Table 4.2.

Parameter	Value	Units
Elastic Modulus	18.0 E6	kN/m^2
Unit Weight	77.0	kN/m^3
Cross Section Area	1.0	m^2
Moment of Inertia	34.0 E6	m^4

Table 4.2. Material parameters for connection beams.

In order to precisely model Soil-Structure Interaction, interfaces are added to the plate elements, consisting of 12-node interface elements compatible with the 6-noded triangular side of a soil or plate element. The roughness of the interaction is modelled by choosing a suitable value for the strength reduction factor R_{inter}. The strength reduction factor is defined as $R_{int} = (tan\delta/tan\phi$, where δ is the friction angle between soil and skirt and ϕ is the internal friction angle of the soil. The value of R_{inter} is chosen as 0.48, following a calibration campaign conducted by (K. Glitrup and L.R. Christiansen [2019]).

Additionally, extended surfaces equal to $0.2D$ are modelled at the skirt tip, since at positions where high peaks in stress and strains are expected, non-physical stress oscillations may be experienced. In this condition, a soil material is assigned in the extended interface corresponding to the adjacent soil without any reduction in interface strength.

The vertical load applied on the tripod is equivalent to $V = 0.5V_{peak}$. The maximum vertical compression capacity V_{peak} is calculated by (K. Nielsen [2020]) as 69.4 MN, for $S/D = 3.0$ and $L/D = 1.0$. The same load is applied throughout the parametric study for both skirt lengths to avoid any conflicts between the analysis and reduce the uncertainties. The coarseness factor applied to the plate and beam material is equal to 0.1, leading to a final mesh consisting of approximately 550,000 elements with 800,000 nodes.

Figure 4.2 is a representative case for the suction bucket tripod model, along with the connection beams, the applied load and the interfaces. The two vertical surfaces enclose the mesh refinement area, while the applied surface displacement for reverse fault can also be seen. Note that the mesh refinement area is moved accordingly with the structure to secure that the points of interest are always

enclosed. Figure 4.3 presents a representative case for the completed model with the soil volume, the structure and the generated mesh.

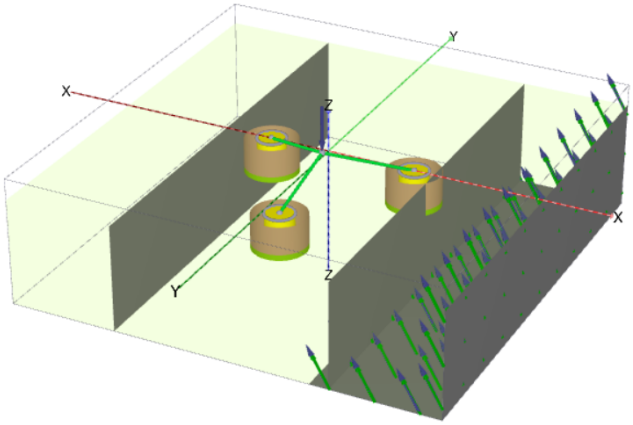

Figure 4.2. Suction bucket tripod model.

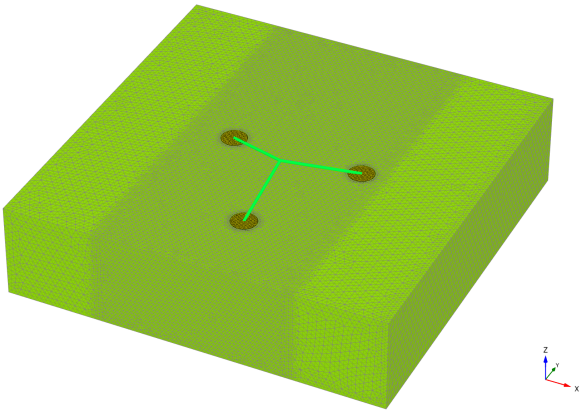

Figure 4.3. Complete model with generated mesh.

The phases for the staged construction are:

- **Phase 0 - Initial stress:** This stage is automatically generated and represents the initial stress state by using the K_0 procedure. The lateral earth pressure coefficient at rest for normal consolidation soil is used and calculated as $K_0 = 1 - sin\phi$.
- **Installation:** In this stage, the structure is installed. Note that after the completion of the installation all displacements are restored to zero values.
- **Loading:** In this stage the point load is applied at the reference point. As in the previous case, the displacements are restored to zero.
- **Fault:** In this stage the prescribed displacement is applied to model the reverse/normal fault.

4.1.1 Resulting forces in beams and plates

The fault rupture is imposing forces to the tripod and these forces are later in the report described and discussed. Thus, the sign convention needs to be explained in advance. It needs to be noted from the beginning that positive axial forces refer to tension whereas negative forces refer to compression. The sign of bending moments and shear forces depend on the local system axis.

The structure is modelled with beams and plates. Regarding the beams, the axial force N is the force in the first direction while the shear forces Q_{12} and Q_{13} are the shear forces over the second beam axis and the third beam axis, respectively. The bending moment M_1 is the torsion (bending around the first axis), the bending moment M_2 is the bending moment due to bending around the second axis and the bending moment M_3 is the bending moment due to bending around the third axis. Figures 4.4 and 4.5 represent the local axes, the forces and moments acting on the beams.

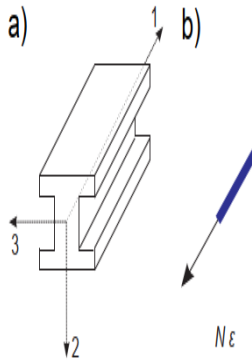

Figure 4.4. Positive axial and shear forces in horizontal beams, (Plaxis [2020*a*]).

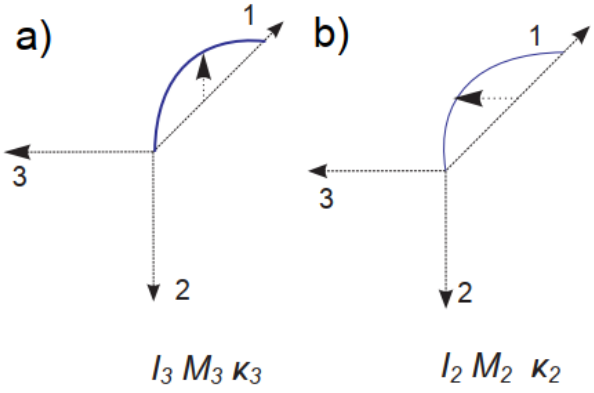

Figure 4.5. Positive bending moments in beams, (Plaxis [2020*a*]).

For plate elements, the axial forces N_1 and N_2 are the axial force in the first and second direction, respectively, the shear force Q_{12} is the in-plane shear force and Q_{13}, Q_{23} are the shear forces perpendicular to the plate over the first and second direction. The bending moment M_{11} is due to bending over the second axis, M_{22} the bending over the first axis and M_{12} is the moment according to transverse shear forces. Figure 4.6 depicts the direction and orientation of the forces acting in plates.

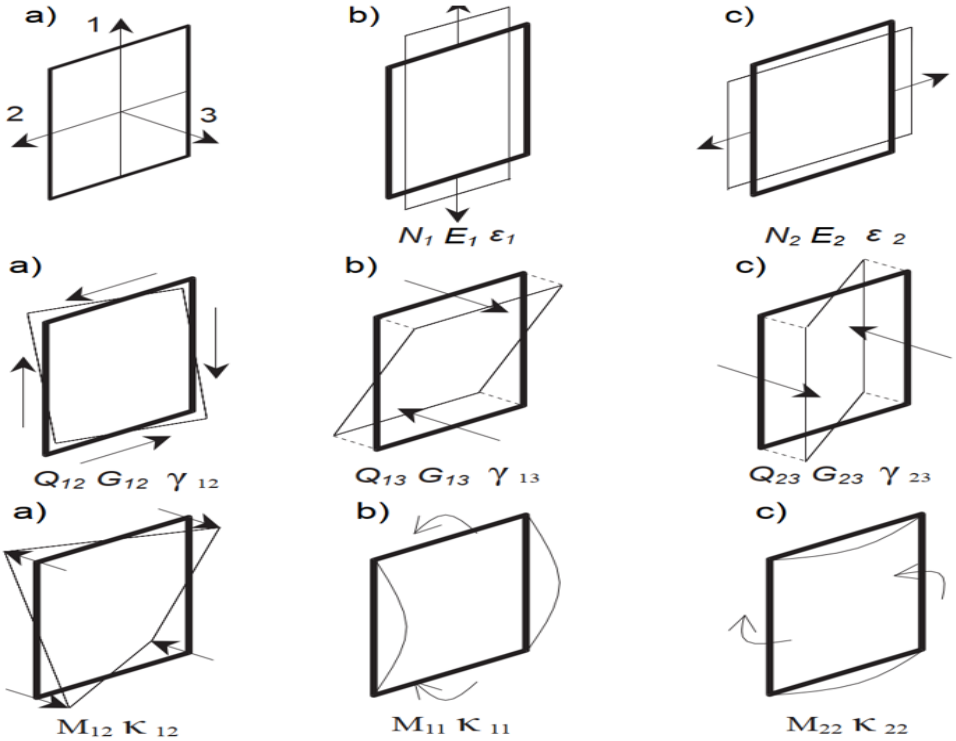

Figure 4.6. Positive axial, shear forces and bending moment directions in plates, (Plaxis [2020*a*]).

4.2 L/D=1

The initial analysis is conducted with length and diameter equal to 6.5 meters while the vertical load accounting for the dead loads acting on the foundation is 34.7 MN. The fault rupture is reverse having 1.5 meters bedrock offset and the tripod position is varied so the fault outcrops under each bucket

subsequently.

The fault rupture path for free field 1.5 meters reverse fault is depicted in Figure 4.7. Note that only shear strains higher than 0.07 are presented for clarity and same scaling is employed for the rest of the report, unless stated otherwise. It is seen that the fault emerges at the surface at a location $x_{outcrop} = 3.5m$ since it is bending towards the footwall. The plan view of the model with plastic shear strain concentration is depicted in Figure 4.8

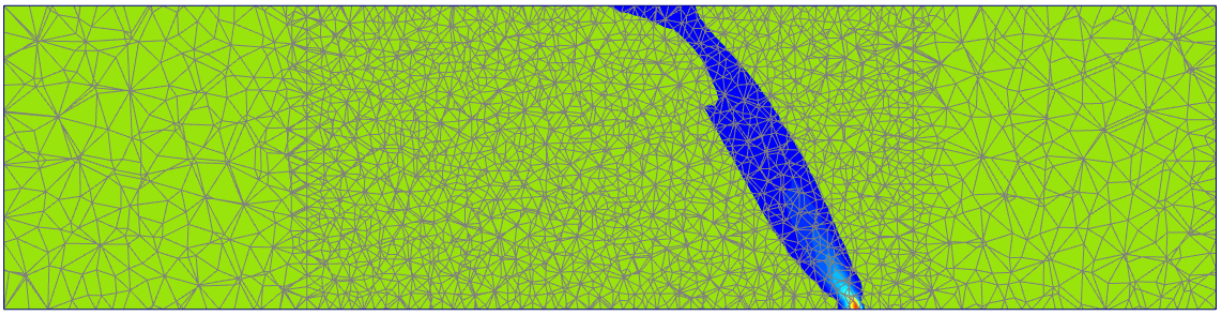

Figure 4.7. FEA plastic shear strain concentration for 1.50 meters reverse fault.

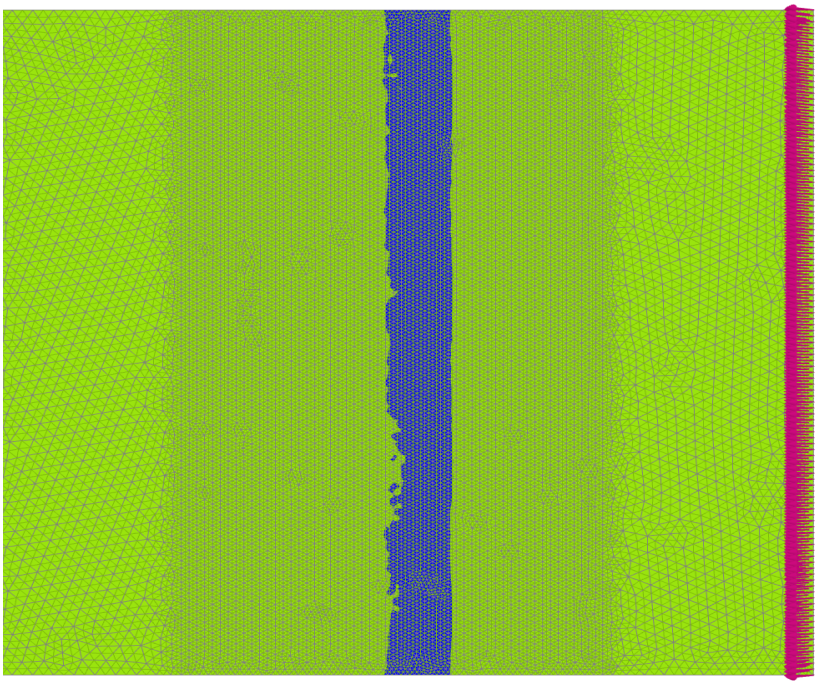

Figure 4.8. Plan view of the free field shear strain contours path.

The deformed soil volume, scaled 5 times for clarity is depicted in Figure 4.9.

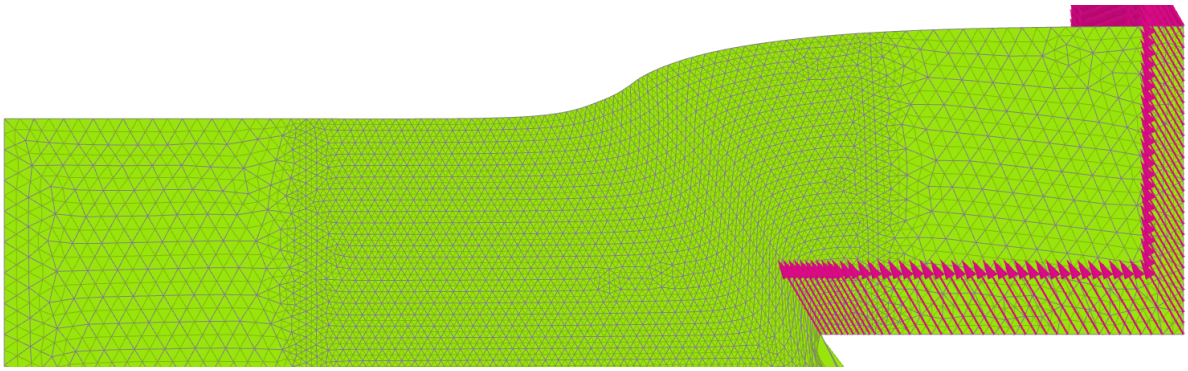

Figure 4.9. Deformed soil volume and mesh after 1.50 meters normal fault rupture.

Since the exact fault outcrop location cannot be known in advance and the response is sensitive to the position of the foundation relative to the free field rupture, the position of the foundation is varied parametrically to explore different interaction mechanisms. Hence, the tripod suction bucket model is placed in three different positions with respect to where the fault rupture would have outcropped in the absence of the bucket group, which is at $x_{outcrop} = 3.5m$. Based on that, every bucket is placed at $x_{outcrop} = 3.5m$ and is expected for the rupture to emerge below its centre. In the first case, named Case A, the free field fault would emerge under bucket number 1, see Figure 4.1, in Case B under bucket 3 and lastly, in Case C under bucket 2.

4.2.1 Case A

Figure 4.10 presents the deformed tripod suction bucket foundation for 1.5 meters reverse fault rupture and the tripod placed so the fault would emerge under bucket 1. As it is depicted, there is no visible significant rotation or structural distress due to fault rupture-suction bucket interaction and the structure seems to remain unaffected from the fault.

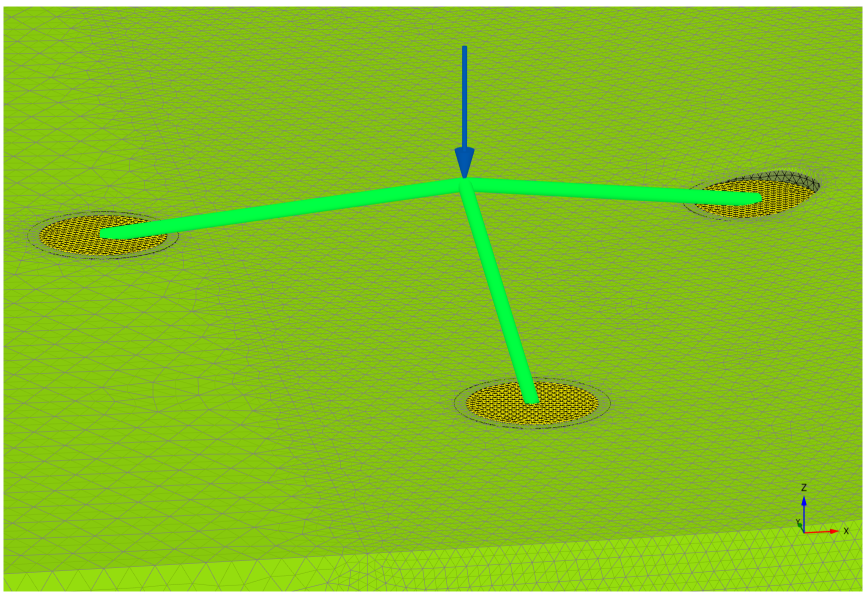

Figure 4.10. tripod deformation in true scale under reverse fault rupture for Case A and $L/D = 1$.

Figure 4.11 illustrates the shear strain contours along the fault rupture path for the free field and for the presence of the structure. It is visible that even the shear strain band should emerge below bucket 1 as indicated by the white dashed line, the FR-SFSI intersperses the fault rupture. In fact, the rupture path is deviated from the presence of the bucket and bends towards the hanging wall. Hence, the bucket acted as a kinematic constraint, causing complete diversion of the fault rupture path and forced it to develop outside the foundation margins.

Regarding the middle leg, namely bucket 3, it can be stated that the rupture propagation is similar to the free field, with the only difference being a slightly higher amount of strains until a depth of approximately 8 meters and a bending towards the footwall. This difference, -even though is minimum- might emanates from the fact that there is a shear strain increment due to the interaction between bucket 1 and the fault. Lastly, bucket 2 is unaltered by the fault.

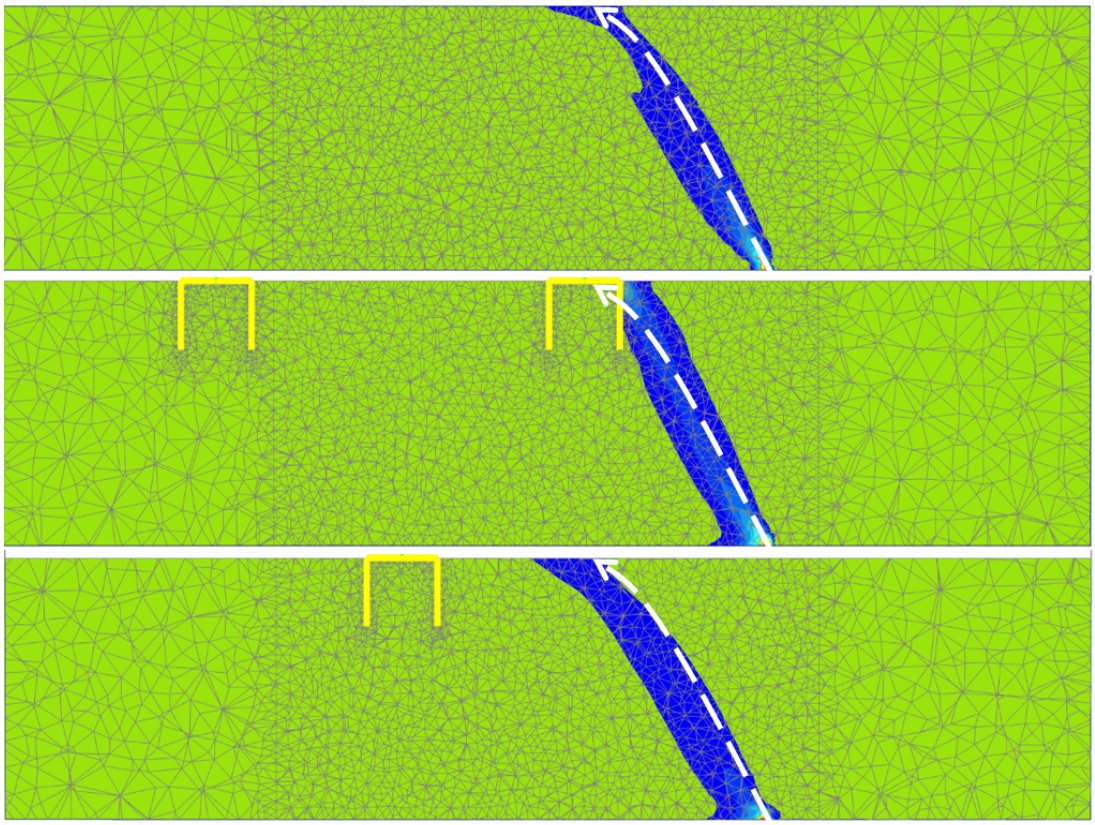

Figure 4.11. Comparison of plastic shear strain contours for Case A and $L/D = 1$. White dashed line indicates the free field path.

Figure 4.12 confirms the above mentioned observations.The plan view reveals that the rupture path is alternated when it reaches bucket 1, while there is increased shear strain localisation on the right edge of the skirt. The left edge does not experience any additional plastic shear strain concentration from the reverse fault.

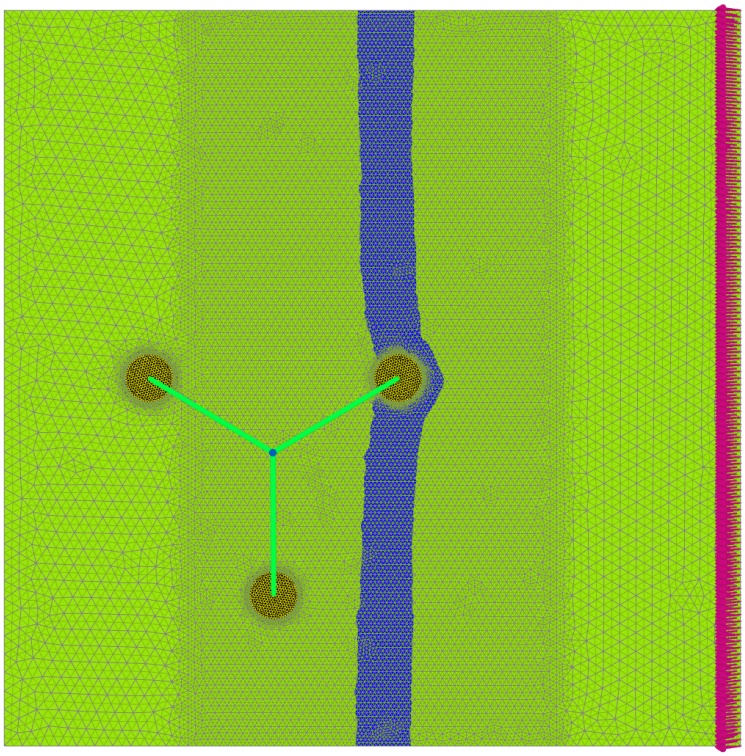

Figure 4.12. Plan view of the shear strain contours path, Case A.

As it is mentioned above, the fault rupture strikes on the side of the bucket skirt and thus is important to investigate the structural response of the system. Note that the tripod is modelled as very stiff, rigid body behavior is expected and structural deformations cannot occur.

Figure 4.13 presents the soil settlement for the tripod buckets. In this case, it is evident that there are no significant settlements in any of the bucket legs. A closer look at the results reveals the mechanism; Bucket one is displaced upwards and the rigid beam connection between them is forcing the rest to settle. Although, it needs to be said clearly that these settlements compared to the structural dimensions can be considered infinitesimally small.

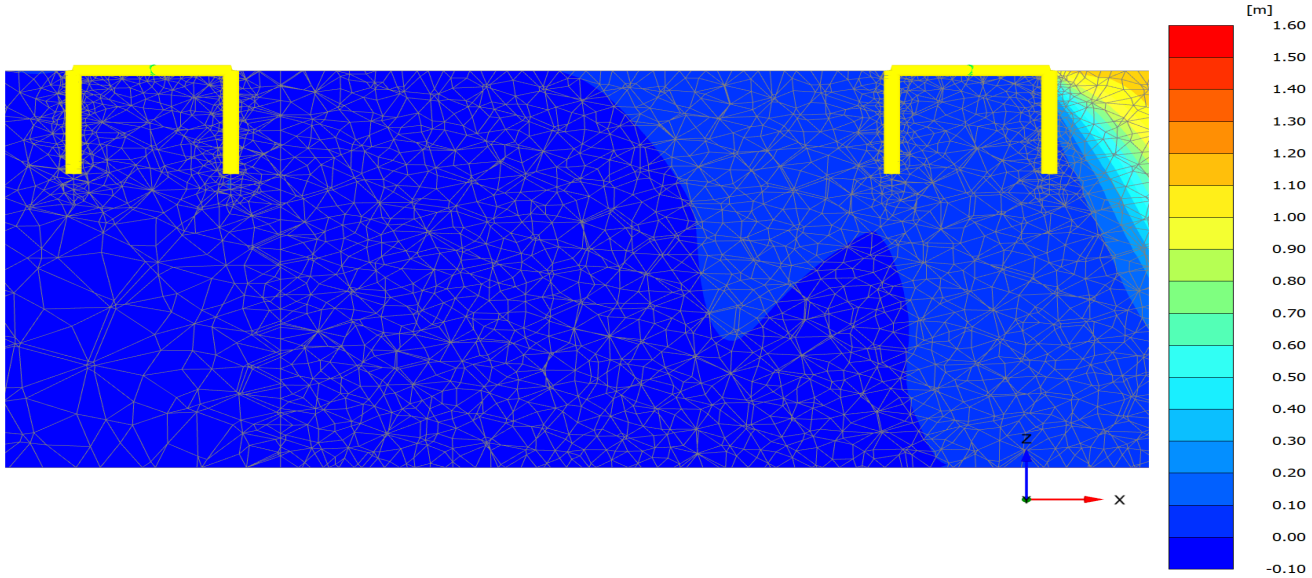

a) Buckets 1 and 2.

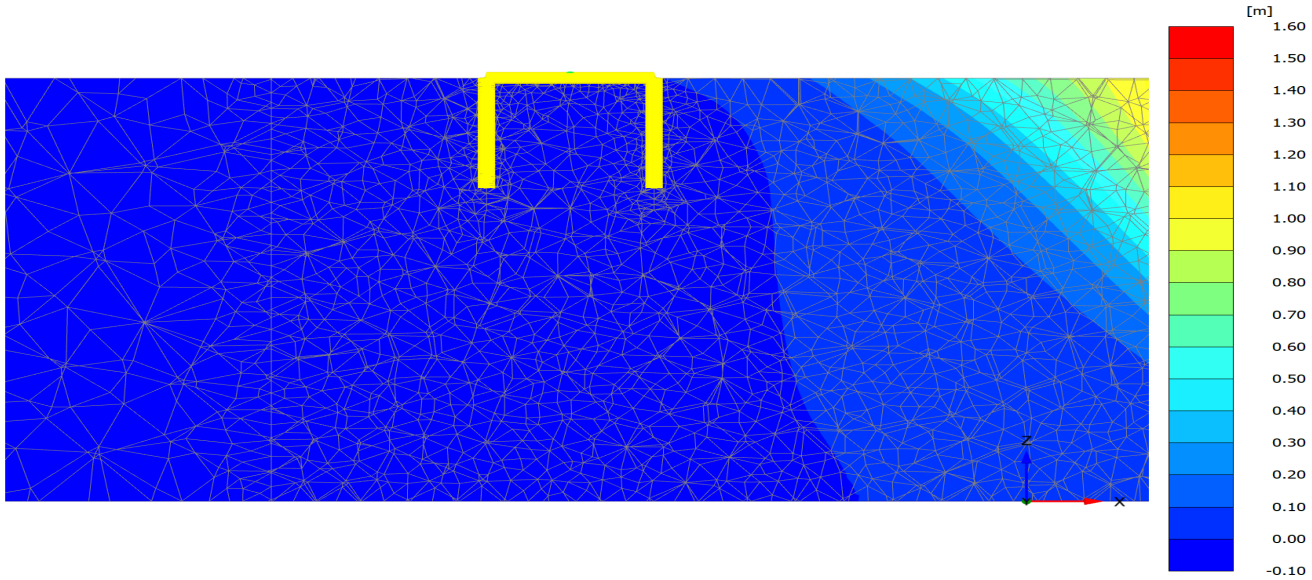

b) Bucket 3

Figure 4.13. Settlement profile, Case A for $L/D = 1$.

Based on the FR-SFSI mechanism, there are horizontal displacements expected on the tripod. The maximum and minimum nodal horizontal displacements along the negative x-axis are presented in Table 4.3.

Bucket	u_{xmin}[cm]	u_{xmax}[cm]
1	-15	-16
2	-9	-11
3	-9	-10

Table 4.3. Tripod horizontal displacements for Case A and $L/D = 1$.

The horizontal displacement of bucket 1 is appeared to be the highest approaching 16 centimeters, while buckets 2 and 3 have maximum displacements in absolute terms equal to 11 and 10 centimeters, respectively. The small difference between the maximum and minimum horizontal displacements is an indication of the rotation of the tripod.

A visualization of the displaced buckets is presented in Figure 4.14 . Note that the displacements are scaled up to five times for clarity. The same scaling applies to all the cases herein, unless stated otherwise. The displaced buckets confirm the above mentioned observations since the dislocations are relatively small despite the scaling, and no noticeable rotations are evident.

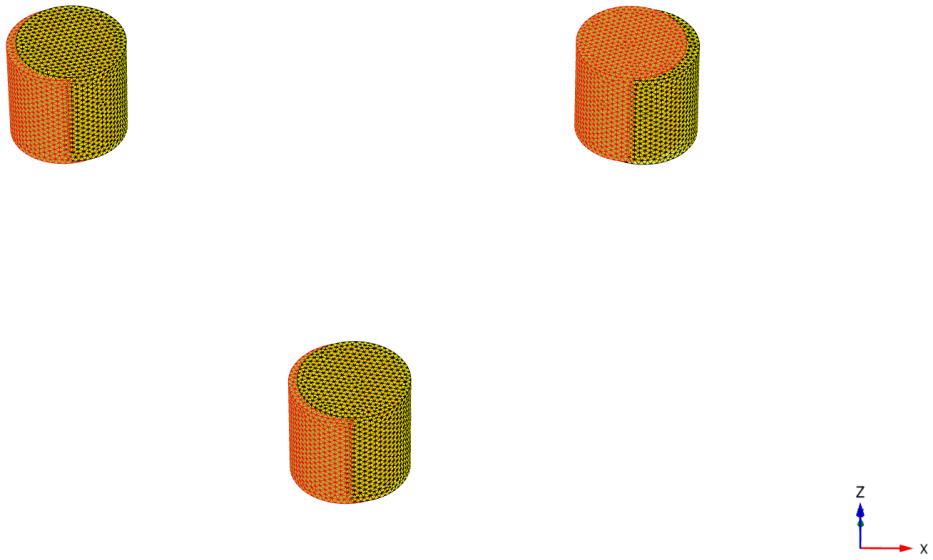

Figure 4.14. Deformed (red) versus stationary (yellow) tripod after fault rupture for Case A and $L/D = 1$.

Lastly, the maximum and minimum nodal forces acting on the bucket are discussed. Table 4.4 presents the axial and shear forces acting on the structure. The moment load is also included. It needs to be noted that those values are not necessarily totally representative of the reality, since the structure modelling is not detailed and is outside of the scope of this thesis.

In addition, these forces refer to the maximum and minimum in the tripod without specifying where they act. They represent the worst case scenario that needs to be taken into account during the design. Despite the uncertainties, with these forces it is allowed to perform a direct comparison between each case and L/D ratio to find the worst case, investigate and open the field for further studies.

Force	Units	Max	Min
N_1	MN/m	22.86	-29.99
N_2	MN/m	11.76	-10.86
Q_{12}	MN/m	13.27	-10.98
Q_{13}	MN/m	656.9	-623.2
Q_{23}	MN/m	197.6	-248.2
M_{11}	MNm/m	82.26	-70.35
M_{12}	MNm/m	27.95	-33.36
M_{22}	MNm/m	18.40	-33.94

Table 4.4. Maximum and minimum forces acting on the buckets for Case A and $L/D = 1$.

It is evident that the tripod suction bucket need to withstand extensive loads due to the fault rupture. The highest are the axial force in the first direction N_1, the shear force perpendicular to the bucket over the first direction Q_{13}, and the bending moment due to bending around the second axis M_{11}. The loads acting on the connection beams are displayed in Table 4.5. It is seen that the forces acting on the beams are lower than the ones acting on the tripod indicating that it absorbs most of the forces, while the axial loads are compressive.

Force	Units	Max	Min
N	MN/m	-3.50	-14.93
Q_{12}	MN	5.13	-6.76
Q_{13}	MN	-7.98	-12.54
M_1	MNm	16.76	29.16
M_2	MNm	50.54	-236.8
M_3	MNm	144.7	-107.6

Table 4.5. Maximum and minimum forces acting on the beams for Case A.

The mechanism for reverse fault rupture-tripod suction bucket foundation for this Case A and $L/D = 1$ can be summarized as:

1. All three buckets remain on the footwall.

2. The fault rupture path is alternated against the one with the absence of the structure and emerges outside of bucket 1 margins, on the right side of the skirt.

3. The tripod is displaced along the negative x-axis. The amount of this displacement is small, while the rotations are close to zero. No damaging settlements are noted.

4. High loads are acting on both the buckets and the connection beams due to the fault rupture.

4.2.2 Case B

Figure 4.15 illustrates the deformed tripod with 1.5 meters reverse fault rupture with the tripod placed in a way that the free field rupture would outcrop under bucket 3. It can be seen that the entire structure rotates due to the fault, with buckets 1 and 3 being carried away by the hanging wall and bucket 2 remaining in the stationary footwall.

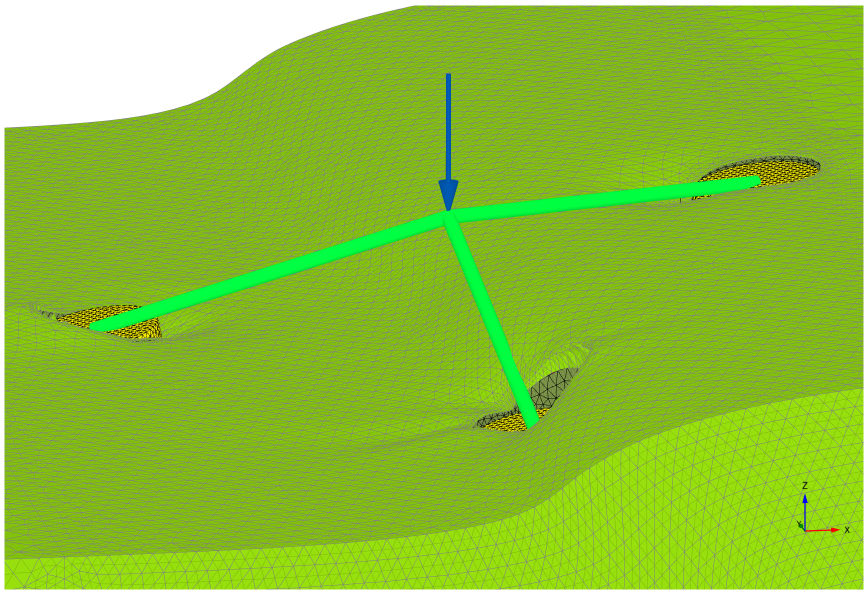

Figure 4.15. tripod deformation in true scale under reverse fault rupture for Case B and $L/D = 1$.

Figure 4.16 depicts the plastic shear strain contours propagating from the fault location to the surface. In this case the fault should have emerged under bucket 3. Although, it is evident as the fault propagates affects all three buckets of the tripod. In fact, bucket 1 is absorbing an amount of the shear strain band on the tips and in the vicinity the left skirt, while bucket 2 also experiences plastic shear strains on both skirts and tips. Based on that it can be stated that the presence of the bucket is affecting the fault rupture propagation and diverts the path.Besides that, the presence of buckets 1 and 2 is not enough to divert completely the path since it stills outcrops on the surface at a position relevant to the free field, with the only difference being a slight bending towards the footwall. at the same location as in the free field.

Regarding bucket 3, where the fault would outcrop without the presence of the tripod the response is similar to Case A with the rupture path being alternated causing the shear strain contours to divert and strike on the outer right part of the skirt, while a small amount is propagating all the way to the top left corner of the lid.

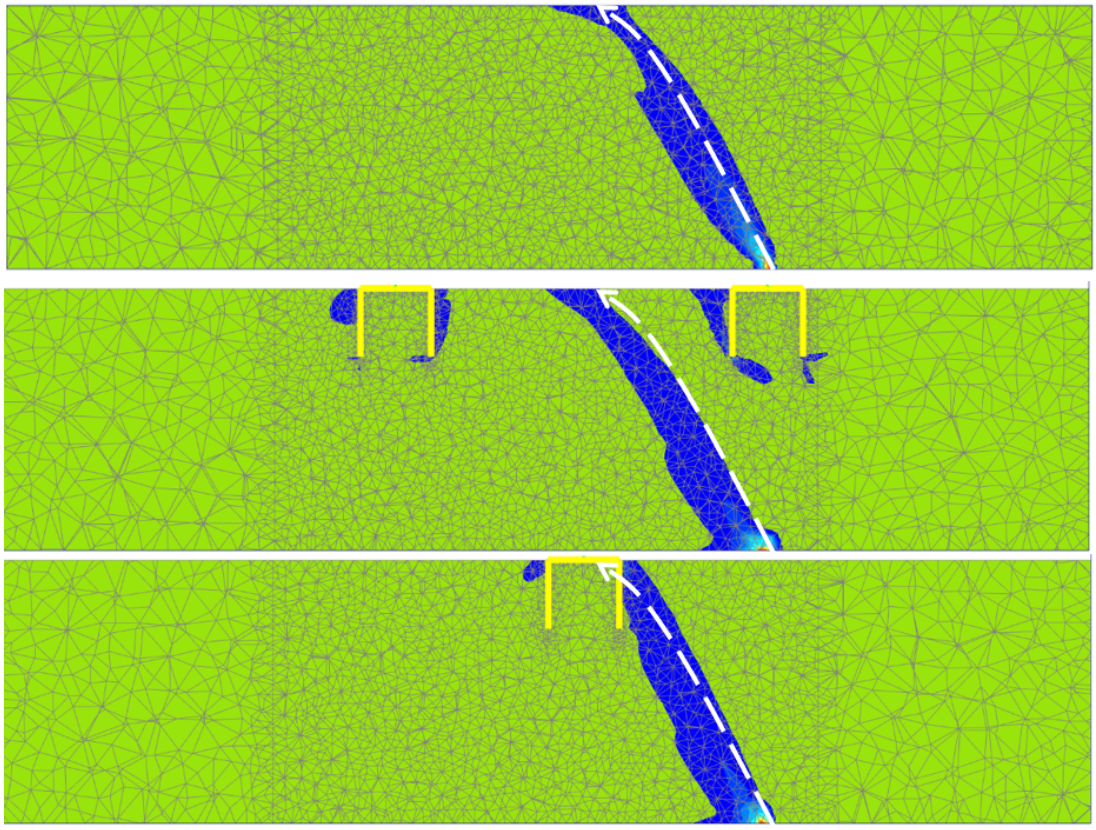

Figure 4.16. Comparison of plastic shear strain contours for Case B and $L/D = 1$. White dashed line indicates the free field path.

Figure 4.17 is validating the previous observations. It can be seen that the fault rupture path in plan view follows the free field path, except the location between buckets 1 and 2, where the shear zone is thinner and some shear strains are transmitted to the perimeter of the bucket's lid. In addition, bucket 3 shifts the path towards the hanging wall and is letting left side practically untouched.

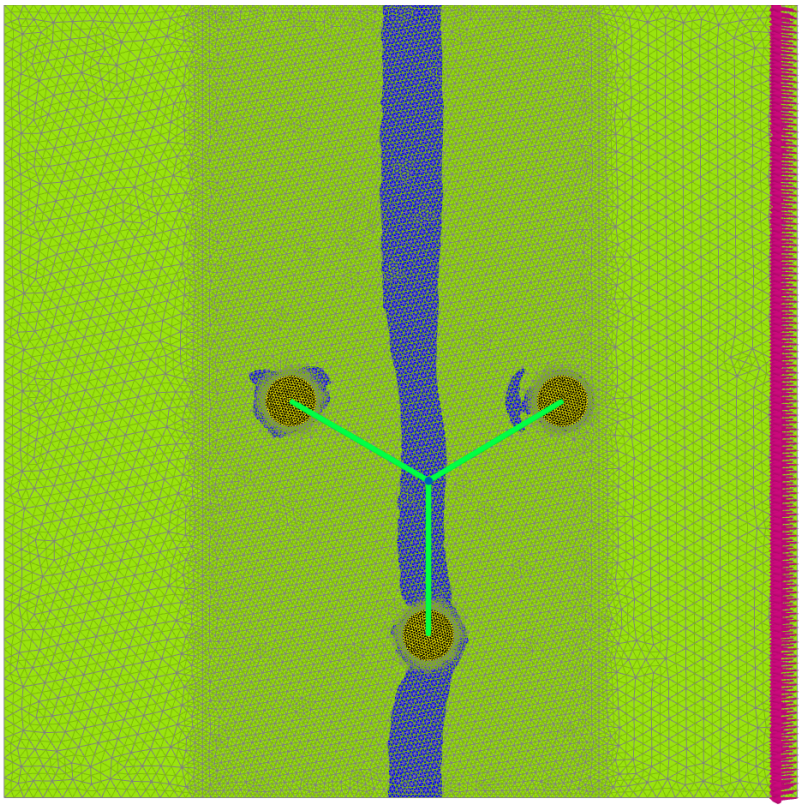

Figure 4.17. Plan view of the shear strain contours path, Case B and $L/D = 1$.

Figure 4.18 displays the settlement profile of the tripod. Observing the figure, the interaction mechanism is revealed, with bucket 1 being clearly to the hanging wall experiencing a serious uplifting surpassing 1 meter of dislocation. Bucket 3 is also in the hanging wall but the displacements along the positive z-axis are reduced reaching a maximum of 50 centimeters. Lastly, bucket 2 is following the rigid rotation of the whole structure and settles up to 20 centimeters. Based on that, it can be stated that the soil beneath bucket 3 acts like a cushion and withstands high stresses reducing the total settlements.

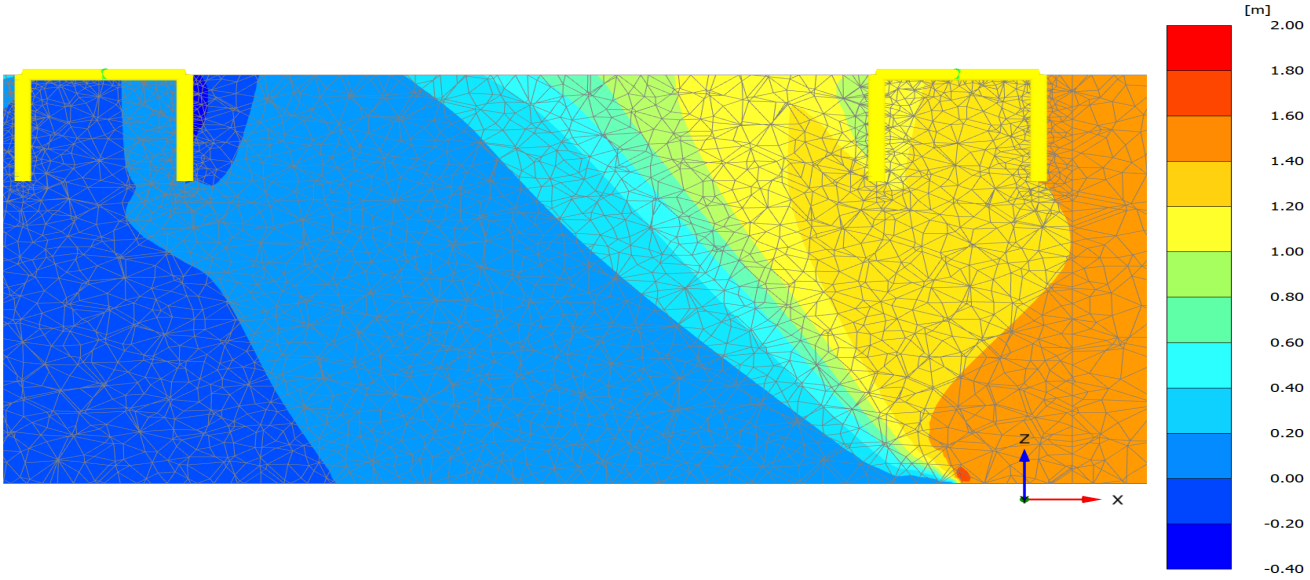

a) Buckets 1 and 2.

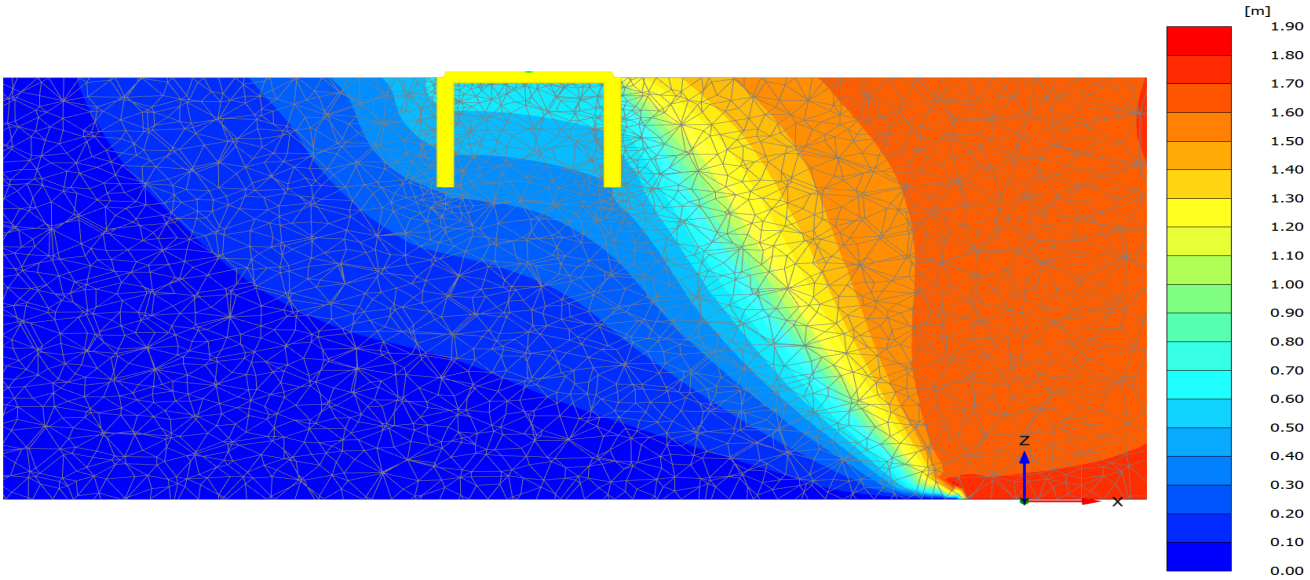

b) Bucket 3

Figure 4.18. Settlement profile, Case B and $L/D = 1$.

The Fault rupture-suction bucket tripod interaction mechanism based to the results displayed above is expected to create horizontal movement of the bucket and significant rotations on the tripod legs. Thereafter, the maximum and minimum horizontal displacements indicating the tripod rotation are displayed in Table 4.6.

Bucket	u_{xmin}[cm]	u_{xmax}[cm]
1	-67	-46
2	-60	-31
3	-57	-31

Table 4.6. Tripod horizontal displacements for Case B and $L/D = 1$.

Based on the horizontal displacements and the fact that the maximum and minimum values differ by approximately 30 centimeters in each bucket, it is safe to state that the buckets are rotating significantly. This rotation is transferring axial and moment loads on the connecting beams which despite the fact that for Case A did not rotate, now they are rotating for -2, 0.2 and 1.9 degrees for beam 1,2 and 3 respectively as shown in Figure 4.1.

Figure 4.19 presents the displaced buckets. It is clear that the structure is rotated and displaced along the negative x-axis experiencing significant deformations.

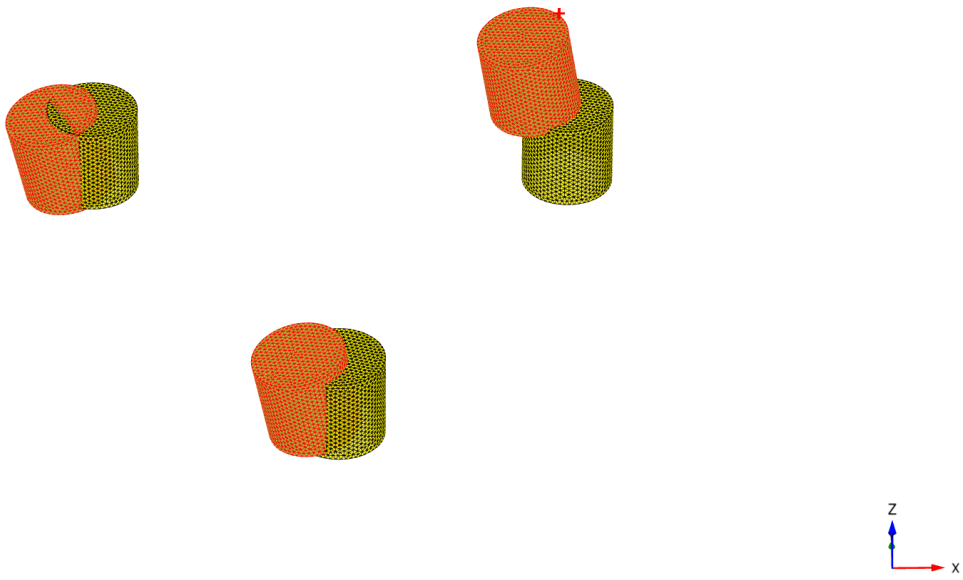

Figure 4.19. Deformed (red) versus stationary (yellow) tripod after fault rupture for Case B and $L/D = 1$.

Lastly, the forces acting on the tripod and the beam are presented in Tables 4.7 and 4.8, respectively. It is evident that the forces are increased compared to Case A and structural distress due to the fault rupture is present. Again, the forces acting on the tripod are higher, while the beams are being compressed axially.

Force	Units	Max	Min
N_1	MN/m	43.85	-44.36
N_2	MN/m	24.85	-23.43
Q_{12}	MN/m	19.87	-21.96
Q_{13}	MN/m	1112	-1619
Q_{23}	MN/m	460.2	-574.9
M_{11}	MNm/m	189.6	-207.2
M_{12}	MNm/m	79.47	-54.51
M_{22}	MNm/m	58.85	-55.32

Table 4.7. Maximum and minimum forces acting on the buckets for Case B and $L/D = 1$.

Force	Units	Max	Min
N	MN	-2.95	-24.63
Q_{12}	MN	10.1	-12.21
Q_{13}	MN	-5.97	-11.21
M_1	MNm	46.65	-33.84
M_2	MNm	128.7	-228.6
M_3	MNm	260.1	-216.9

Table 4.8. Maximum and minimum forces acting on the beams for Case B and $L/D = 1$.

The mechanism for reverse fault rupture-tripod suction bucket foundation for Case B and $L/D = 1$ can be summarized as:

1. Bucket 1 and 3 are attached to the hanging wall, while bucket two remains on the footwall.

2. The fault rupture path is alternated against the free field and outcrops outside of bucket 3 margins. Increased plastic shear strains are evident on the outside of the skirt and on the tips of the buckets

3. There is significant displacement and rotation of the entire structure. In addition, it tilts counterclockwise and this is causing settlements.

4. High loads are acting on both the buckets and the connection beams due to the fault rupture.

4.2.3 Case C

In Figure 4.20 the deformed tripod for Case C is depicted. In this scenario, the tripod is placed such as the free field fault rupture would outcrop under bucket 2. After an initial observation, the structure rotates while all three buckets are now behaving as founded in the hanging wall.

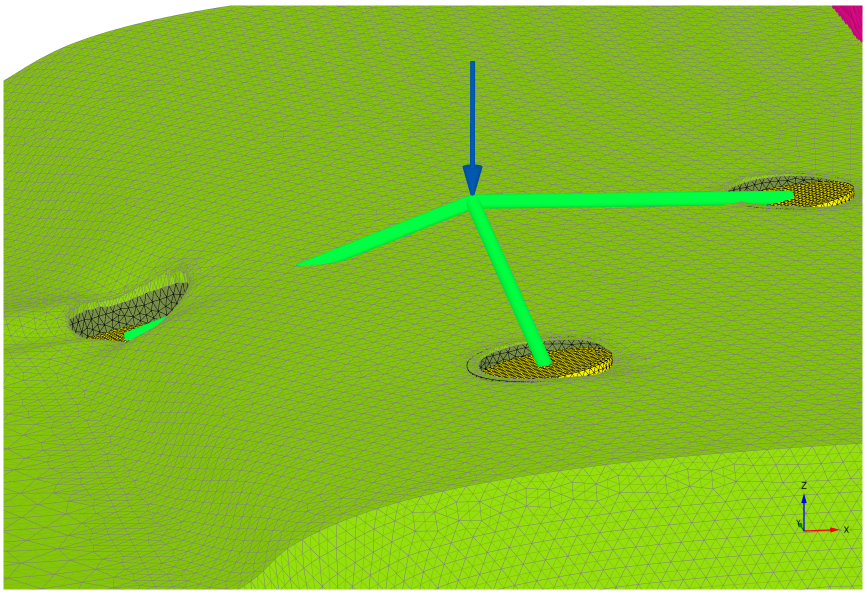

Figure 4.20. tripod deformation in true scale under reverse fault rupture for Case C and $L/D = 1$.

Figure 4.21 presents the plastic shear strain contours propagating from the fault scrap location to the surface. Again in this case, it is obvious that the presence of the tripod is affecting the fault rupture propagation. In the case of bucket 1 it is observed that it remains almost untouched with only a very small concentration around the left skirt and the tip. Regarding bucket 2, where the fault would outcrop with the absence of the structure, it can be claimed that plastic shear strains are circling the bucket with high concentrations in both skirts and between the two tips. An interesting observation in this scenario is that the inner area of the bucket remains again untouched, deviates and avoid the fault to outcrop. This can be due to the increased soil compaction under the bucket. Lastly, bucket 3 does not experiencing any shear strain around it but it is noted that the fault rupture path is bending slightly towards the footwall compared to the free field.

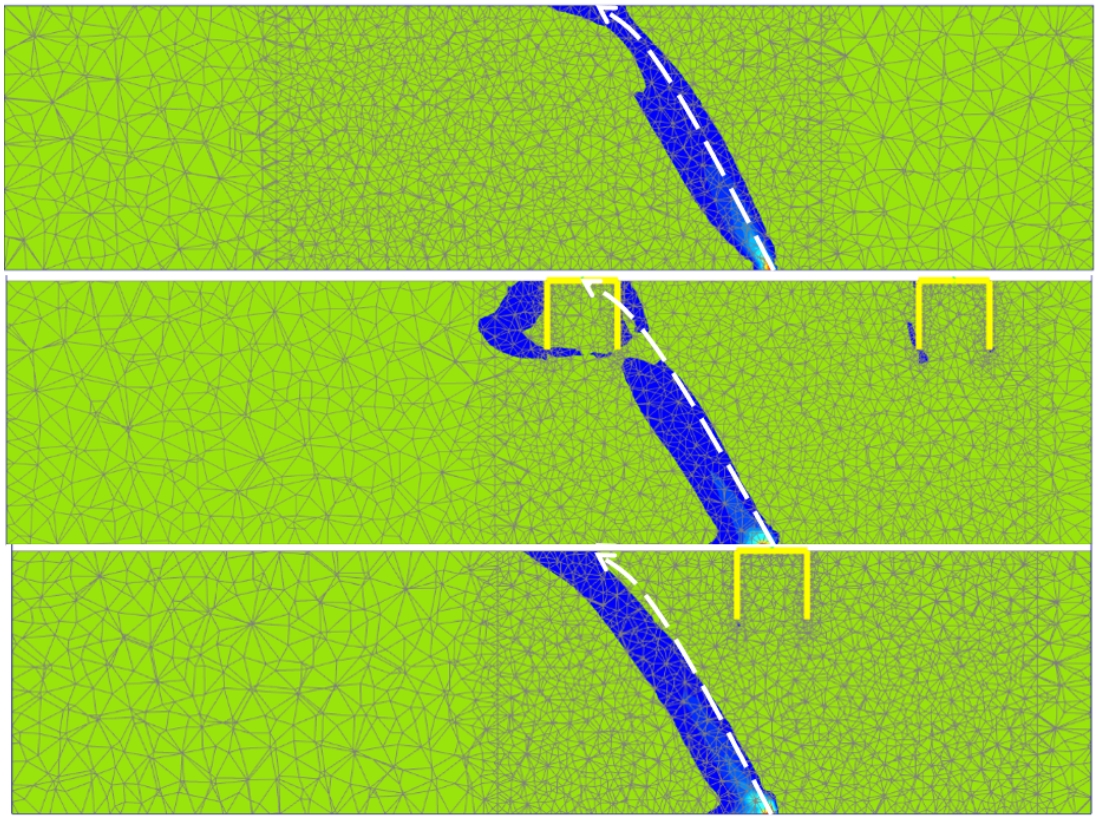

Figure 4.21. Comparison of plastic shear strain contours for Case C and $L/D = 1$. White dashed line indicates the free field path.

In Figure 4.22 a plan view of the model along with the plastic shear strains is presented. It can be noted that the buckets 1 and 3 are not showing any plastic shear strains on the surface, while bucket 2 is alternating the free field propagation.

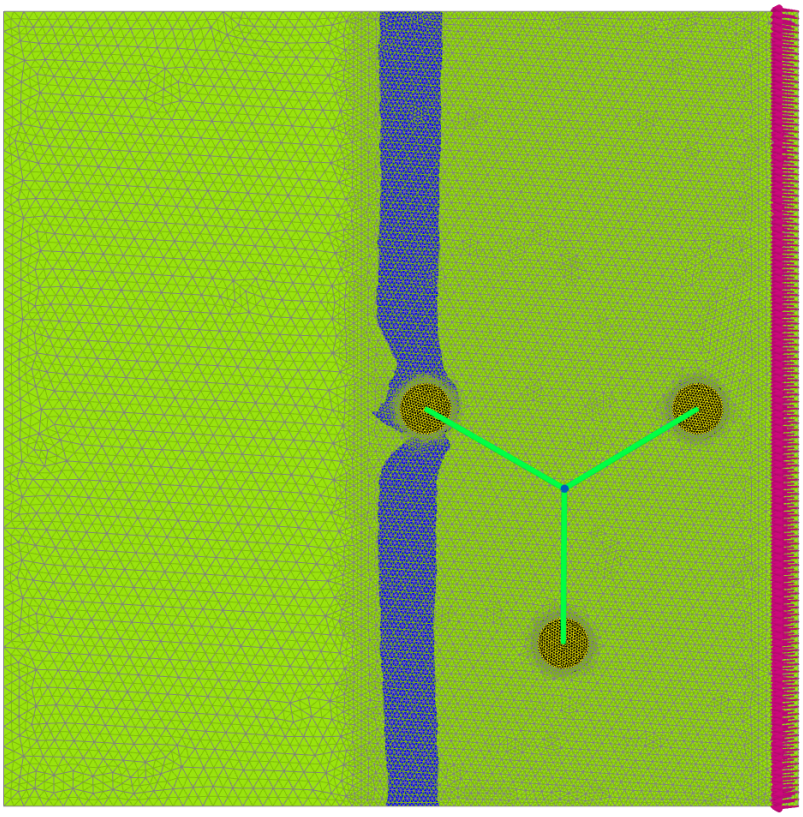

Figure 4.22. Plan view of the shear strain contours path, Case C.

Figure 4.23 depicts the settlement profile of the tripod. It can be seen that bucket 1 is completely in the hanging wall with uplifting dislocations almost equal to the bedrock offset. The same pattern is also observed for bucket 3 with slightly reduced upward displacements below the bucket which are also indicating the rotation due to the fault. Regarding bucket 2, where the fault should outcrop it is seen that even though it is behaving also as being in the hanging wall, the upward movement is relatively small compared to the size of the structure leading to a maximum of 30 centimeters. Based on that it can be claimed that the weight and size of the bucket, along with the compacted soil is in a large extent withstanding the tectonic dislocation.

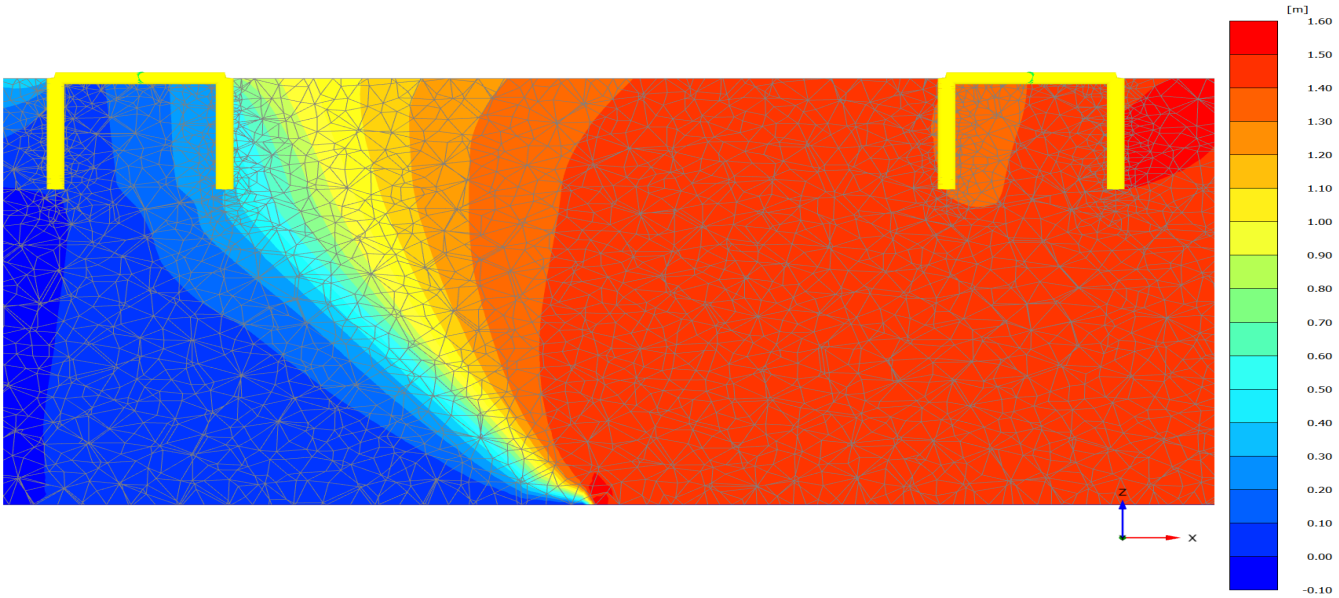

a) Buckets 1 and 2.

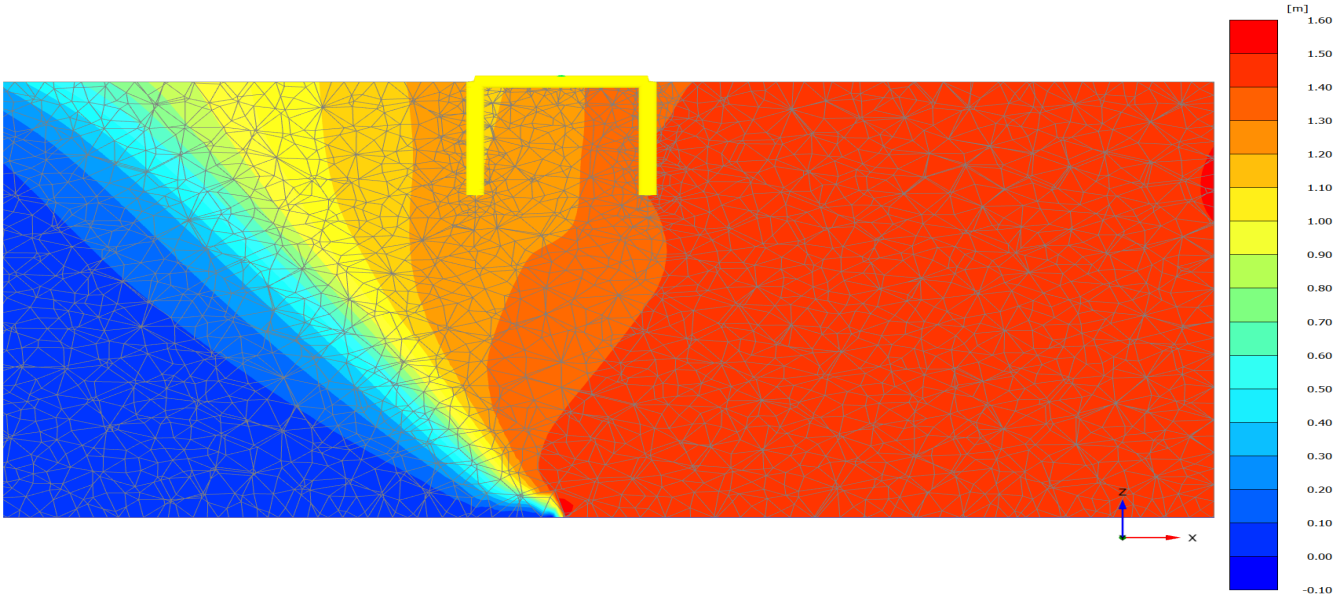

b) Bucket 3

Figure 4.23. Settlement profile, Case C and $L/D = 1$.

As it is already shown from the previous cases, the fault rupture is displacing the tripod horizontally. Hence, the maximum and minimum nodal horizontal displacement of each leg are presented in Table 4.9 . In this way, an estimation about the structural rotation can be made. It is seen that Case C produces the highest dislocations long the negative x-axis compared to the other cases, surpassing 1 meter. This dislocation is causing the connecting beams to rotate by -2, 1.72 and 0.18 degrees for beam 1, 2 and 3 respectively.

Bucket	u_{xmin}[cm]	u_{xmax}[cm]
1	-72	-93
2	-59	-91
3	-83	-104

Table 4.9. Tripod horizontal displacements for Case C and $L/D = 1$.

The deformed buckets are displayed in Figure 4.24. Here, the structural deformation is clear; the buckets on the right side (bucket 1 and 3) are moved upwards and tilt significantly while bucket 2 experiences smaller rotations.

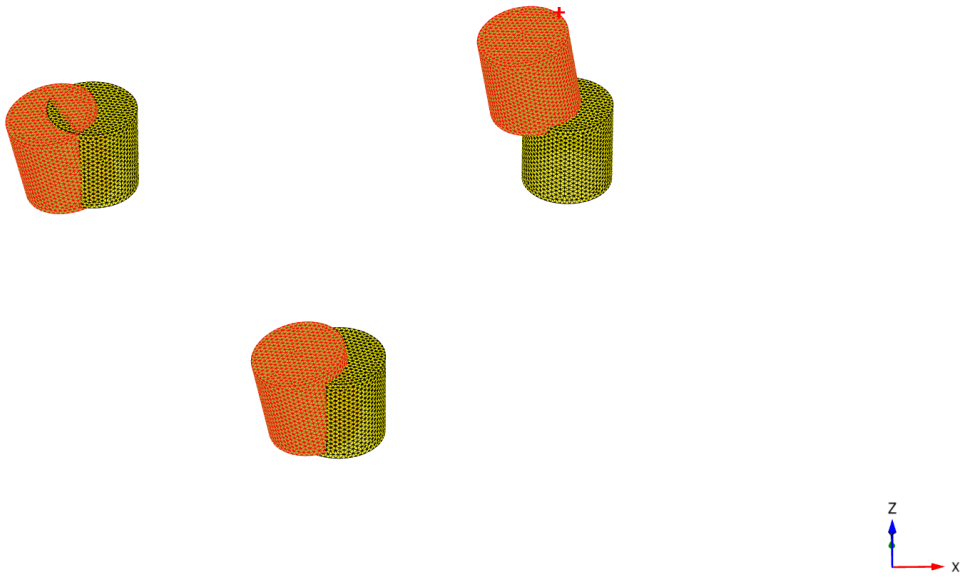

Figure 4.24. Deformed (red) versus stationary (yellow) tripod after fault rupture for Case C and $L/D = 1$.

The last data set examined for Case C are the forces acting on the legs and the connection beams in Tables 4.10 and 4.11. Comparing with Case B, the loads on the plates are similar with some deviations evident with respect to the type of the loading. Similar pattern is observed in the beams, while they are again compressed axially due to the fault rupture.

Force	Units	Max	Min
N_1	MN/m	36.34	-32.17
N_2	MN/m	19.06	-16.43
Q_{12}	MN/m	19.24	-16.33
Q_{13}	MN/m	1040	-1205
Q_{23}	MN/m	517.1	-338.4
M_{11}	MNm/m	133.1	-150.3
M_{12}	MNm/m	50.46	-66.56
M_{22}	MNm/m	65.17	-58.02

Table 4.10. Maximum and minimum forces acting on the tripod for Case C and $L/D = 1$.

Force	Units	Max	Min
N	MN	-3.85	-19.12
Q_{12}	MN	9.63	-5.53
Q_{13}	MN	-4.087	-14.44
M_1	MNm	81.33	-56.33
M_2	MNm	80.80	-255.2
M_3	MNm	125.1	-217.3

Table 4.11. Maximum and minimum forces acting on the beams for Case C and $L/D = 1$.

The mechanism for reverse fault rupture-tripod suction bucket foundation for Case C and $L/D = 1$ can be summarized as:

1. All three buckets are being carried away from the hanging wall and displace upwards.

2. The fault rupture path is alternated against the free field and emerges all round bucket 2. The plastic shear strain band on the other two buckets is small.

3. There is significant displacement and rotation of the entire structure while it tilts counter-clockwise which also creates settlements.

4. High loads are acting on both the buckets and the connection beams due to the fault rupture.

4.3 Discussion of results for L/D=1

In this section, a summary of the results for all three cases with $L/D = 1$ ratio are presented and discussed. Case A is the most beneficial in all the aspects due to the fact that all the buckets stay in the footwall. Thus, the contact area of the foundation is large, the loads acting due to the fault the lowest and no structural rotation is observed. The rupture influences the tripod only by dislocating it approximately 15 centimeters along the negative x-axis. In addition, the plastic shear strains tend to avoid the the structure and the fault emerges in the vicinity of the skirt.

In the comparison of Cases B and C it is seen that they both create significant structural rotation. In terms of horizontal displacement Case B is beneficial, On the other hand, Case C is beneficial in terms of settlements since it remains on the footwall while the structural rotation of Case B creates settlements. In terms of acting loads Case C is again better than Case B with some exemptions.

Overall, considering the fact that the tripod behaves as a rigid body meaning that the horizontal displacement might not be damaging, it can be claimed that Case B, where the fault is about to outcrop below bucket 3 is the worst case scenario for $L/D = 1$.

4.4 L/D=0.5

In this section, the L/D ratio is reduced to 0.5 to see how it affects FR-SFSI. The bucket diameter remains 6.5 meters but the skirt length is changed to 3.25 meters, while the rest of the parameters are the same, with 1.5 meters reverse fault which outcrops at $x = 3.5m$ and vertical load equal to 34.7 MN. The tripod is placed so the free field fault with the absence of the bucket would outcrop below each bucket subsequently, as in the previous analysis with $L/D = 1$.

4.4.1 Case A

Figure 4.25 illustrates the deformed tripod for 1.5 meters reverse fault rupture with L/D ratio equal to 0.5. The tripod is placed in a position where the free filed fault would outcrop below bucket 1. It is evident from the figure that similar with the scenario with $L/D = 1$ there is nor visible structural rotation or settlement and the tripod remains on the footwall.

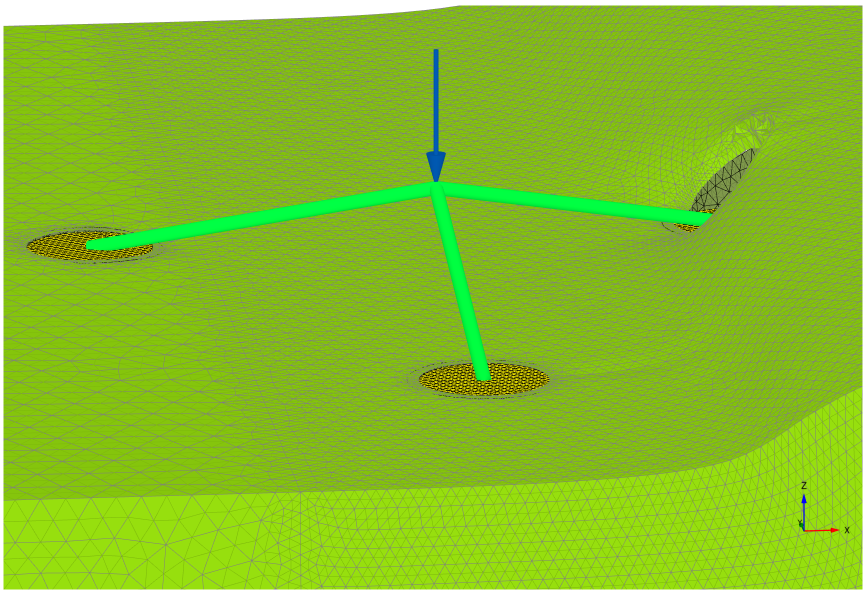

Figure 4.25. tripod deformation in true scale under reverse fault rupture for Case A and $L/D = 0.5$.

Figure 4.26 presents the plastic shear strain path for the free field model, against the model with the presence of the tripod. The response is identical to the long skirted tripod. For bucket 1, the rupture fails to outcrop below the bucket, is deviated bending towards the hanging wall and outcrops in the top right corner of the leg. As for bucket 3, the fault rupture propagates as of the free field with the only difference being a small increase of shear strains until a depth of approximately 8 meters. In addition, it is angled towards the footwall. Finally, bucket 2 remains practically untouched from the tectonic movement.

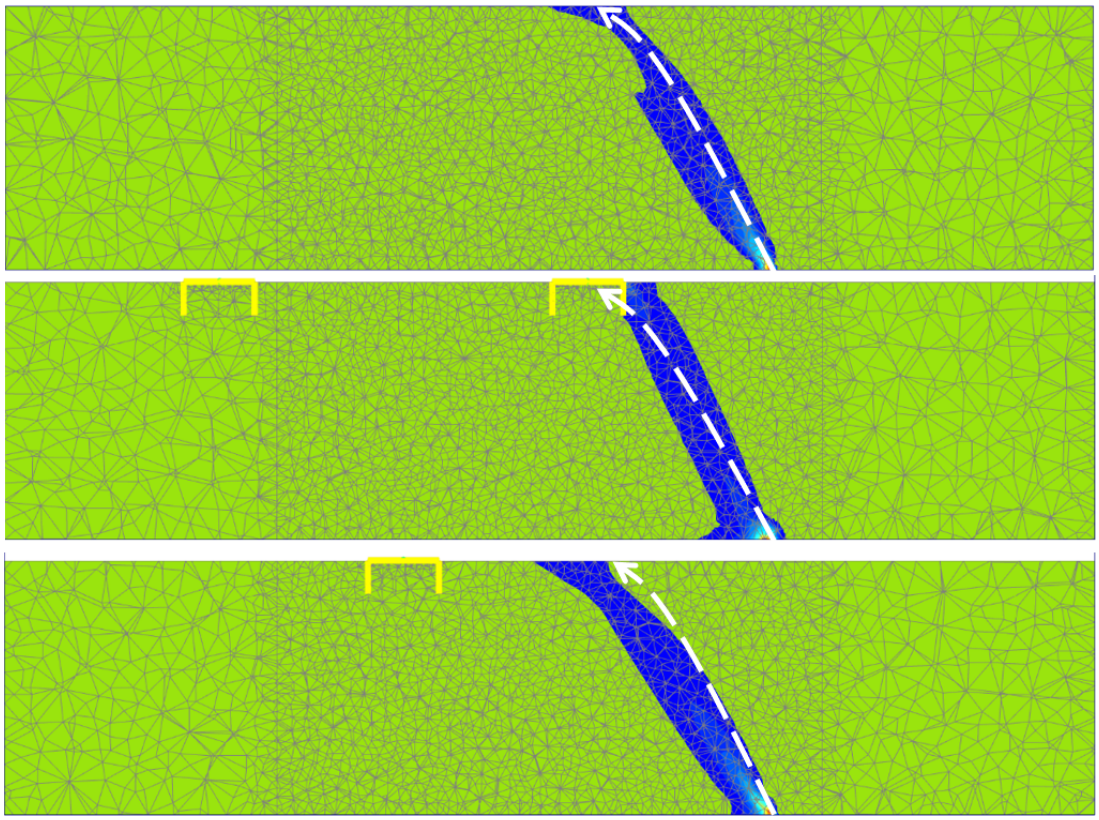

Figure 4.26. Comparison of plastic shear strain contours for Case A and $L/D = 0.5$. White dashed line indicates the free field path.

The plan view of the model, presented in Figure 4.27 is validating the above mentioned results. The result is very similar with the one from $L/D = 1$, where there is a small increase in plastic shear strain on the right edge of bucket's 1 skirt, while the left edge does not experience any plastic shear strains.

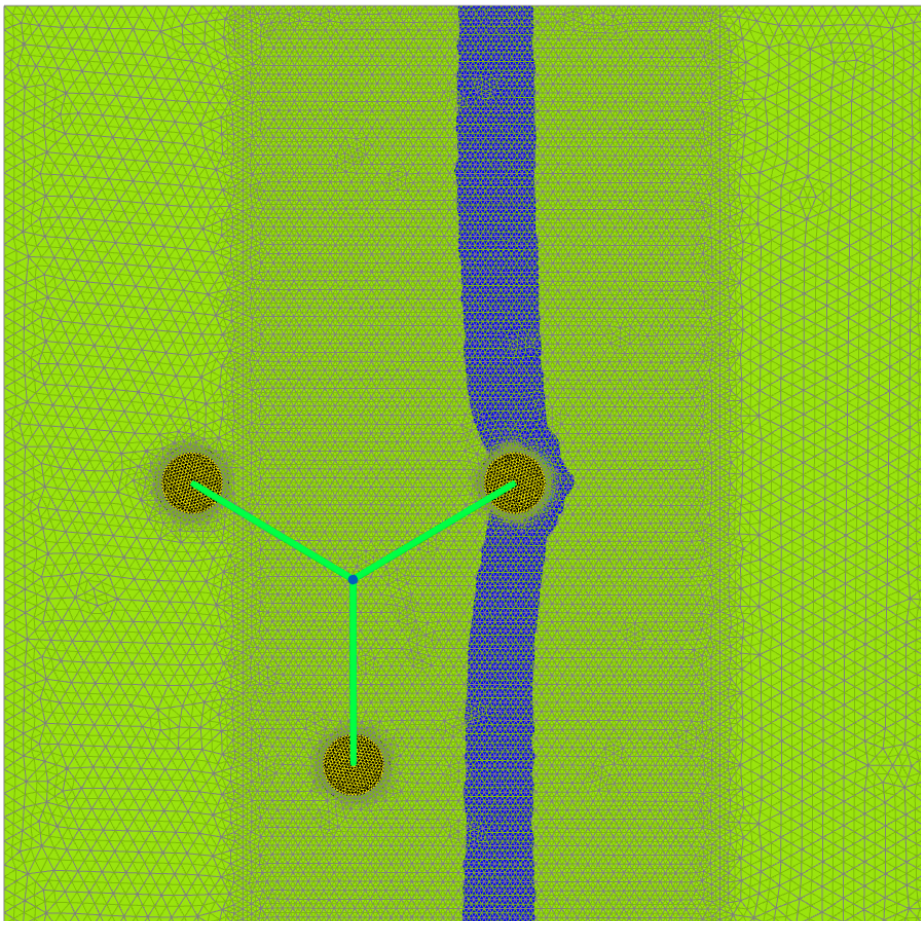

Figure 4.27. Plan view of the shear strain contours path, Case A and $L/D = 0.5$.

Figure 4.28 presents the settlements and upward movement caused by the reverse fault rupture. In this case also, the results are not affected by the skirt length. The settlements below the buckets are close to zero, while no upward movement due to the reverse fault rupture is spotted.

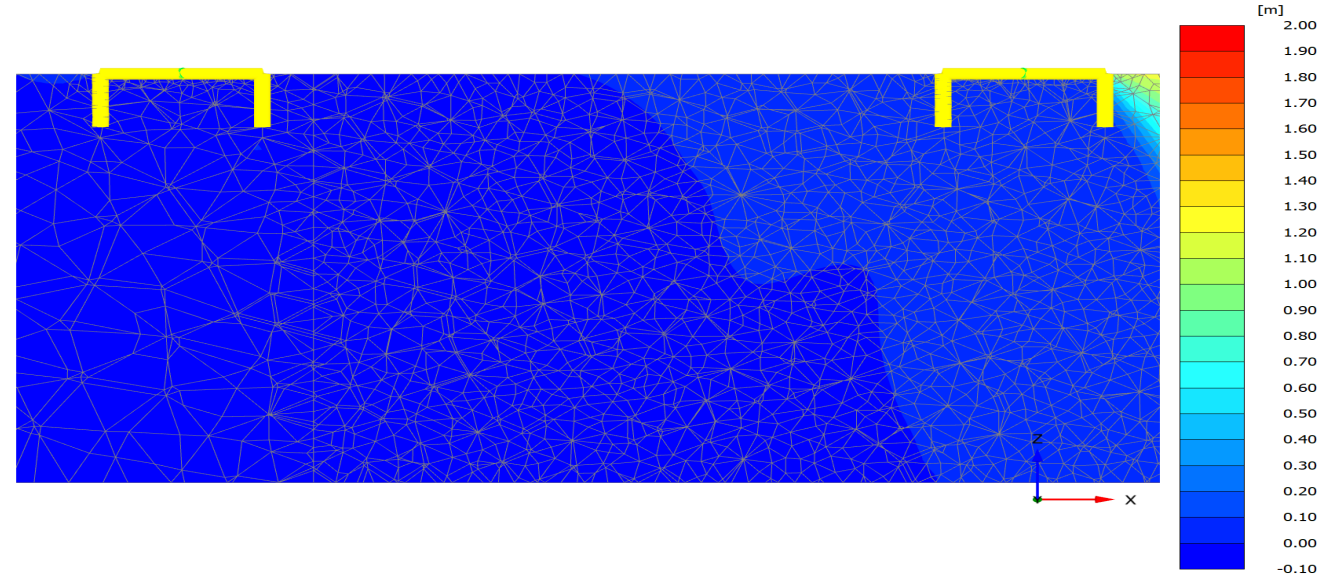

a) Buckets 1 and 2.

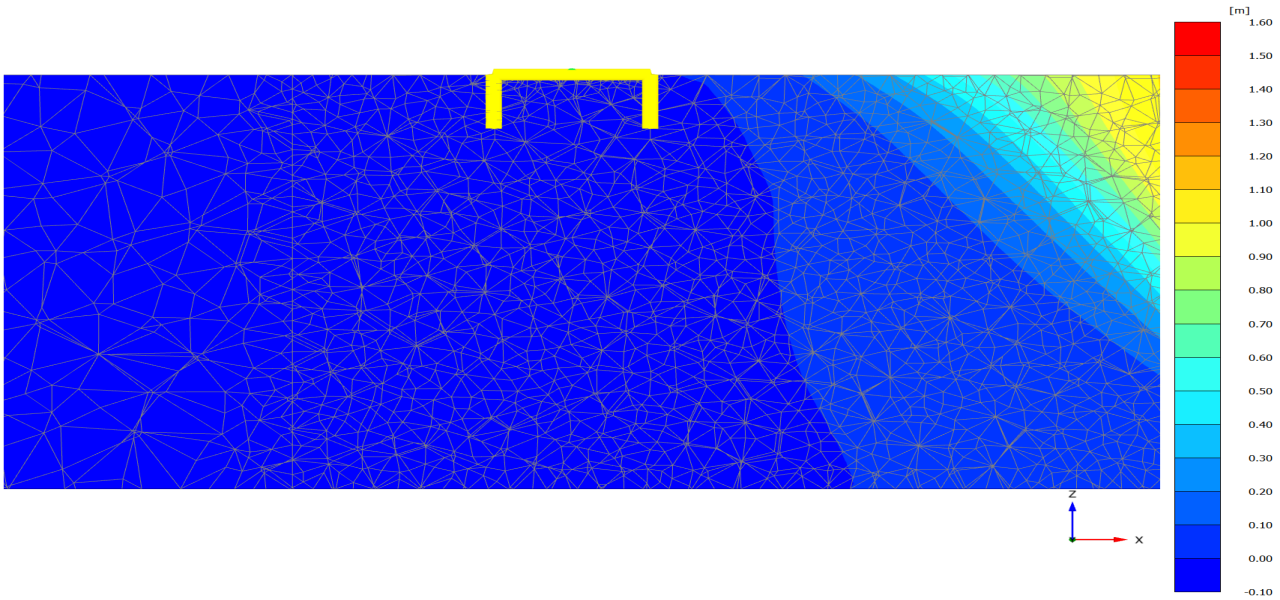

b) Bucket 3

Figure 4.28. Settlement profile, Case B.

The horizontal displacement of the buckets is presented in Table 4.12. It can be noted that there is no significant nodal differential displacements which indicates the absence of structural rotations, while the maximum of the tripod dislocation is 15.5 centimeters.

Bucket	u_{xmin}[cm]	u_{xmax}[cm]
1	-15	-155
2	-11	-12
3	-9	-10

Table 4.12. Tripod horizontal displacements for Case A and $L/D = 0.5$.

The displaced buckets are presented in Figure 4.29. Note that the deformation is scaled up to 5 times to reveal the mechanism. It is obvious that no matter the short skirt, the tripod is not displaced or deformed in a way that could question the structural integrity.

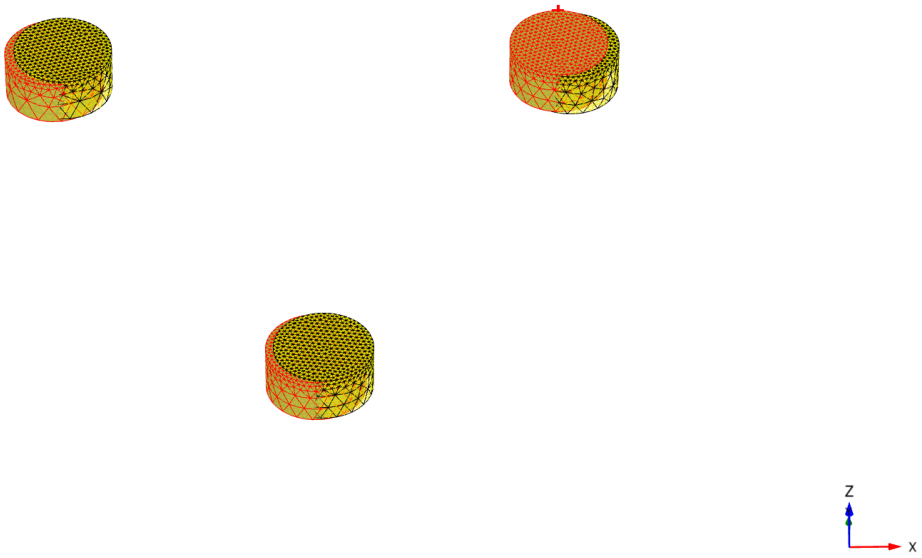

Figure 4.29. Deformed (red) versus stationary (yellow) tripod after fault rupture for Case A and $L/D = 0.5$.

Finally, the maximum and minimum nodal forces acting on the tripod are presented in Table 4.13 and discussed furthermore. If those forces are compared with the scenario of $L/D = 1$, it can be observed that are halved , while the pattern in terms of which of the forces are the highest remains the same.

Force	**Units**	**Max**	**Min**
N_1	MN/m	18.01	-23.35
N_2	MN/m	7.76	-6.03
Q_{12}	MN/m	10.40	-8.47
Q_{13}	MN/m	324.2	-349.7
Q_{23}	MN/m	106.6	-142.3
M_{11}	MNm/m	45.01	-40.72
M_{12}	MNm/m	13.72	-18.36
M_{22}	MNm/m	8.46	-19.35

Table 4.13. Maximum and minimum forces acting on the buckets for Case A and $L/D = 0.5$.

Table 4.14 presents the loads that are imposed to the connecting beams by the fault rupture. As in the buckets, the forces in the beams are halved compared to the tripod with skirt equal to 6.25 meters and $L/D = 1$.

Force	Units	Max	Min
N	MN/m	-3.04	-12.42
Q_{12}	MN	4.07	-5.46
Q_{13}	MN	-8.88	-12.77
M_1	MNm	10.34	15.12
M_2	MNm	28.05	-242.5
M_3	MNm	115.2	-84.47

Table 4.14. Maximum and minimum forces acting on the beams for Case A and $L/D = 0.5$.

1. All three buckets remain on the footwall.

2. The fault rupture path is alternated against the one with the absence of the structure and emerges on the right side of bucket's 1 skirt.

3. The tripod is displaced along the negative x-axis. The amount of this displacement is small, while the rotations are close to zero. No damaging settlements are noted.

4. The fault is imposing loads on both the buckets and the connection beams due to the fault rupture.

5. The response overall is very similar with the case of $L/D = 1$, except the forcing acting on the tripod. Those forces reduced by approximately 50% for $L/D = 0.5$.

4.4.2 Case B

Figure 4.30 presents the deformed tripod with 1.5 meters reverse fault for Case B, where the rupture would emerge below bucket 3. It can be seen that the tripod is experiencing significant rotation with bucket 1 being in the hanging wall, bucket 2 on the footwall and bucket three, where the fault should emerge is also being slightly lifted up.

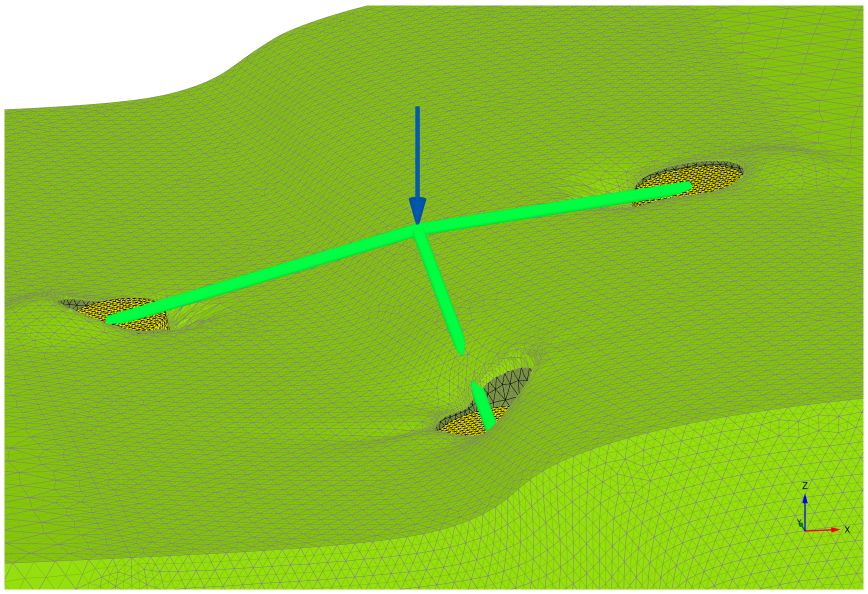

Figure 4.30. tripod deformation in true scale under reverse fault rupture for Case A and $L/D = 0.5$.

Figure 4.31 depicts the plastic shear strain propagation. The white dashed line indicates the free field response with the absence of the structure. As it can be seen, the path slightly bends towards the footwall between buckets 1 and 2, while shear strain concentration appears around the skirt and on the tip of the buckets. In case of bucket 3, below which the fault should emerge it is evident that the presence of the tripod leg tends to make the fault avoid the structure and outcrops on the right skirt. A small strain concentration appears on the top left part of the bucket also.

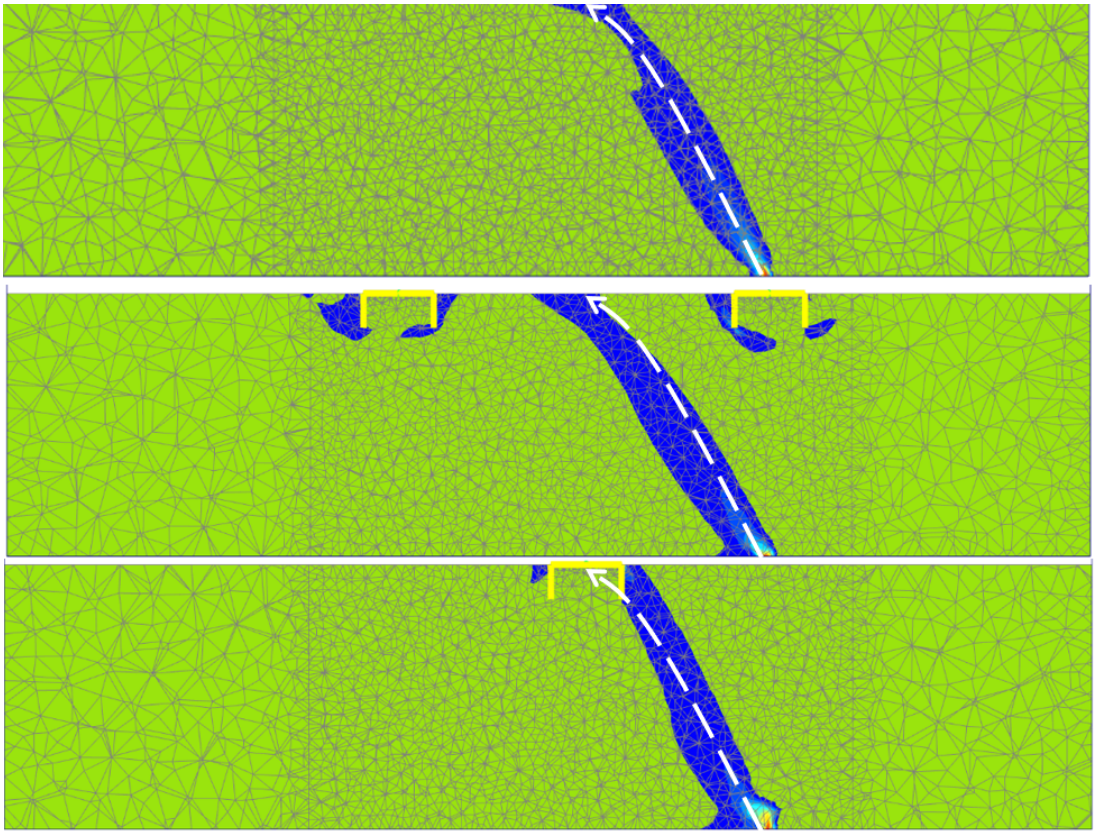

Figure 4.31. Comparison of plastic shear strain contours for Case B and $L/D = 0.5$. White dashed line indicates the free field path.

Figure 4.32 is validating the above mentioned results. The result is very similar with the one from $L/D = 1$, where the shear strain zone follows the free field path except the location between buckets 1 and 2, where some of the shear is transmitted at the buckets. In bucket 3, the fault rupture bends towards the hanging wall and avoids the structure.

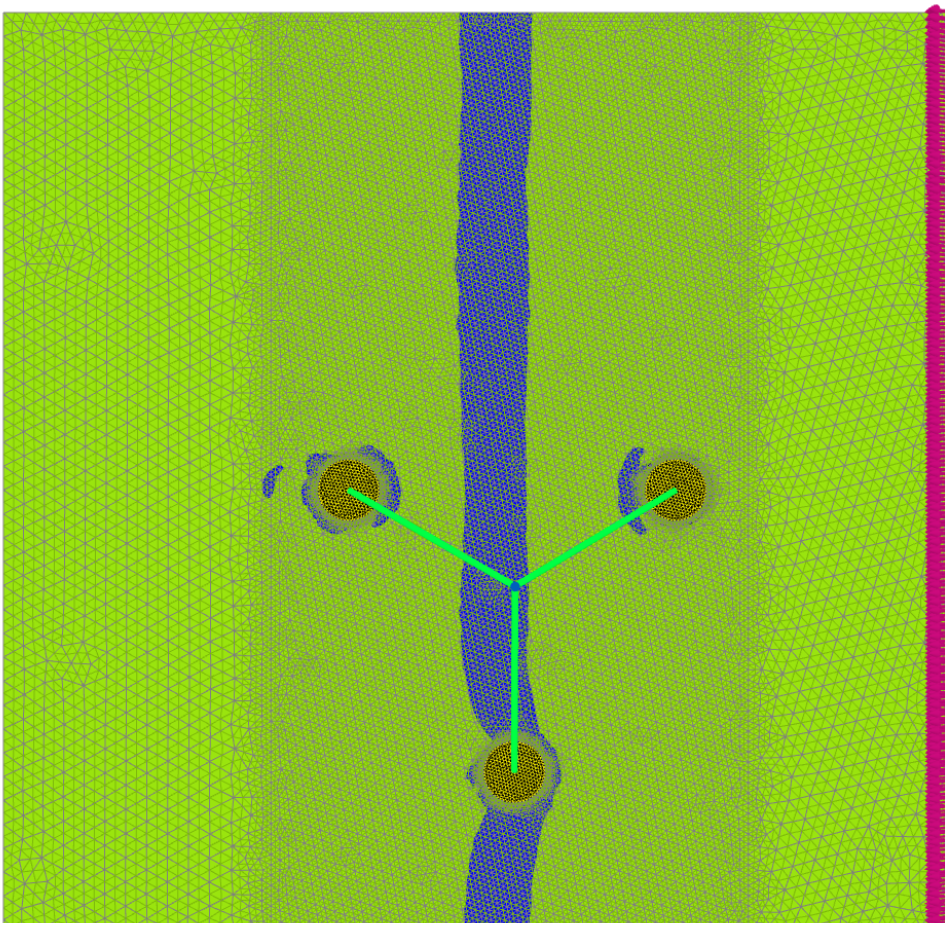

Figure 4.32. Plan view of the shear strain contours path, Case B and $L/D = 1$.

Figure 4.33 illustrates the settlement profile for this scenario. It can be seen that bucket 1 is as expected at the hanging wall experiencing structural rotation due to the differential settlement below the lid. The same pattern is visible for bucket 2 with the difference of it being in the footwall. The response overall for these two buckets is very similar with the response for $L/D = 1$. On the other hand, the behavior is alternated for bucket 3, where the fault outcrops. In this scenario, the bucket is lifted upwards for only approximately 20 centimeters, while for the case with the longer skirt the upwards displacement was up to 60 centimeters.

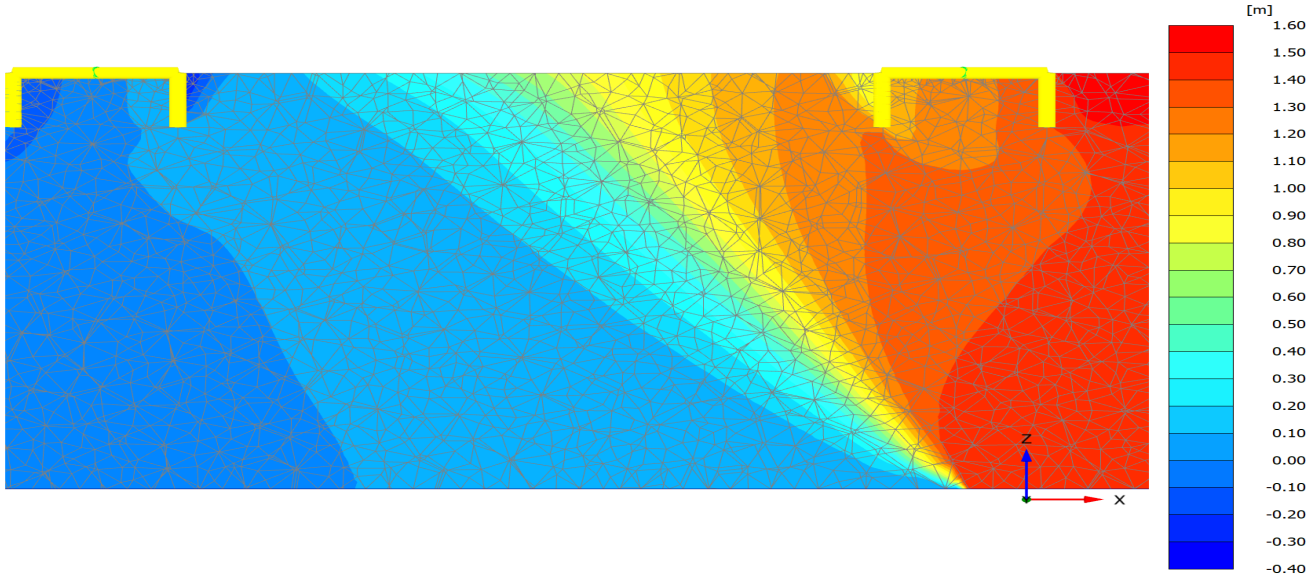

a) Buckets 1 and 2.

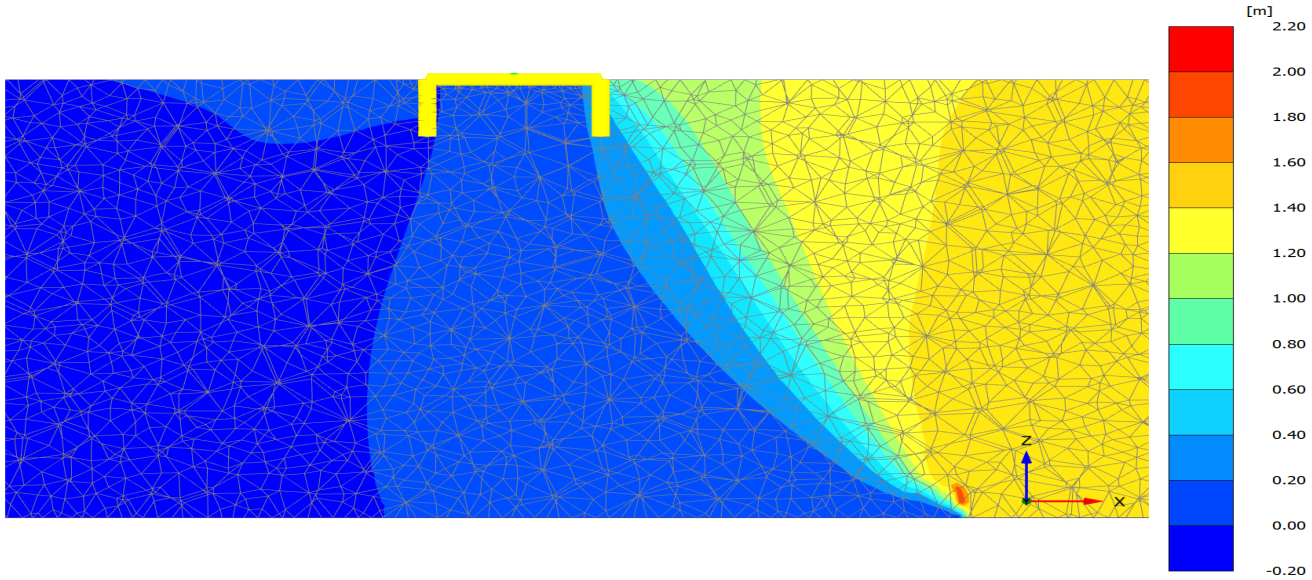

b) Bucket 3

Figure 4.33. Settlement profile, Case B and $L/D = 1$.

Table 4.15 presents the maximum and minimum nodal horizontal displacement. It is evident that the bucket displaces and rotates as a rigid structure due to fault rupture, while the values for $L/D = 0.5$ are smaller than the case examined previously with the longer skirt.

Bucket	$\mathbf{u_{xmin}}$**[cm]**	$\mathbf{u_{xmax}}$**[cm]**
1	-47	-65
2	-39	-62
3	-41	-54

Table 4.15. Tripod horizontal displacements for Case B.

The displacements and rotations experienced by the bucket are transferring loads to the connection beam and developing rotations equal to 2.08, 0.28 and 1.91 degrees for beam 1, 2 and 3 respectively, which are very similar with Case B of $L/D = 1$.

Figure 4.34 presents the displaced buckets. The mechanism is clear; There is both counter-clockwise rotational and transitional movement of the buckets legs, with bucket 1 being the most outplaced.

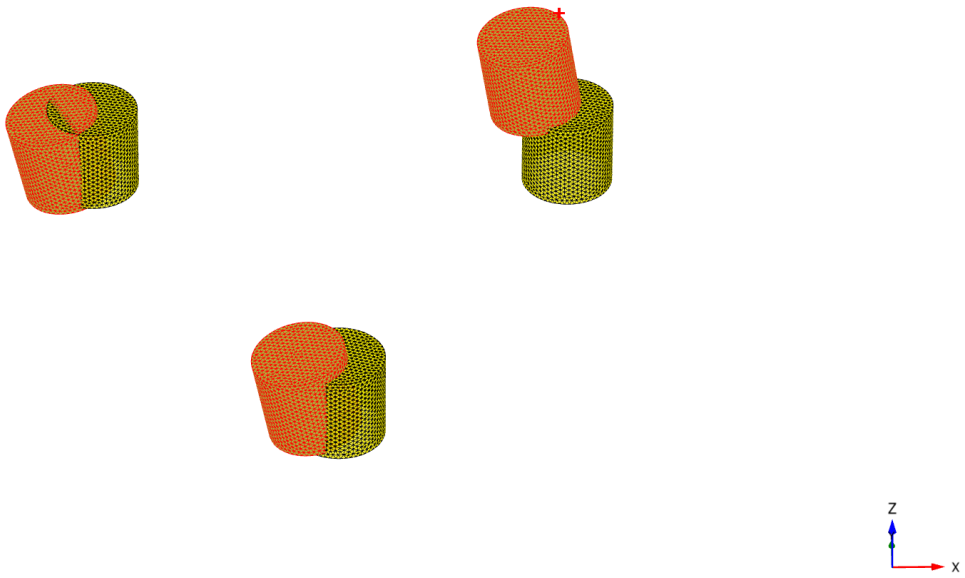

Figure 4.34. Deformed (red) versus stationary (yellow) tripod after fault rupture for Case B.

Finally, the forces acting on the tripod and the beam are presented in Tables 4.16 and 4.17, respectively. One can note that the response is similar with the study with $L/D = 1$, meaning the beams are being compressed but in this case the values for all types of resulting forces are approximately halved.

Force	Units	Max	Min
N_1	MN/m	26.61	-26.77
N_2	MN/m	11.46	-9.29
Q_{12}	MN/m	11.62	-12.86
Q_{13}	MN/m	330.8	-625.0
Q_{23}	MN/m	177.4	-218.6
M_{11}	MNm/m	71.44	-82.34
M_{12}	MNm/m	31.51	-21.10
M_{22}	MNm/m	21.40	-24.12

Table 4.16. Maximum and minimum forces acting on the buckets for Case B.

Force	Units	Max	Min
N	MN	-2.44	-16.02
Q_{12}	MN	6.72	-7.58
Q_{13}	MN	-8.06	-12.16
M_1	MNm	17.47	-8.57
M_2	MNm	50.28	-241.7
M_3	MNm	159.5	-130.8

Table 4.17. Maximum and minimum forces acting on the beams for Case B.

The mechanism for reverse fault rupture-tripod suction bucket foundation for Case B and $L/D = 1$ can be summarized as:

1. Bucket 1 and 3 are attached to the hanging wall, while bucket 2 remains on the footwall.

2. The fault rupture path is alternated against the free field and emerges on the right side of bucket's 3 skirt. Increased plastic shear strains are evident around all buckets.

3. There is significant displacement and rotation of the entire structure, it tilts counter-clockwise and settlements are also created.

4. The loads acting on both the buckets and the connection beams due to the fault rupture are half of them for $L/D = 1$.

5. Overall, shorter skirt seems to beneficial for this case in terms of the loads acting on the tripod and the horizontal dislocation.

4.4.3 Case C

Case C is scenario where the free field fault rupture would outcrop below bucket 2 and the deformed soil volume for this case can be seen in Figure 4.35. It is noted that the tripod rotates as a rigid body experiencing high levels of deformations, with all three buckets behave as founded in the hanging wall.

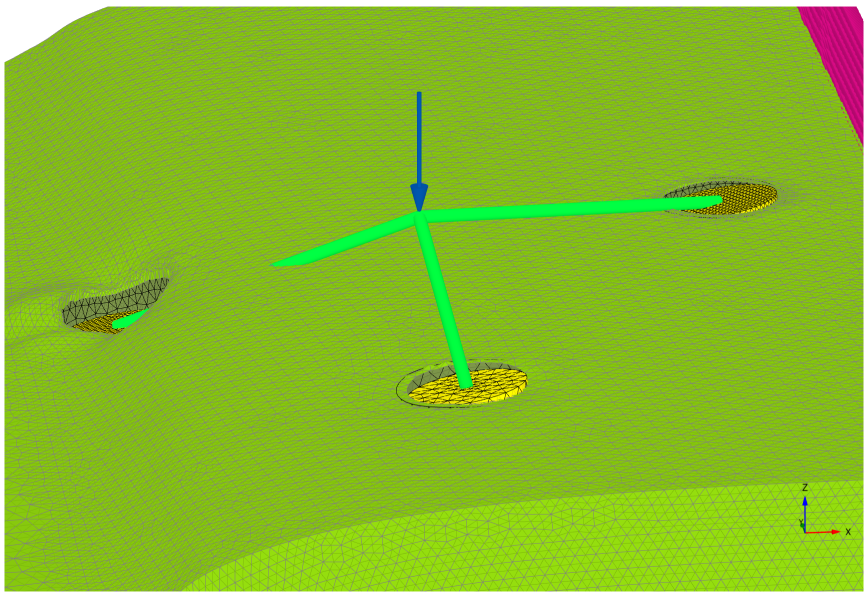

Figure 4.35. tripod deformation in true scale under reverse fault rupture for Case C and $L/D = 0.5$.

Afterwards, the plastic shear strains created by the fault rupture and their path are investigated. Figure 4.36 depicts that the presence of the structure is bifurcating the fault rupture path. Bucket 1 is practically not affected by the fault, experiencing only a small amount on the left tip. On the other hand bucket 2, where the fault would outcrop with the absence of the structure is alternating the path and lead the fault to outcrop in the vicinity of the right side skirt. Also, high shear strain concentration is visible on the left side of the bucket as well as below the left tip. It can be stated that the mechanism is different than the one with $L/D = 1$, where the right tip leads a higher amount of strains "pass" below the bucket, while a smaller amount is present on the right side of the skirt. Lastly, bucket 3 does not have any shear strain localisation due to the fault, while the path diverts towards the footwall compared to the free field.

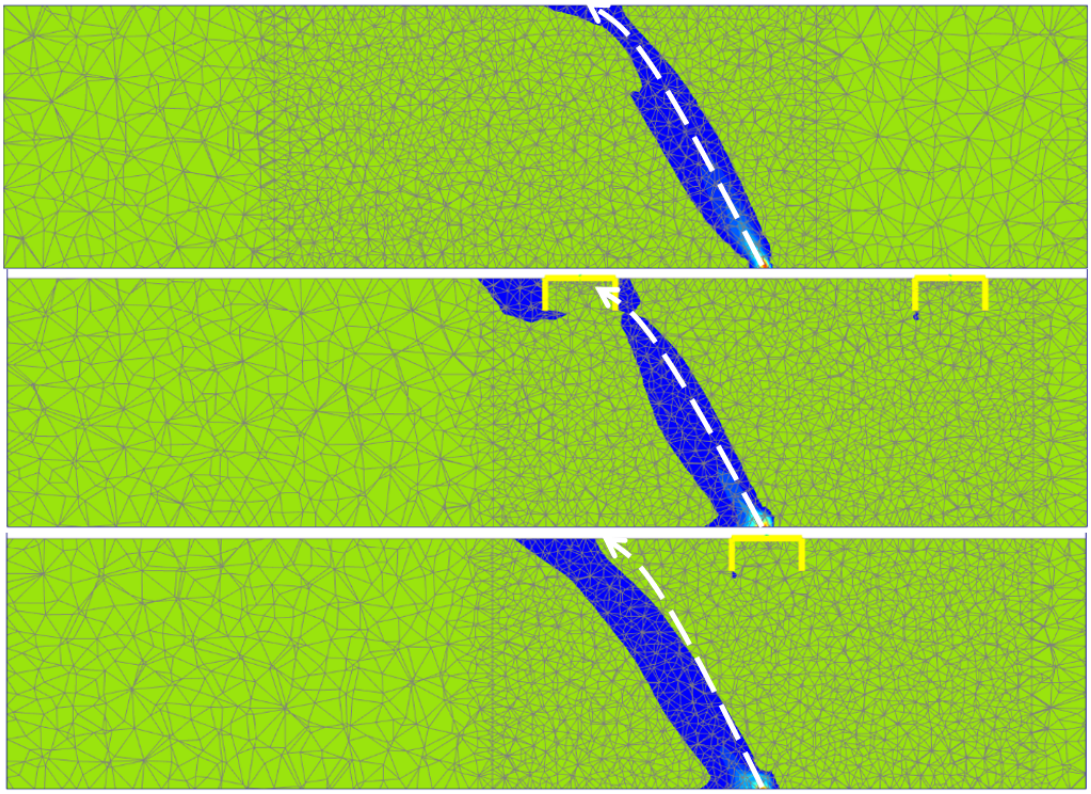

Figure 4.36. Comparison of plastic shear strain contours for Case C and $L/D = 0.5$. White dashed line indicates the free field path.

In Figure 4.37 a plan view of the model with the shear strain concentration is depicted. It is evident that buckets 1 and 3 are practically untouched, while bucket 2 is causing the rupture to divert and plastic shear strains are accumulating on the left side of the bucket.

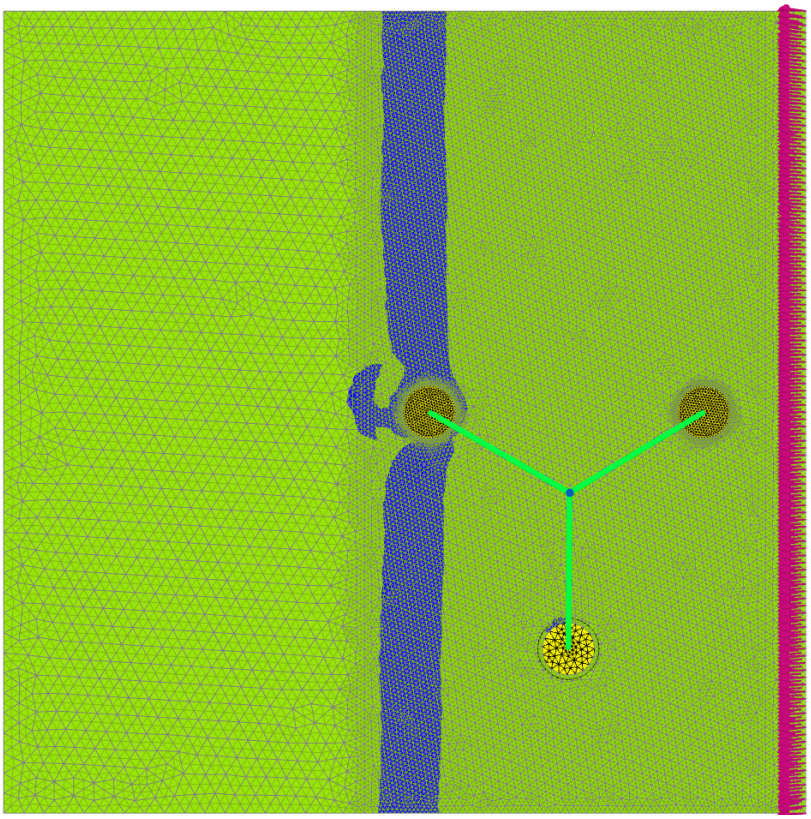

Figure 4.37. Plan view of the shear strain contours path, Case C and $L/D = 0.5$.

The settlement profile of the soil around the tripod is presented in Figure 4.38. Bucket 1 is drifting to the hanging wall and the upward displacement reaches 1.5 meters, equal to the bedrock offset. Also, it is noted that on the left side below the lid the upward displacement is smaller, enforcing it to rotate. Bucket 3 experiences the same pattern with slightly reduced displacements and equivalent rotations. Regarding bucket 2, it is dragged from the fault, but the upwards displacements are smaller reaching approximately 25 centimeters and rotating as well.

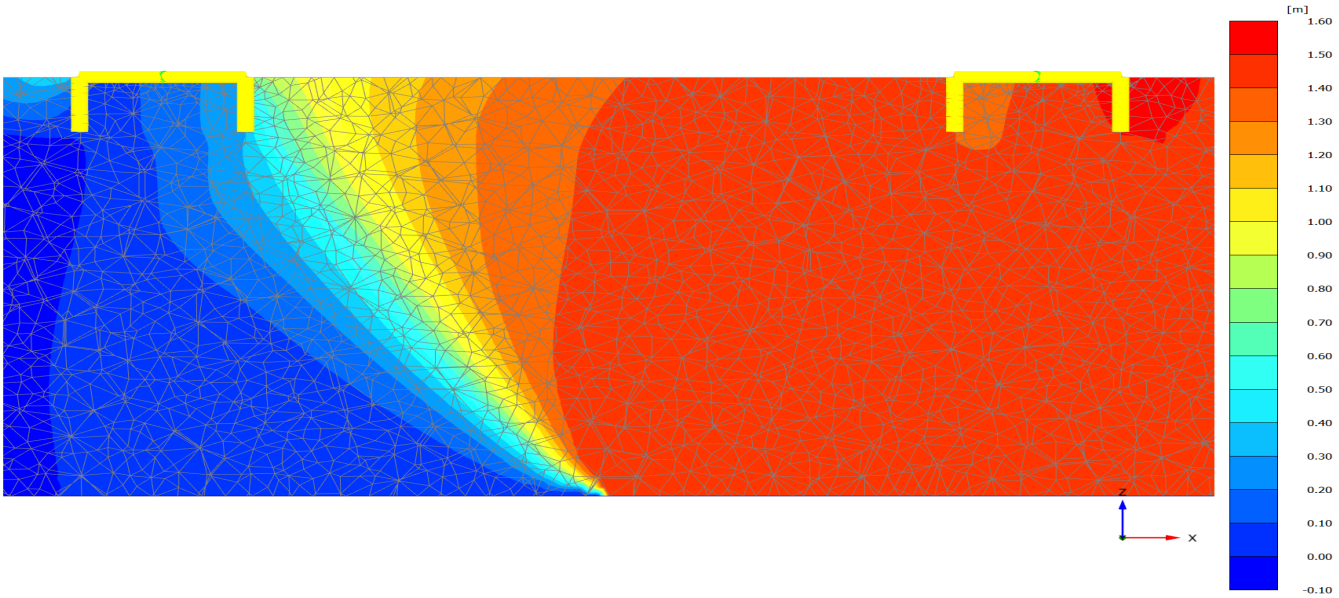

a) Buckets 1 and 2.

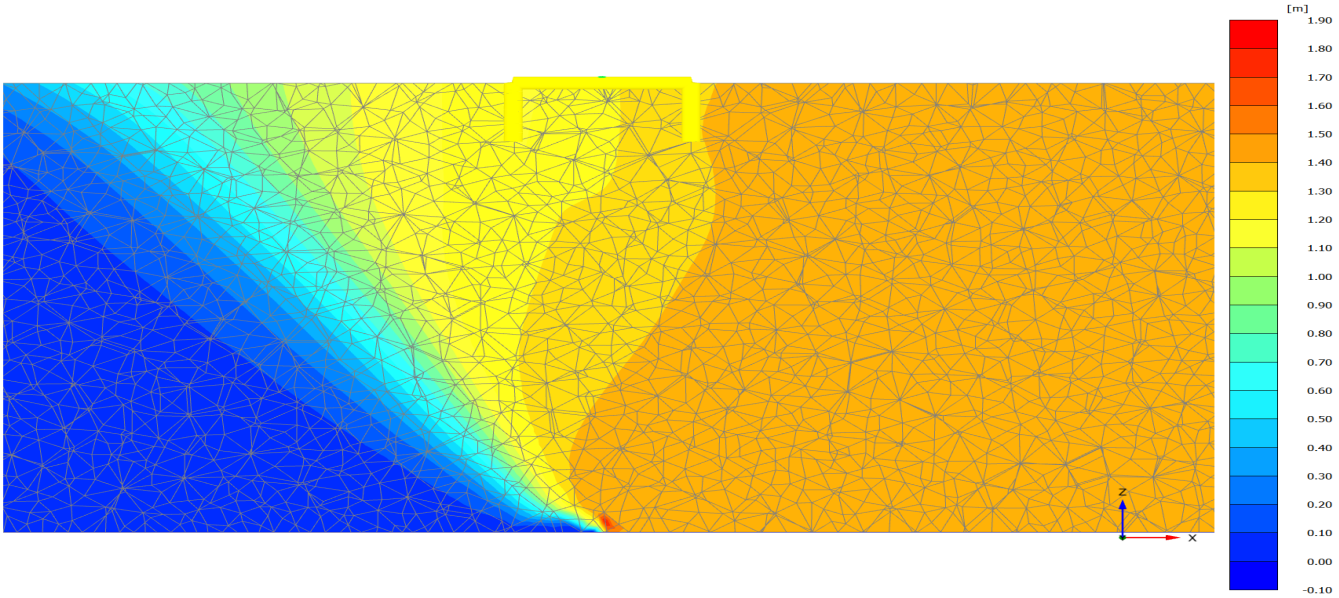

b) Bucket 3

Figure 4.38. Settlement profile, Case C and $L/D = 0.5$.

As it is mentioned before, the fault rupture which outcrops outside of the buckets is forcing them to displace along the negative x-axis. Thus, the maximum and minimum nodal horizontal displacements of each leg are presented in Table 4.18. By this way, it is again verified that the bucket is tilted counter-clockwise. Case C produces the highest displacements, compared Case A and B, while the dislocation is equivalent with Case C for $L/D = 1$.

The horizontal displacement and the rotation of the structure is enforcing the connection beams to rotate also for -2.14, 1.77 and 0.2 degrees for buckets 1, 2 and 3 respectively.

Bucket	u_{xmin}[cm]	u_{xmax}[cm]
1	-76	-88
2	-67	-90
3	-88	-100

Table 4.18. Tripod horizontal displacements for Case C and $L/D = 0.5$.

The deformation representation of the buckets can be seen in Figure 4.39. The mechanism is clear; all the buckets are rotating, while buckets 1 and 3 are also moved significantly upwards due to the reverse fault movement.

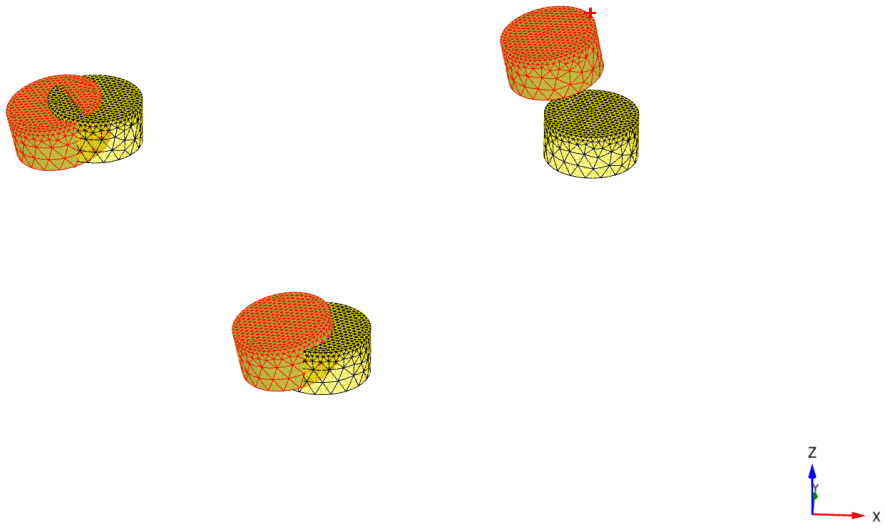

Figure 4.39. Deformed (red) versus stationary (yellow) tripod after fault rupture for Case C and $L/D = 0.5$.

Lastly, the forces acting on the structure are examined on Tables 4.19 and 4.20. Interestingly, the loads acting on the tripod with $L/D = 0.5$ are approximately half of them in $L/D = 1$, or on some cases even less.

Force	Units	Max	Min
N_1	MN/m	22.78	-20.03
N_2	MN/m	9.96	-8.58
Q_{12}	MN/m	11.74	-9.92
Q_{13}	MN/m	477.8	-558.8
Q_{23}	MN/m	261.8	-157.2
M_{11}	MNm/m	60.42	-70.97
M_{12}	MNm/m	23.88	-32.01
M_{22}	MNm/m	30.03	-31.09

Table 4.19. Maximum and minimum forces acting on the tripod for Case C and $L/D = 0.5$.

Force	Units	Max	Min
N	MN	-2.59	-13.05
Q_{12}	MN	6.47	-3.60
Q_{13}	MN	-7.15	-13.96
M_1	MNm	39.23	-25.9
M_2	MNm	35.49	-257.8
M_3	MNm	78.69	-141.3

Table 4.20. Maximum and minimum forces acting on the beams for Case C and $L/D = 0.5$.

The mechanism for reverse fault rupture-tripod suction bucket foundation for Case C and $L/D = 1$ can be summarized as:

1. The entire tripod is attached to the hanging wall.

2. The fault rupture path is alternated against the free field and emerges all round bucket 2. The concentration of plastic shear strains on the other two buckets is small.

3. There is significant displacement and rotation of the entire structure while it tilts counter-clockwise which also creates settlements.

4. The loads acting on the tripod due to the fault rupture for $L/D = 0.5$ are halved than those for $L/D = 1$.

5. The response overall is similar to $L/D = 1$; the only change that makes $L/D = 0.5$ beneficial is the forces acting on the structure.

4.5 Discussion of results for L/D=0.5

In this section, a summary of the results for all three cases with $L/D = 1$ ratio is presented and discussed. Case A is the most beneficial in all the aspects where all the buckets stay in the footwall. Thus, the contact area of the foundation is large, the loads acting due to the fault the lowest and no structural rotation is experienced. The rupture influences the tripod only by dislocating it approximately 15 centimeters along the negative x-axis. In addition, the plastic shear strains tend to avoid the the structure and the fault emerges in the vicinity of the skirt.

Besides Case A, the other two cases both causing the tripod to undergone significant rotations and loads. Regarding the horizontal dislocation, Case B is beneficial while Case C is preferred in terms

of settlements and structural rotations. The loads acting in both Case B and C are identical and no clear distinction can be made.

Overall, considering the fact that the tripod behaves as a rigid body, meaning that the horizontal displacement might not be damaging it can be claimed that Case B, where the fault is about to outcrop below bucket 3 is the worst case scenario for $L/D = 0.5$.

Conclusions and future work 5

In this thesis, a Numerical Analysis Dip-Slip of Fault-Suction Bucket Interaction was performed. The model was constructed in commercial Finite Element Analysis program Plaxis 3D. The model consisted of 25 meters dense sand with a width equal to 100 meters to avoid the undesired boundary effects. The Hardening Soil model with small strain stiffness (HSsmall) soil parameters were calibrated against centrifuge tests by (K. Nielsen [2020]) and were verified in this thesis against results published by (Anastasopoulos et al. [2007]) for both normal and reverse fault rupture. The verification was conducted in terms of vertical displacement versus distance plots and plastic shear strain contours.

After the verification of the numerical model and soil parameters, a parametric study was conducted to see the influence of reverse fault rupture on a tripod suction bucket foundation. The foundation was modelled by very rigid plate materials, and beam materials were connecting the tripod legs. A vertical load accounting for $0.5V_{peak}$ was applied at a height 5 meters above the seabed. Since the exact position of fault outcroping is not known in advance, the position of the structure was varied in a way that the fault rupture would outcrop by the absence of the structure below each bucket, subsequently. In addition, the length of the skirt was varied examining two cases, one with $L/D = 1$ and one with $L/D = 0.5$ to see the influence of the skirt length on the response. The comparison was conducted in terms of plastic shear strain concentration, settlements, tripod displacements and forces acting on it due to the fault.

The first finding of this study is that HSsmall along with the proposed numerical model was able to capture the response under dip-slip fault rupture. The comparison with the previously published investigations was successful, with the almost perfect accuracy for reverse fault rupture. The response on normal fault rupture is considered acceptable but further improvements may be done in future studies.

For $L/D = 1$, it was found that the if the tripod is placed so the free field rupture would outcrop beneath bucket 1 -Case A-, the tripod acts as a kinematic constraint, causing complete diversion of the fault rupture path and forced it to develop outside the foundation margins.. In this way, the entire structure is displaced 15 centimeters along the negative x-axis, while no important rotations are evident. In the scenario of the fault outcroping below bucket 3 -Case B-, there is shear strain accumulation on the skirt of the buckets, while the path is bifurcated to outcrop on the right side of bucket's 3 skirt. The horizontal displacement of the tripod is increased, reaching almost 70 centimeters and significant structural rotations and loads are imposed. These rotations may risk the structural integrity and might not comply with Serviceability Limit State requirements. If the tripod is placed so that the fault rupture would emerge under bucket 2 -Case C-, there is significant plastic shear accumulation around and below the bucket as the fault rupture path outcrops on the vicinity of the skirt. The horizontal displacement reaches 1 meter but the structural rotations are still significant, but slightly reduced. The loads acting on the tripod and the connection beams are equivalent with Case B.

Based on the findings, it can be claimed that the preferred fault rupture outcrop position is as in Case A, while the worst case scenario is that if the fault emerges between the middle bucket, namely bucket 3.

For $L/D = 0.5$, the observed results indicated that the response is identical. Specifically, the shorter skirt tripod leads to deviation of the fault rupture path, while structural rotations and horizontal displacements were similar. Although, the tripod with $L/D = 0.5$ is beneficial in terms of the loads acting on it, which are halved than those acting on $L/D = 1$.

Overall, since the tectonic movements cannot be known in advance the designer of tripods in the vicinity of active faults should investigate all the possible fault scenarios accounting for both normal and reverse fault, model different bedrock offsets and design the tripod for the worst case scenario. In this research thesis, it was seen that because of the high level of soil confinement below the buckets, the fault rupture path is avoiding to outcrop, causing the fault to divert and emerge outside of the foundation margins. This is true for both $L/D = 0.5$ and $L/D = 1$.

Future work in the area may include some of the following:

- Further calibration of the numerical model and/or the soil parameters to capture the normal fault response more precisely.
- Model higher bedrock offsets for both normal and reverse fault rupture to observe how does this affects the results.
- Model looser sand or clay to see the influence of soil density on the results.
- Model the structure in a more realistic manner for further investigation regarding the forces acting on the structure, and if those forces risk the structural integrity. A more appropriate FEA program may be used for this purpose.
- Vary the surcharge load and see how it reduces the upward movement of the bucket, the horizontal displacement and the rotations imposed.
- Vary the spacing of the buckets to investigate the how the group effect influences the results.
- Model further L/D ratios and find the critical skirt length that forces the fault to outcrop outside of the bucket.
- Investigate the effect of strike-slip faults on a tripod suction bucket foundation.
- Centrifuge tests can be performed with a small scale tripod suction bucket foundation to verify experimentally the numerical observations.

Bibliography

Anastasopoulos, I., Callerio, A., Bransby, M., Davies, M., Nahas, A. E., Faccioli, E., Gazetas, G., Masella, A., Paolucci, R., Pecker, A. and Rossignol, E. [2008], 'Numerical analyses of fault-foundation interaction', *Bulletin of Earthquake Engineering* **6**, 645–675.

Anastasopoulos, I. and Gazetas, G. [2007*a*], 'Foundation-structure systems over a rupturing normal fault: Part I. Observations after the Kocaeli 1999 earthquake', *Bulletin of Earthquake Engineering* **5**, 253–275.

Anastasopoulos, I. and Gazetas, G. [2007*b*], 'Foundation-structure systems over a rupturing normal fault: Part II. Observations after the Kocaeli 1999 earthquake', *Bulletin of Earthquake Engineering* **5**, 277–301.

Anastasopoulos, I., Gazetas, G., Bransby, M., Davies, M. and Nahas, A. E. [2007], 'Fault Rupture Propagation through Sand: Finite-Element Analysis and Validation through Centrifuge Experiments', *Journal of Geotechnical and Geoenvironmental Engineering* **133**, 943–958.

Anastasopoulos, I., Gazetas, G., Bransby, M., Davies, M. and Nahas, A. E. [2009], 'Normal Fault Rupture Interaction with Strip Foundations', *Journal of Geotechnical and Geoenvironmental Engineering* **135**, 359–370.

Anastasopoulos, I., Kourkoulis, R., Gazetas, G. and Tsatsis, A. [2013], 'Interaction of piled foundation with a rupturing normal fault', *Geotechnique* **63**, 1042–1059.

Bhattacharya, S. [2019], *Design of foundations for offshore wind turbines*, John Wiley Sons Ltd.

Bransby, M., Davies, M. and Nahas, A. E. [2008], 'Centrifuge modelling of normal fault-foundation interaction', *Bulletin of Earthquake Engineering* **6**, 585–605.

Bransby, M., Davies, M., Nahas, A. E. and Nagaoka, S. [2008], 'Centrifuge modelling of reverse fault-foundation interaction', *Bulletin of Earthquake Engineering* **6**, 607–628.

Gazetas, G., Pexker, A., Faccioli, E. and Paolucci, R. [2008], 'Preliminary design recommendations for dip-slip fault-foundation interaction', *Bulletin of Earthquake Engineering* **6**, 677–687.

Houlsby, G. T., Ibsen, L. B. and Byrne, B. W. [2005], 'Suction caissons for wind turbines', *Frontiers in Offshore Geotechnics* **3**.

IRENA [2020], *Renewable capacity statistics 2020 International Renewable Energy Agency (IRENA)*, Abu Dhabi.

K. Glitrup and L.R. Christiansen [2019], *Calibration of Advanced Constitutive Models to Investigate Cyclic Behavior of a Tripod Suction Bucket Foundation*, Aalborg University.

K. Nielsen [2020], *Group Effect on Bearing Capacities of Multi Bucket Foundations in Sand*, Aalborg University.

Kramer, S. [1996], *Geotechnical Earthquake Engineering*, Prentice-Hall, Inc.

Loli, M., Anastasopoulos, I., Bransby, M., Ahmed, W. and Gazetas, G. [2011], 'Numerical analyses of fault-foundation interaction', *Journal of Geotechnical and Geoenvironmental Engineering* **137**, 914–925.

Marza, V. I. [2014], 'On the death toll of the 1999 Izmit (Turkey) major earthquake'.

Plaxis [2020*a*], *Plaxis 3D-Reference Manual CONNECT Edition V20.04*, Bentley Systems.

Plaxis [2020*b*], *Plaxis Material Models Manual CONNECT Edition V20.04*, Bentley Systems.

Rasouli, H. and Fatahi, B. [2018], 'A novel cushioned piled raft foundation to protect buildings subjected to normal fault rupture', *Computers and Geotechnics* **106**, 228–248.

Rokonuzzaman, M., Nahas, A. E. and Sakai, T. [2014], 'Experimental validation of a numerical model for the interaction of dip-slip normal fault ruptures, sand deposits, and raft foundations', *International Journal of Geotechnical Engineering* .

Rokonuzzaman, M., Sakai, T., Nahas, A. E., Tanaka, T. and Hossain, M. Z. [2009], 'Experimental validation of a numerical model: Reverse fault rupture propagation through sand', *Doboku Gakkai Ronbushu* **65**, 151–161.

Spyridonidou, S., Vafiona, D. and Loukogeorgaki, E. [2020], 'Strategic Planning of Offshore Wind Farms in Greece', *Sustainability* **12**, 1–20.

Appendices

Hardening Soil Model with Small Strain Stiffness

A

In this chapter, the theoretical framework of Hardening Soil Model with Small Strain Stiffness is presented based on (Plaxis [2020b]). Also, the calibrated values used as input in Plaxis 3D are shortly explained.

Hardening Soil Model with Small Strain Stiffness (herein HSsmall for brevity) is an advanced hardening plasticity constitutive model based on Hardening Soil model. The yield surface can expand due to plastic straining. Both shear and compression hardening are contained in this model, while when soil is subjected to primary deviatoric loading shows a decrease in stiffness accompanied with irreversible plastic strains.

A.1 Stiffness parameters

A basic idea for the formulation of HSsmall is the hyperbolic relationship between the vertical strain ϵ_1 and the deviatoric stress q in primary triaxial loading. Standard triaxial tests tend to yield curves that can be described by:

$$-\epsilon_1 = \frac{1}{E_i}\frac{q}{1-q-q_a} \qquad for \quad 1 < q_r \tag{A.1}$$

Where:

ϵ_1	axial strain [-]
E_i	Initial stiffness [kPa]
q	Deviatoric stress [kPa]
q_a	Asymptotic value of the shear strength [kPa]
q_f	Ultimate value of deviatoric stress[kPa]

Initial stiffness E_i, is related to the confining stress dependent stiffness modulus for primary loading E_{50} at 50% maximum deviatoric stress applied by:

$$E_i = \frac{2E_{50}}{2-R_f} \tag{A.2}$$

Where R_f is the failure ration q_a/q_f. This relationship is plotted in Figure A.1.

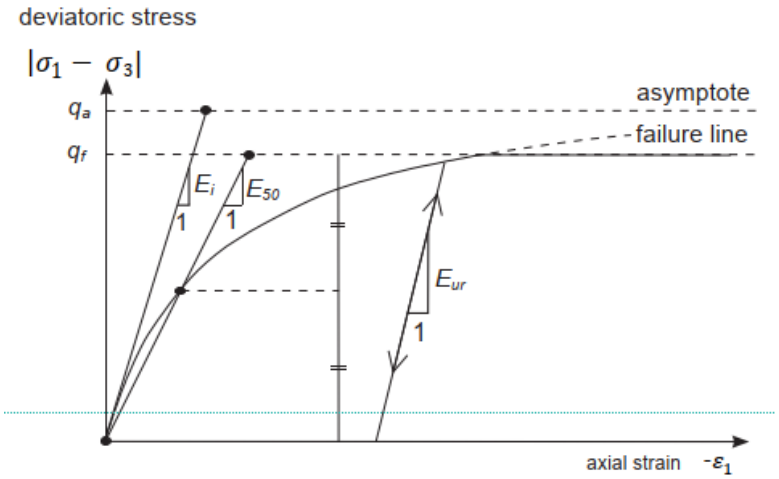

Figure A.1. Hyperbolic stress-strain relation in primary loading for a standard drained triaxial test, (Plaxis [2020*b*]).

The secand modulus E_{50} is given by drained triaxial tests by calculating the secant stiffness at 50 % maximum deviatoric stress and is connected with E_{50}^{ref}, the reference stiffness modulus as:

$$E_{50} = E_{50}^{ref} \left(\frac{ccos(\phi) - \sigma_3' sin(\phi)}{ccos(\phi) - p^{ref} sin(\phi)} \right)^m \tag{A.3}$$

Plaxis default reference confining pressure is 100 stress units, while c is the cohesion. Power (m) varies from 0.5 for Norwegian sand and silts to 1 for soft clays. The ultimate deviatoric stress q_f is given by:

$$q_f = (ccot(\phi) - \sigma_3') \frac{2sin(\phi)}{1 - sin(\phi)} \tag{A.4}$$

For unloading/reloading stress paths, another stress-dependent stiffness modulus is used:

$$E_{ur} = E_{ur}^{ref} \left(\frac{ccos(\phi) - \sigma_3' sin(\phi)}{ccos(\phi) - p^{ref} sin(\phi)} \right)^m \tag{A.5}$$

Where E_{ur}^{ref} is the reference Young's modulus and reloading, corresponding to the reference pressure p_{ref}. In many cases like this, it is appropriate to set $E_{ur}^{ref} = 3E_{50}^{ref}$.

Finally, the oedometer stiffness modulus even though is calculated by oedometer test results, the absence of those lead to:

$$E_{oed}^{ref} = \frac{E_{50}^{ref}}{1.25} \tag{A.6}$$

As it is already mentioned, soil stiffness decays nonlinearly with increasing strain amplitude and this is the main difference between HS model and HSsmall model, with the latter one taking into account this behavior, as well as hysteresis under cyclic loading. This reduce of soil stiffness can be attributed to the loss of intermolecular and surface forces within the soil skeleton.

Hardin-Drnevich relationship which is based on laboratory tests describes the relation between soil stiffness and shear strain by the following hyperbolic law:

$$\frac{G_S}{G_0} = \frac{1}{1 + a|\frac{\gamma}{\gamma_{0.7}}|} \tag{A.7}$$

Compared to standard HS model, HSsmall requires two additional parameters as input, namely reference shear modulus at very small strains ($\epsilon < 10^{-6}$), G_0^{ref} and threshold shear strain at which $G_s = 0.722G_0$.
In order to define G_0, (K. Glitrup and L.R. Christiansen [2019]) took into account the fines content by the following relationship:

$$G_0(FC) = G_0(FC = 0)f_r(FC) \tag{A.8}$$

Where:

$G_0(FC = 0)$	Small strain shear modulus for clean sand
f_r	Reduction factor depending on fines content

With:

$$f_r(FC) = \begin{cases} 1 - 0.043FC & \text{for FC} \leq 10\ \% \\ 0.57 & \text{for FC} \geq 10\ \% \end{cases} \tag{A.9}$$

The threshold shear strain $\gamma_{0.7}$ is calculated by:

$$\gamma_{0.7} = \frac{1}{9G_0}(2c'(1 + cos(2\phi')) - \sigma_1'(1 + K_0)sin(2\phi')) \tag{A.10}$$

Where:

K_0	Lateral earth pressure coefficient at rest
σ_1'	Effective vertical stress

A.2 Strength Parameters

Three of the parameters used in HSsmall coincide with those of the non hardening linear elastic perfectly plastic Mohr-Coulomb model, meaning the cohesion c, friction angle ϕ and dilation angle ψ.

These parameters were calculated by (K. Glitrup and L.R. Christiansen [2019]) based on triaxial test with different relative densities and confining pressures. Given the strains ϵ_α and ϵ_ν, the dilation angle can be found by:

$$\psi = arcsin\left(\frac{\frac{d\epsilon_\nu}{d\epsilon_\alpha}}{\frac{d\epsilon_\nu}{d\epsilon_\alpha} - 2}\right) \tag{A.11}$$

Although, the value of the dilatancy angle was found to be unrealistically high and the suggested expression from (Plaxis [2020*b*]) as $\psi' = \phi' - 30$ was employed. The cohesion was taken as 0.2 kPa in order to avoid numerical instabilities in Plaxis 3D.
The lateral earth pressure coefficient at rest is calculated by:

$$K_0 = 1 - sin(\phi') \tag{A.12}$$

The effective Poisson's ratio is determined as:

$$\nu = \frac{1 - sin(\phi')}{2 - sin(\phi')} \tag{A.13}$$

A.3 Dilatancy cut-off

Dilative materials like sand arrive in a critical density state where dilatancy has come to an end, after extensive shearing, see Figure A.2. This phenomenon is handled with HSsmall with the dilatancy cut-off choice. If the

dilatancy cut-off is set as true, the initial and maximum void ratio, e_{init} (in-situ void ratio) and e_{max} (critical state void ratio) respectively need to be defined. As soon as the maximum void ratio is reached due to volume change under the loading, the mobilised dilatancy angle is set to zero.

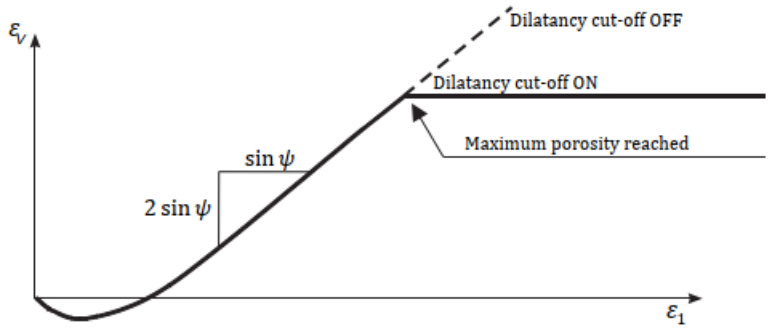

Figure A.2. Strain curve for standard drained triaxial test with cut-off, (Plaxis [2020*b*]).

Free field results

B

In this chapter, the remaining results from the free field calculations are presented. These results include the deformed soil volumes under normal and reverse fault, along with the deformed mesh with shear strain localisation for the bedrock offsets for which no similar results are available to compare.

One prerequisite to conduct the parametric study is that the fault rupture emerges at the surface and interacts with the foundation which may alternate the fault path and the displacement and rotation mechanisms. Thus, higher offsets are modelled. The additional offsets are presented in Table B.1.

Fault type	**Bedrock offset h (m)**	
Normal	1.5	2.0
Reverse	1.5	2.0

Table B.1. Type of fault and bedrock offsets modelled for the parametric study.

The reverse fault with 1.5 meter bedrock offset is used in the main report for the parametric analysis, while the rest are presented herein. These offsets are not used due to time limitations but can form the basis of a further study. In this way, a future proposed model can be verified or calibrated.

Reverse fault

Figures B.1 and B.2 illustrate the deformed soil and localised shear strain band, respectively, under 0.70 meters reverse fault rupture. Note that the deformed soil volume is scaled up 5 times for clarity In this scenario it is evident that even though the the soil deforms, the plastic shear strain concentration is not propagating up to the soil surface, meaning that the rupture does not outcrop.

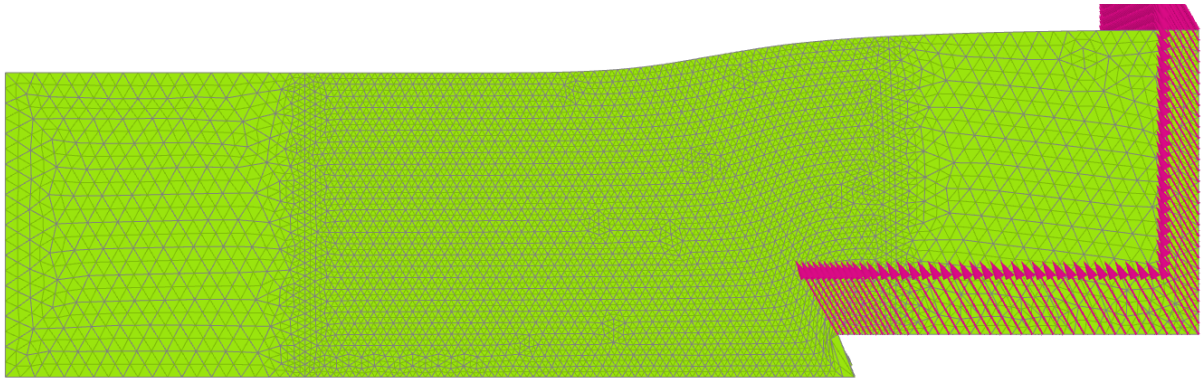

Figure B.1. Deformed soil volume and mesh after 0.70 meters reverse fault rupture.

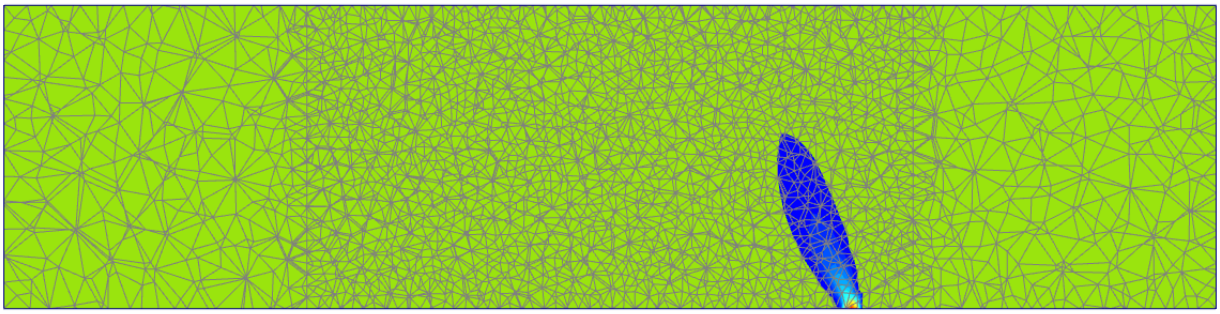

Figure B.2. FEA plastic shear strain concentration for 0.70 meters reverse fault.

Figures B.3 and B.4 illustrate the deformed soil and localised shear strain band, respectively, under 0.50 meters reverse fault rupture. In this scenario, the soil deformation reduces further and the shear strain band is as expected also reduced, causing the fault not to outcrop on the surface.

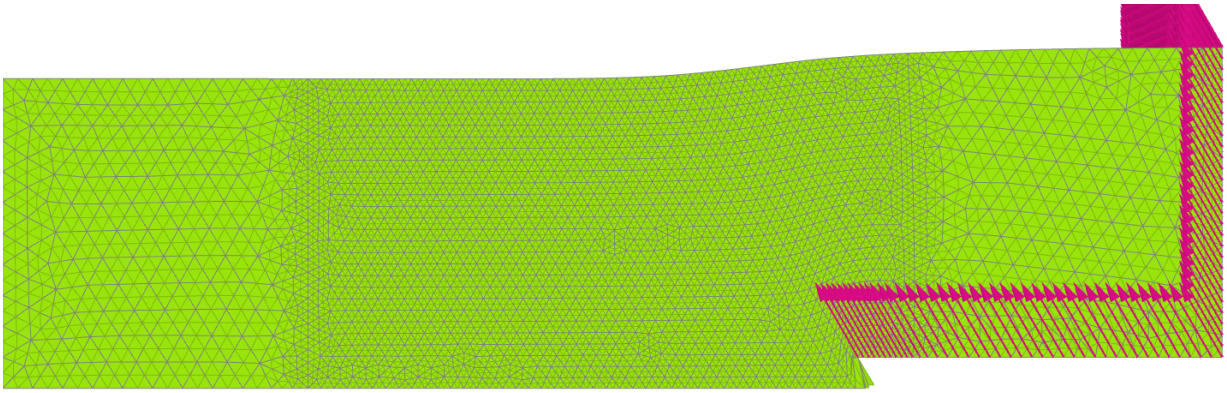

Figure B.3. Deformed soil volume and mesh after 0.50 meters reverse fault rupture.

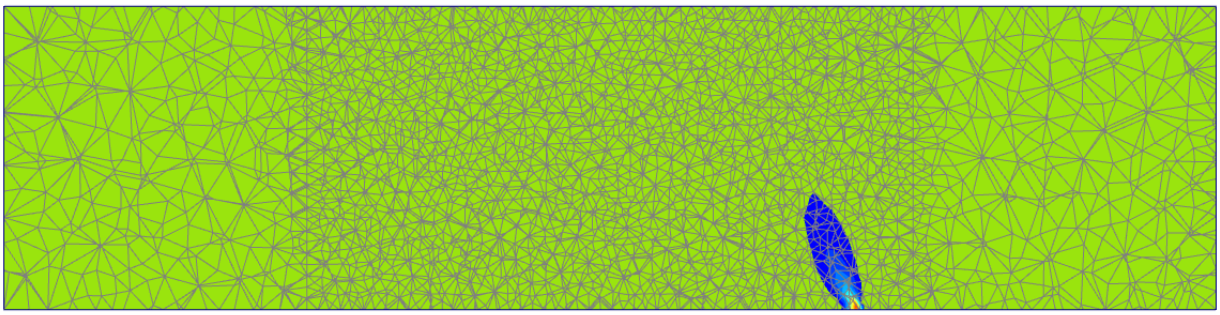

Figure B.4. FEA Plastic shear strain concentration for 0.50 meters reverse fault.

Finally, Figures B.5 and B.6 depict the deformed soil and localised shear strain band, respectively, under 0.19 meters reverse fault rupture. It can be now claimed that a reverse fault rupture of that intensity will probably not affect significantly any type of foundation. The imposed displacements are minor, while the shear strain band is limited to the very bottom of the soil layer, letting practically any type of structure founded above remain untouched.

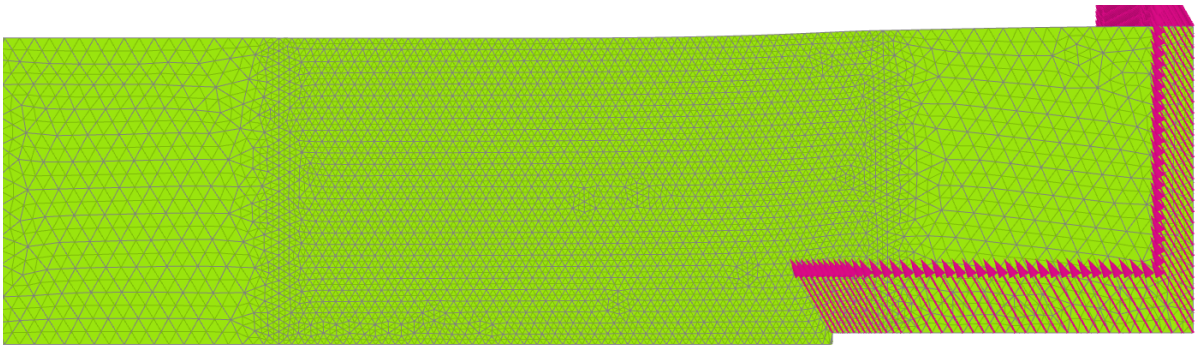

Figure B.5. Deformed soil volume and mesh after 0.19 meters reverse fault rupture.

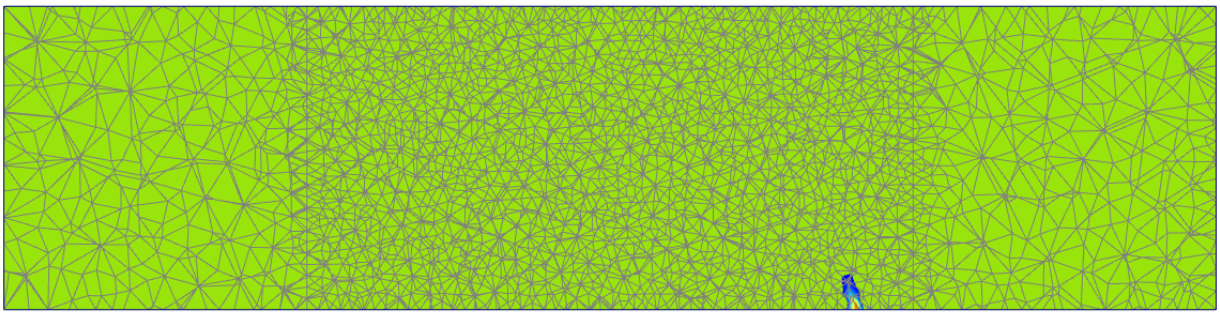

Figure B.6. FEA plastic shear strain concentration for 0.19 meters reverse fault.

The deformed soil volume, the plastic shear strains and the $\Delta_y - d$ plot for 2 meters reverse fault are presented in the following figures. Note that due to the high strain concentration, only strains higher than 0.07 are depicted.

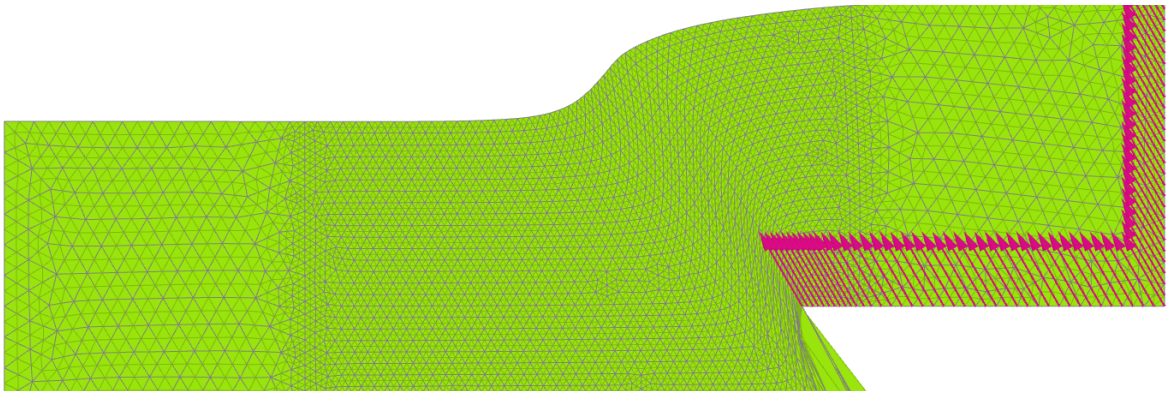

Figure B.7. Deformed soil volume and mesh after 2.00 meters reverse fault rupture.

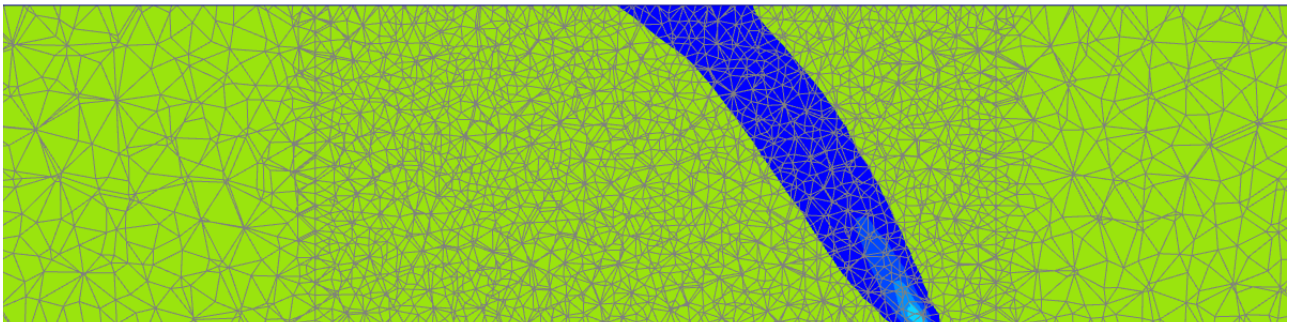

Figure B.8. FEA plastic shear strain concentration for 2.00 meters reverse fault.

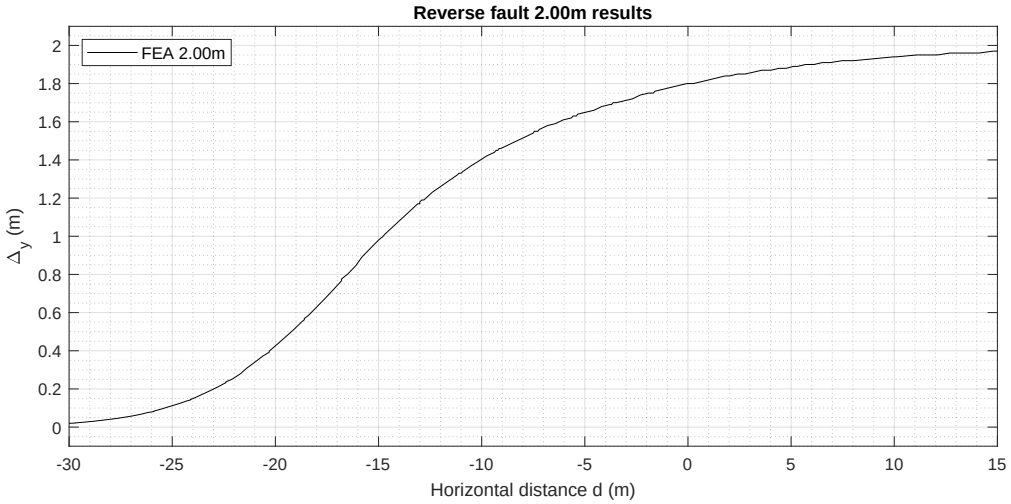

Figure B.9. $\Delta_y - d$ comparison for reverse fault with 2.00 meters bedrock offset.

Normal fault

Figures B.10 and B.11 illustrate the deformed soil and localised shear strain band, respectively, under 0.8225 normal fault rupture. One interesting difference is that the deformation is more significant with the reverse fault rupture with similar bedrock offset, see Figure B.1 . Also, the fault path emerges on the surface while the normal fault with 0.70 meters dislocation is not, as it is depicted in Figure B.2 . Based on these observations, one can claim that the damage to a potential structure founded above a normal fault might experience heavier damage.

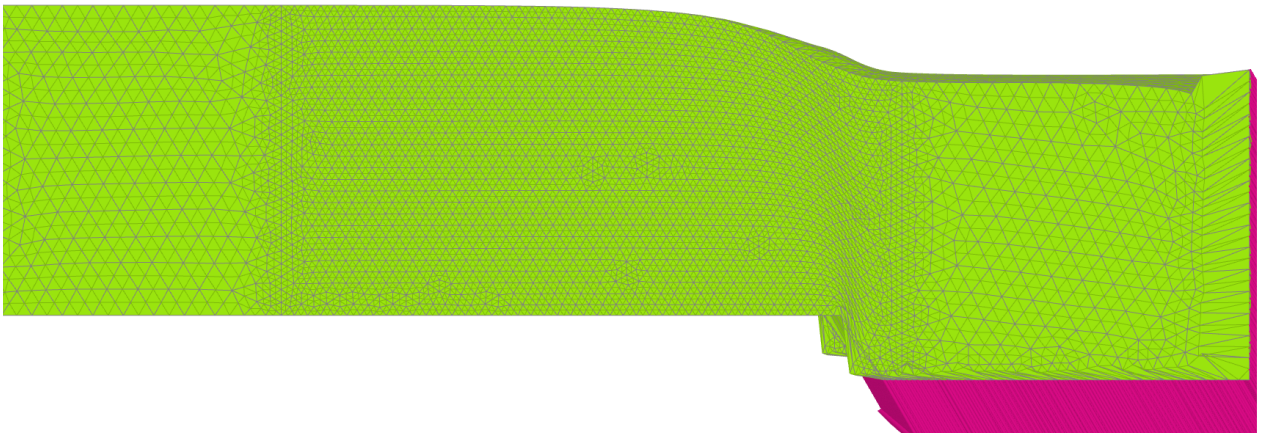

Figure B.10. Deformed soil volume and mesh after 0.825 meters reverse fault rupture.

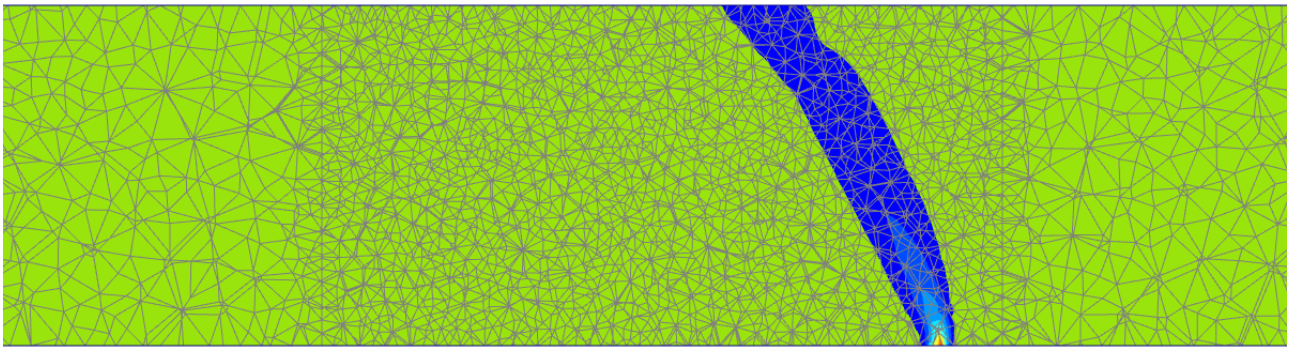

Figure B.11. FEA plastic shear strain concentration for 0.825 meters reverse fault.

Figures B.12 and B.13 illustrate the deformed soil and localised shear strain band, respectively, under 0.50 normal fault rupture. In this case the soil distortion is as expected reduced, although it can be noticed that high levels of plastic shear concentration are present up to a depth of approximately 10 meters.

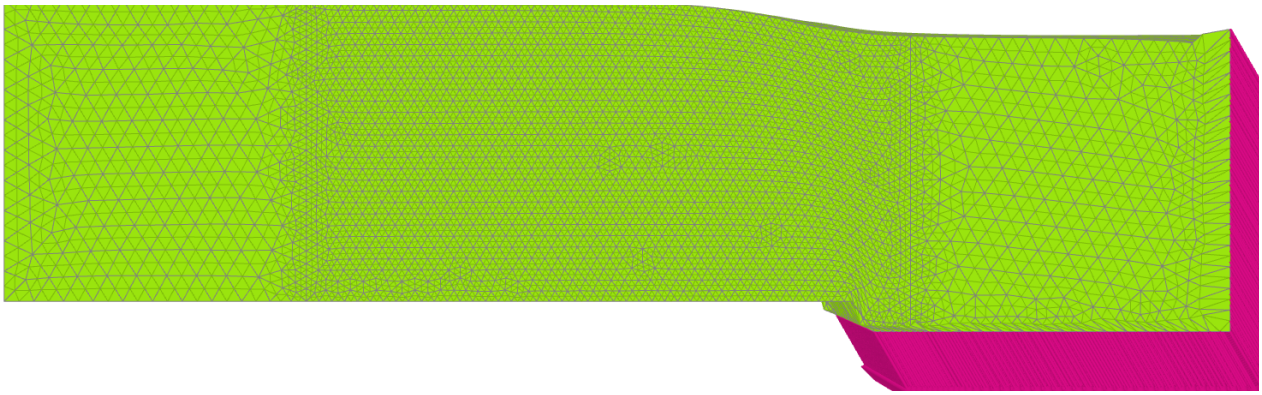

Figure B.12. Deformed soil volume and mesh after 0.50 meters reverse fault rupture.

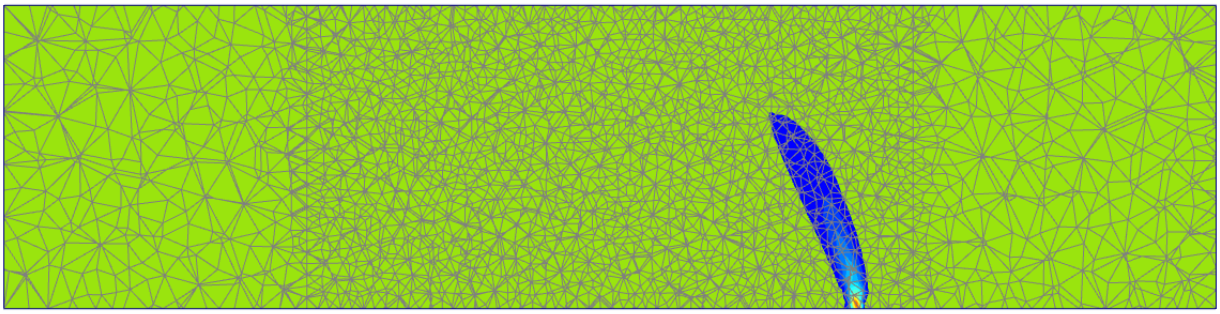

Figure B.13. FEA Plastic shear strain concentration for 0.50 meters reverse fault.

Figures B.14 and B.15 illustrate the deformed soil and localised shear strain band, respectively, under 0.225 normal fault rupture. With this amount of bedrock offset the deformations remain small, while the shear band is very narrow and is not propagating above 18 meters of soil depth, leaving the potential structures -especially those founded in shallow foundations- unaffected.

Figure B.14. Deformed soil volume and mesh after 0.225 meters reverse fault rupture.

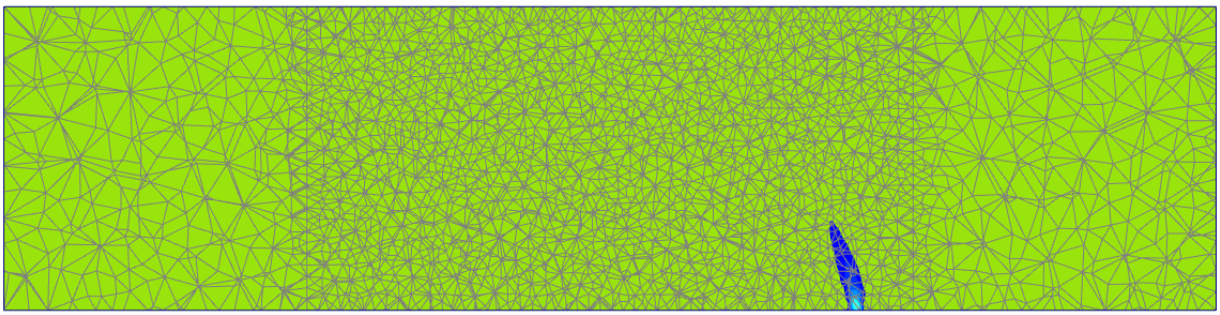

Figure B.15. FEA plastic shear strain concentration for 0.225 meters reverse fault.

The deformed soil volume, the plastic shear strains and the $\Delta_y - d$ plot for 1.50 meters normal fault calculated for future studies are presented in the following figures. Note that due to the high strain concentration, only strains higher than 0.07 are depicted.

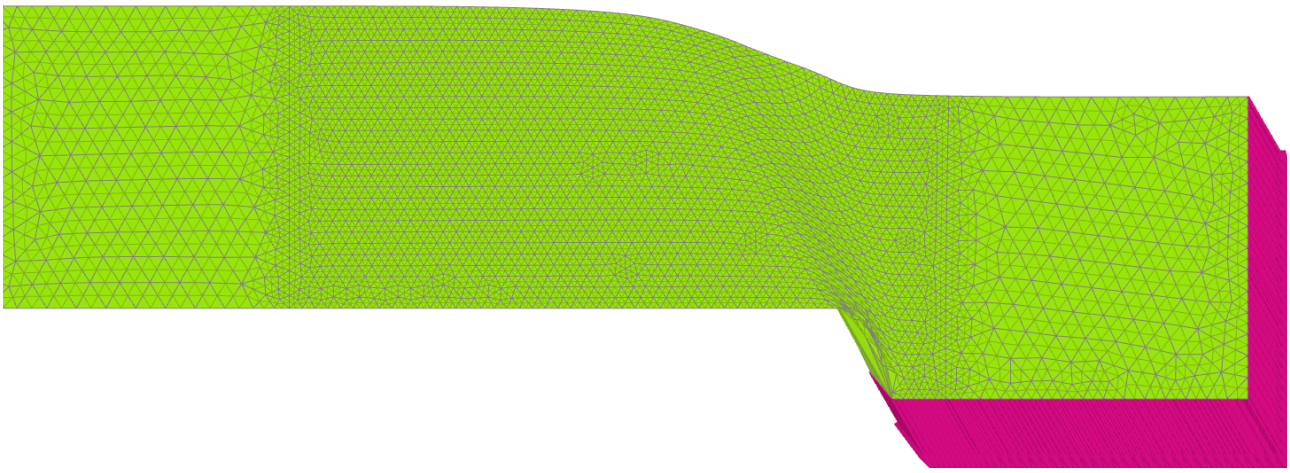

Figure B.16. Deformed soil volume and mesh after 1.50 meters normal fault rupture.

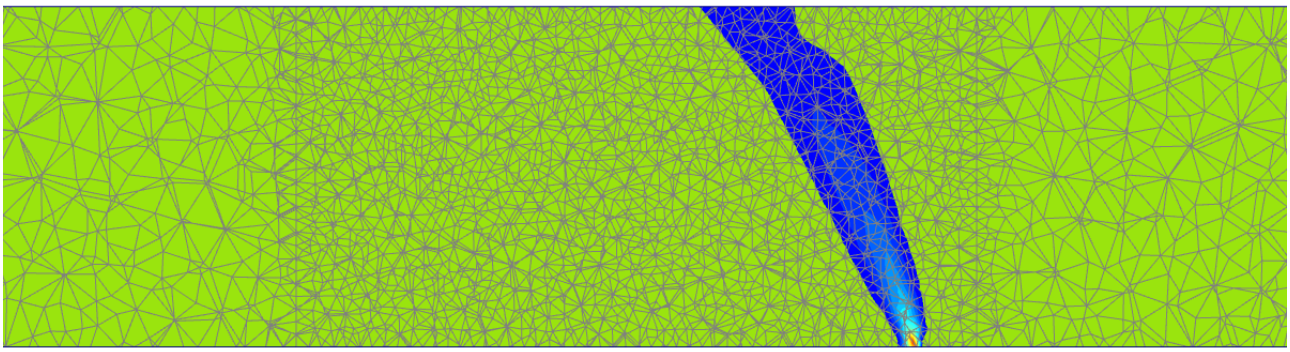

Figure B.17. FEA plastic shear strain concentration for 1.50 meters normal fault.

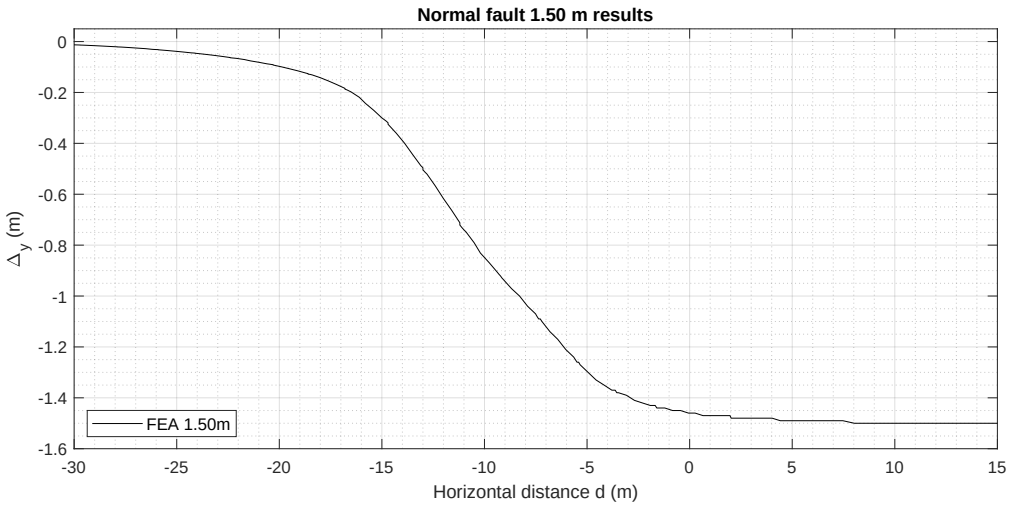

Figure B.18. $\Delta_y - d$ comparison for normal fault with 1.50 meters bedrock offset.

Lastly, the deformed soil volume, the plastic shear strains and the $\Delta_y - d$ plot for 2.00 meters normal fault are presented in the following figures. Note that again only strains higher than 0.07 are depicted.

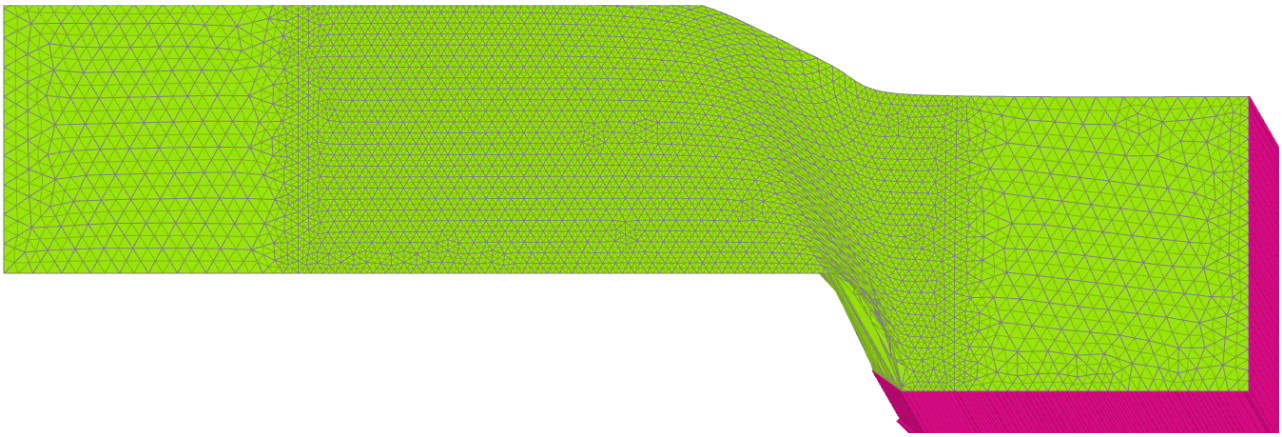

Figure B.19. Deformed soil volume and mesh after 2.00 meters normal fault rupture.

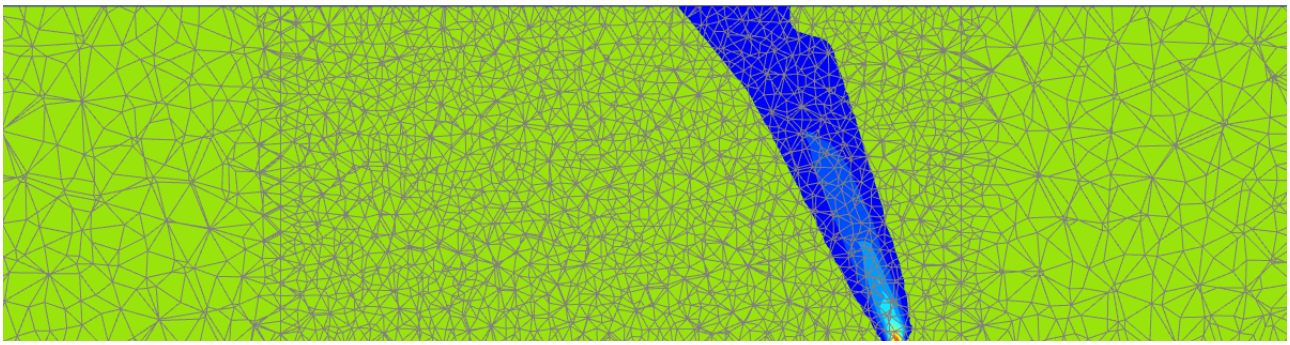

Figure B.20. FEA plastic shear strain concentration for 2.00 meters normal fault.

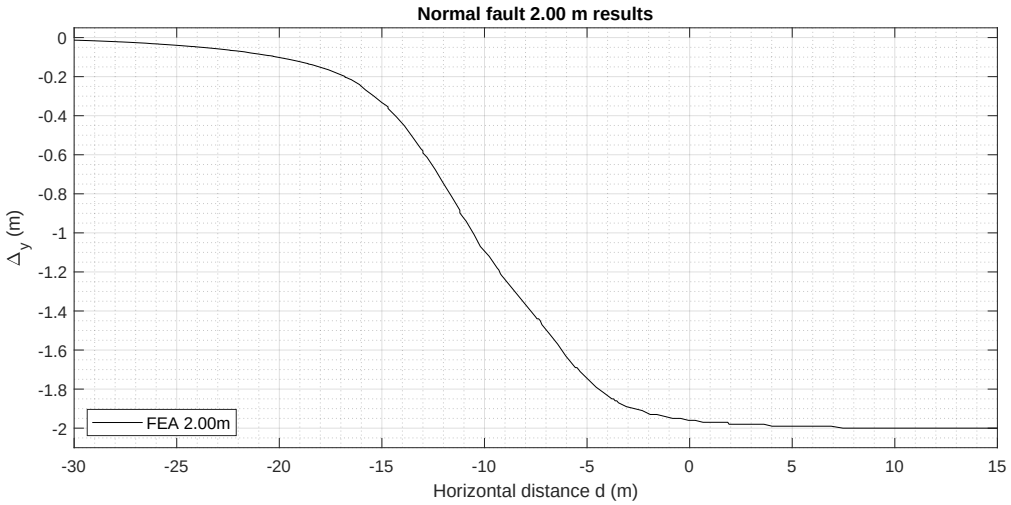

Figure B.21. $\Delta_y - d$ comparison for normal fault with 2.00 meters bedrock offset.